WASHINGTON UNIVERSITY IN ST. LOUIS
Department of Physics

Dissertation Examination Committee:
Lee Sobotka, Chair
Robert Charity, Co-Chair
Willem Dickhoff
Manel Errando
Saori Pastore

Proton-Decay Branches and Structures in ^{7}Li and in Neutron-Poor Nuclides Around Calcium

by
Nicolas Danato Dronchi

A dissertation presented to
Washington University in St. Louis
in partial fulfillment of the
requirements for the degree
of Doctor of Philosophy

December, 2024 St. Louis, Missouri

Table of Contents

List of Figures

List of Tables

Acknowledgements

It is only through a huge number of people that my education and the research in this dissertation was possible. “If I have seen further it is by standing on the shoulders of giants” -Isaac Newton, 1675.

I’ll start by saying I greatly appreciate my advisors Lee Sobotka and Robert Charity. It is through their thoughts and ideas that I had projects to work on and it is also through them that I was able to bring this dissertation to completion. The time and mentoring they have given to me has been invaluable and has made me the scientist I am today.

I would like to thank the people at Washington University who have supported me. I appreciate my committee members who have read this dissertation while also advising me through my education. Thank you to the radiochemistry group. I will miss the time we spent together in our “historic” building and our lunch-table discussions. Finally, it has been an honor working alongside my graduate student friends and colleagues in the physics department including my classmates, mentors, and outreach/committee members.

Just like at the bottom of each paper, I thank the DOE for the fact that this work was funded and that I was paid money to do it. Thanks a ton to all my collaborators: at Michigan State, who made my experiment actually work in the early days of Covid-19; at Texas A&M, especially to the beam scientists who worked tirelessly at my experiment; to the CENTAUR collaboration, who always allowed me to join in on the fun. Finally, I appreciate the many opportunities available for conferences, internships, and schools within the nuclear physics community.

My last and biggest thank you goes out to my family who supported me but also grew with me. I love you Mom and Dad. You were my original supporters all the way from day one, and have always been the rock I need to succeed. I am most grateful to the late grandpa

Joe Dronchi, who freed me of the financial costs of higher education, allowing me to study what excited me. Finally, to the one who actually had to deal with me on a day-to-day, I thank my wife Carly. It isn't possible to express how much you have supported me but I think legally, half this dissertation is yours. Curie (the rat dog), I know you can't read, but I think you belong in the list of thank yous as well.

While it definitely wasn't easy, I think I will always look back fondly at my time in graduate school.

Nicolas Danato Dronchi

Washington University in St. Louis

December, 2024

ABSTRACT OF THE DISSERTATION

Proton-Decay Branches and Structures in ^{7}Li and in Neutron-Poor Nuclides Around Calcium

by
Nicolas Danato Dronchi
Doctor of Philosophy in Physics
Washington University in St.Louis, 2024
Advised by Lee Sobotka and Robert Charity

The collection of proton decays observed via invariant-mass spectroscopy in this work have been applied to an array of topics in nuclear physics including the continuum effects on near-threshold resonances, the branching ratio for a quasi-bound system, and evidence for the evolution of shell structure. In the first experiment, the ^{6}He(d,n)^{7}Li* reaction was employed in an attempt to populate a resonance predicted by an *ab initio* calculation. No evidence of this resonance was found leading to a discussion on how the model needs to be improved in order to treat nuclear states above multiple thresholds. In a separate experiment, the p/γ branching ratio for the first 2^{+} state of ^{36}Ca was studied and measured to be B_p = 0.087(8). This branching ratio enabled the measurement of a $B(E2,\, 0_1^+ \rightarrow 2_1^+)$ strength of ^{36}Ca [$B(E2\uparrow) = 131(20)\ e^2\text{fm}^4$]. The $B(E2)$ and branching-ratio values can be reproduced in the shell-model with the ZMB2 interaction, an interaction that predicts the $Z = 20$ *sd*-shell closure is incomplete with large proton pf-shell occupancies in the ground state. This experiment also resulted in a set of reactions populating proton-rich nuclei including ^{35}Ca and the first observations of ^{37,38}Sc and ^{34}K. Proton decays for these nuclei were reconstructed, yielding three new ground-state masses and information on their low-lying structures. The newly-measured mass excesses are: ΔM(^{37}Sc) = 3500(410) keV, ΔM(^{38}Sc) = -4656(14) keV, and ΔM(^{34}K) = -1487(17) keV. These masses enable us to look at trends in separation energies, which help elucidate how nuclear structure evolves, showing a fading of the Z=20 shell gap for $N \leq$18 and indications of a N=16 subshell gap.

Chapter 1

Introduction

In this dissertation, the exotic decay mode of proton emission has been experimentally studied. The forthcoming chapters include three different examples of proton emission: (1) excited states above multiple decay thresholds, (2) an excited state that has competing proton-decay and gamma-decay modes, and (3) ground states of nuclei beyond the proton drip line. The measurements contained in this work provide important tests of models that calculate the interactions between protons and neutrons in nuclei, where the loosely bound systems couple strongly to the continuum. This work has also added evidence on the evolution of shell structure for nuclei far from stability by observing three new ground-state masses for isotopes beyond the proton drip-line. In the big picture, the study of proton emission helps to answer the question on how protons and neutrons interact through the strong force. Answering this, helps us extrapolate to systems inaccessible in the laboratory such as stellar systems, and in so doing helps explain where the elements and isotopes we are made of are formed.

1.1 Stability and nuclear decay

Atoms have a negatively-charged cloud of electrons which surround a dense, positively-charged core called the nucleus. The nucleus is comprised of two different nucleon types, positively-charged protons and neutrons with no charge. The proton number (Z) determines what element the atom is and the neutron number (N) determines the specific isotope for a given element (with mass number A = N + Z). Figure 1.1 shows the chart of nuclides, plotting proton number versus neutron number to visualize the landscape of possible nuclei, where the black boxes indicate stable nuclei and the colors indicate unstable nuclei with different decay modes. Here, the word "stable" indicates the nucleus has a lifetime commensurate with the age of the universe while unstable nuclei are defined by their half-life ($t_{1/2}$), i.e. the time it takes for half a sample to decay away.

To understand how a nucleus will decay, you must first look at the mass of a nucleus. You can think of the chart of nuclides with a suppressed third axis of mass. The mass clearly goes up as you increase A, but for a given isobar (constant A), stable nuclei lie at the bottom of a mass parabola. Across the chart, stable nuclei form a valley which the unstable nuclei decay towards and the difference between masses is one of the principal factors determining how fast or what decay modes are available. If the mass of a neutron-rich parent nucleus (N,Z) is larger than the daughter nucleus (N-1,Z+1), then β^--decay will change a neutron to a proton. If the mass of a proton-rich parent nucleus (N,Z) is larger than the daughter nucleus (N+1,Z-1), then two potential decay branches are available, electron capture (εc) and β^+, to change a proton to a neutron. Again, the difference in mass becomes important because β^+-decay is only possible when the mass difference is greater than $2m_e$, where m_e = 0.511 MeV/c^2 is the mass of the electron.

This same principle is true for other spontaneous decay modes such as α-emission, p-

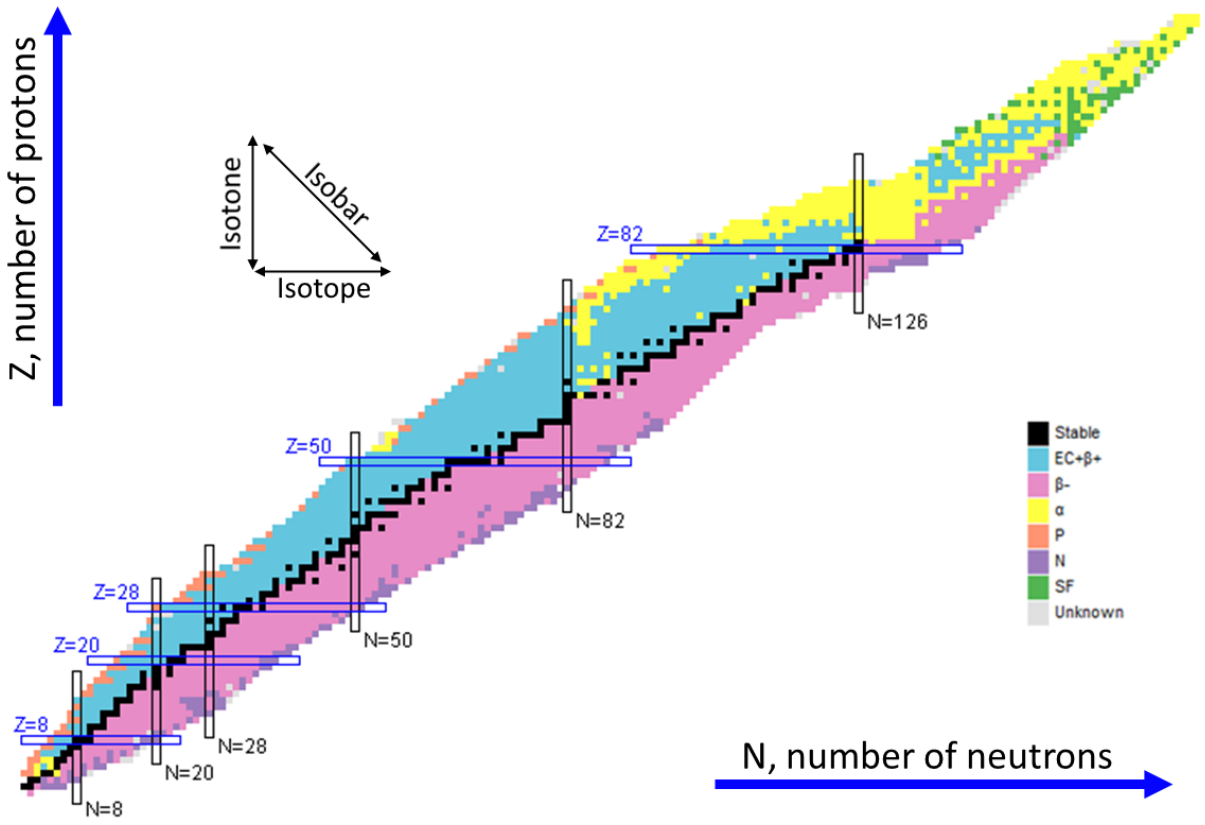

Fig. 1.1: The chart of nuclides (also known as a Segrè chart) Taken from NuDat [1]. Moving vertically increases the number of protons while moving horizontally changes the number of neutrons. Decay type is color coded. Isotopes have constant Z, isotones have constant N, and isobars have constant A.

emission, n-emission, or spontaneous fission. A decay or spontaneous conversion, requires the Q value, defined as the difference in mass between the reactants and products,

$$Q = \sum_{reactants} M_i - \sum_{products} M_j, \tag{1.1}$$

to be greater than zero. For proton, neutron, and alpha decays, instead of a Q value, the separation energy is often used where $S_{n/p/\alpha} = -Q$ so that negative separation energies indicates an energetically allowed, or thermodynamically spontaneous, decay.

Just because a reaction is spontaneous thermodynamically, it does not imply that the decay rate is fast. Kinetically, the rate of decay can be held back by potential-energy barriers. Around a third of the chart has Q_α>0 and more than half could spontaneously fission if not for the presence of barriers. For example, ^{208}Pb has a positive Q_α value of 517 keV [2] and should spontaneously decay but is stable with a lifetime too long to measure. If a ^{208}Pb nucleus was to fission perfectly in half, creating two ^{104}Nb nuclei, it would result in a release of about 122 MeV of energy, but the spontaneous fission of ^{208}Pb is not observed. In quantum mechanics, it is possible for a particles to tunnel through a barrier, and this is discussed later in Section 1.4 for proton decays, but the probability of it occurring dies off exponentially in proportion to the size of the potential barrier. This results in potential energy barriers trapping nucleons in states that meet the energetic requirements for a decay but will never be observed doing so.

1.2 Semi-empirical mass formula

Nuclear mass is a bulk property of all the protons and neutrons interacting together in the nucleus. Bare nucleons have a mass (in energy units) on the order of $m_p \approx m_n \approx$1 GeV while the binding energy between nucleons is $BE_{nuc} \sim$8 MeV/A. The atomic mass is slightly heavier than the bare nucleus, adding on the mass of electrons $m_e = 0.511$ MeV then decremented by the binding energy of all electrons $BE_{elec} \sim$200 keV-1 eV. Together the mass of an atom can be written as follows,

$$M(N,Z) = Z * (m_p + m_e) + N * m_n - BE_{nuc} - BE_{elec}. \tag{1.2}$$

The simplest picture of nuclear binding energy, suggested in the 1930s by G. Gamow, is

the liquid-drop model (LDM) [3]. This was later refined and quantified by Weizäcker and Bethe and called the semi-empirical mass formula (SEMF) [4]. In the LDM and SEMF, the nucleus is a dense, incompressible charged fluid comprised of nucleons held together by the attractive strong nuclear force but kept separate due to a strong repulsive core. Nuclear binding in the SEMF is estimated based on just proton and neutron numbers with just five empirical constants fit to reproduce the masses of atoms. The form is as follows,

$$BE_{nuc}(N,Z) = a_V A - a_S A^{2/3} - a_C \frac{Z(Z-1)}{A^{1/3}} - a_A \frac{(N-Z)^2}{A} + \delta(N,Z), \tag{1.3}$$

where a_V, a_S, a_C, a_A, and δ_0 are the fitted constants. The origins of these terms can be visualized in Fig. 1.2 and are discussed below.

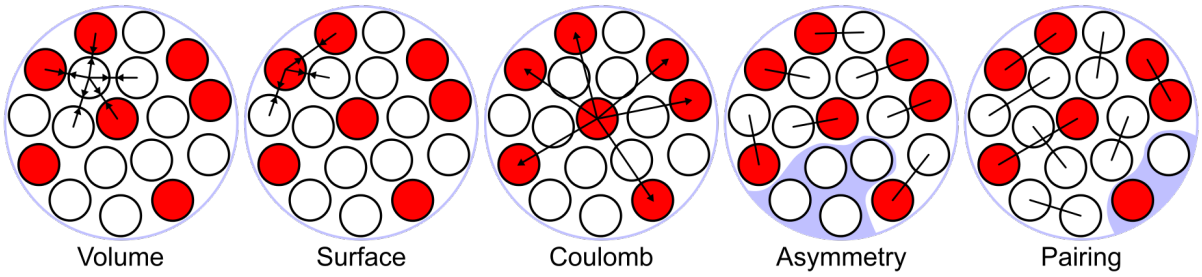

Fig. 1.2: Visual representation of the terms in the SEMF. [5]

The first term, positive and linear in A, is the volume term. This comes from the saturation of the strong force, i.e. the range of the strong force is smaller than the size of the nucleus and extends only to a nucleon's nearest neighbors before the attractive strength falls off. In an infinite system, each nucleon would bind with a set of neighbors and provide a fixed amount of binding energy. This amounts to about 15.5 MeV of binding energy per nucleon.

The second term is the surface term, which is subtractive and lowers the binding energy.

In a finite system, there must be nucleons at the surface of the drop that don't have as many neighboring nucleons to bind with. The surface area of a sphere is $4\pi r^2$ and the radius of a nucleus is approximately $1.2A^{1/3}$ leading to the surface term being proportional to $A^{2/3}$. The reduction of binding from the surface term relative to the volume term is greatest for light nuclei where the surface-to-volume ratio is large. This amounts to a decrease in binding energy and an increase in mass of about 1 MeV/fm^2.

The third term is the Coulomb term. The Coulomb potential between two charges, q_1 and q_2, can be written as,

$$V_C(r) = \frac{1}{4\pi\varepsilon_0}\frac{q_1 q_2}{r}, \tag{1.4}$$

where ε_0 is the permittivity of free space. The Coulomb potential is long range, meaning that every proton in the nucleus will repel every other proton within the nucleus, decreasing the amount the nucleus is bound by. The total electrostatic energy, U, within the nucleus is the sum of the energy between all possible pairs of protons in the nucleus. For an uniform distribution of charge, the energy is the work done in gathering the charges together from infinity. If Q_r is the charge of the sphere with radius r, then the work to add on a charge dQ is,

$$dU = \frac{Q_r dQ}{4\pi\varepsilon_0 r}, \tag{1.5}$$

The charge Q_r is,

$$Q_r = \rho_e \frac{4}{3}\pi r^3, \tag{1.6}$$

where ρ_e is the charge density. This makes the charge added to the sphere to be,

$$dQ_r = \rho_e 4\pi r^2 dr, \tag{1.7}$$

and thus the work bringing the charge together is,

$$dU = \frac{4\pi\rho_e^2 r^4 dr}{3\varepsilon_0}. \tag{1.8}$$

Integrating Eq. (1.8) from r=0 to r=R, the radius of a sharp sphere approximately the size of a nucleus, and replacing the charge density by the total charge over the total volume, $\rho_e = Q/(4/3\pi R^3)$, gives,

$$U = \frac{3}{5}\frac{Q^2}{4\pi\varepsilon_0 R}. \tag{1.9}$$

Here, we get the proportionality from Eq. (1.3) if Q^2 = Z(Z-1) and the radius $R \propto A^{1/3}$.

The fourth term in Eq. (1.3) is the asymmetry energy. This term indicates there is an energy cost to creating an asymmetry in the neutron-to-proton ratio. When following the Pauli exclusion principle, only two nucleons of opposite spin can occupy a level, filling energy levels from lowest to highest according to independent Aufbau principles. With N=Z, the pairs of nucleons fill up the same levels with some spacing Δ between levels. Converting one pair of nucleons to the other, costs a total energy of (2Δ). Doing this again, you have to move the next pair up $3(2\Delta)$ for a total cost of $4(2\Delta)$. To move up n pairs, creating an asymmetry of $(N - Z) = 2n$, the total energy cost is $n^2(2\Delta)$, leading to the $(N-Z)^2$ proportionality in the SEMF. For a three dimensional well, the spacing between energy levels, Δ, is inversely proportional to the volume, giving the 1/A proportionality in the asymmetry term.

The fifth and final term in Eq. (1.3) is the pairing energy. Experimentally, masses of nuclei depend on their even or oddness of each type of nucleon, suggesting a pairing term. Paired nucleons bind more than unpaired nucleons, leading to an increased binding energy if all protons and neutrons are paired and, conversely, a decreased binding energy if the last

proton and neutron aren't paired. This is quantified by the pairing term $\delta(N, Z)$ as,

$$\delta(N,Z) = \begin{cases} +\delta_0/A^{1/2} & even - even \\ 0 & even - odd \\ -\delta_0/A^{1/2} & odd - odd\,, \end{cases} \tag{1.10}$$

where even-even pairing occurs when both protons and neutrons are paired up, even-odd when only one of the two are paired, and odd-odd when neither are paired.

Data for the binding energy per nucleon for stable isotopes is shown in Fig. 1.3 along with the contributions from the SEMF. The figure shows the sharp increase in BE/A as the surface term is quickly reduced in relative importance, a peak of stability around ^{56}Fe, and then a slow decrease in binding as A increases due to the Coulomb and asymmetry terms suppressing the binding. This figure provides major insight into the question of whether a reaction (with fixed total A) has a positive Q value, i.e. a spontaneous decay will move towards higher binding energy per nucleon. As an example, fission occurs in heavy isotopes like ^{235}U because the fission fragments it produces are to the left in Fig. 1.3 and have larger binding energies per nucleon.

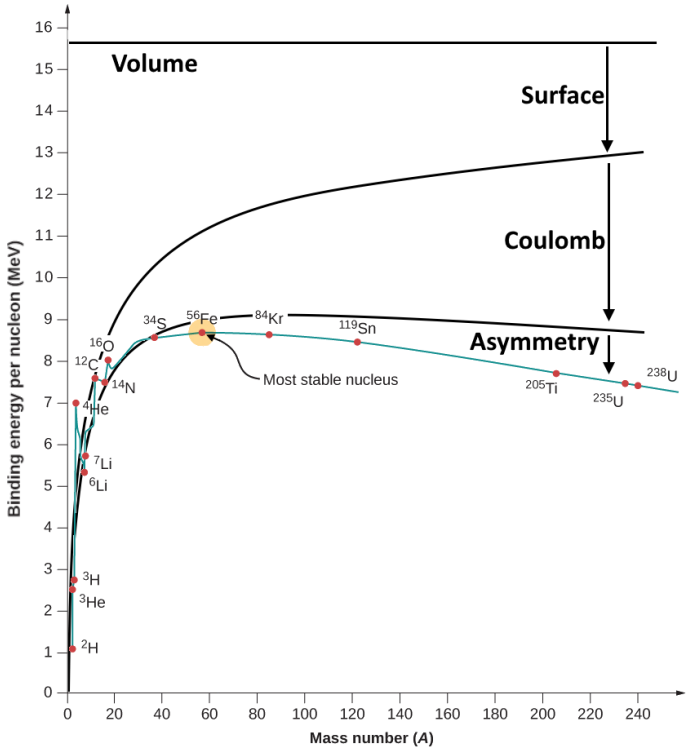

Fig. 1.3: Plot of binding energy per nucleon for stable isotopes adapted from Ref. [6]. Data is shown for specific isotopes in red dots and a blue line while the rough contributions from the SEMF are overlaid in black.

1.3 Nuclear structure

When the SEMF from Section 1.2 is fit to data, it does a good job at describing overall trends, but it becomes clear there are systematic deviations. For example, deviations from this model are shown in Fig. 1.4 where the largest differences occur at set numbers of N. This comes as a result of nuclear structure and shell effects. We see an increase in stability, i.e. more binding, for nuclei that have the number of protons or neutrons equal to 2, 8, 20, 28, 50, 82, and 126. These "magic" numbers arise as a result of nucleons occupying shells with non-uniform gaps between levels, i.e. the Δ used in the analysis of the asymmetry term

in the SEMF is not a constant. This stability can show up many ways and helps explain the natural abundances of isotopes in nature, the large number of stable isotopes or isotones at magic numbers, trends in nuclear masses, and the double-humped mass distribution observed in fission.

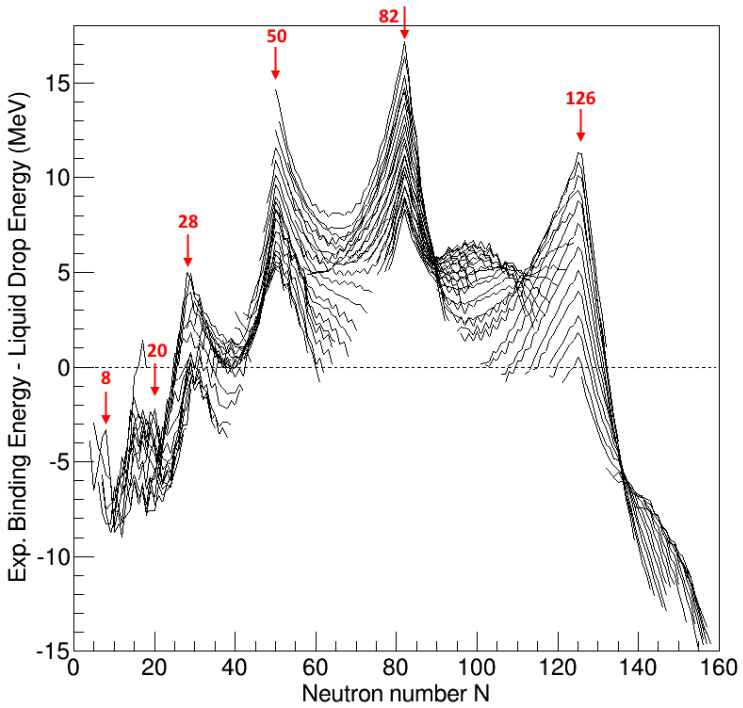

Fig. 1.4: Difference between the SEMF (or LDM) and measured binding energies for isotopic chains of each element. Shell effects can be seen as peaks at the magic numbers N = 8, 20, 28, 50, 82, and 126. [7]

1.3.1 Independent-particle model

The combined effect of nucleons interacting within a nucleus results in an attractive potential that traps protons and neutrons. To understand the structure of the nucleus, a reasonable starting point is a model where a nucleon does not interact with each other nucleon independently but instead interacts with a central potential produced by the combined effect of

all nucleons. This description of nuclei is called the independent-particle model.

The exact form of the nuclear potential is unknown but the simplest picture for this central potential is that of the harmonic oscillator, i.e. parabolic in shape. The harmonic oscillator potential has the unique property that solutions to Schrödinger's equation results in equally-spaced energy levels. The levels are defined by their principle quantum number, N, with energy $N\hbar\omega$, where ω is the oscillation frequency. Issues quickly arise for the harmonic oscillator potential. First, the harmonic oscillator potential has a rounded bottom while heavier nuclei with large volumes need a potential that saturates. Second, the harmonic oscillator infinitely increases with no limit to how many levels can be bound while we know there is a limit to the chart of nuclides. The finite square well, having a flat, uniform bottom and sharp edges, offers a direct improvement to these issues. It also removes the angular momentum degeneracy creating a split between levels with the same principle quantum number but different orbital angular momentum numbers $\ell = 0$, 1, 2, 3, 4, and 5 (labeled as s, p, d, f, h, and i, respectively). This reproduces the magic numbers 2, 8, and 20 but fails to reproduce the higher magic numbers.

The central potential can be improved if the edges of the well are rounded to give a diffuse edge to the nucleus. The Woods-Saxon potential is a commonly used form given by,

$$V(r) = \frac{-V_0}{1 + exp(\frac{r-R}{a})}, \tag{1.11}$$

where V_0 is the well depth, a is the diffuseness of the surface, and R is the radius of the nucleus. The final addition to the potential is the spin-orbit coupling, introduced in 1949 by Goeppert-Mayer [8] and at the same time by Haxel, Jensen, and Suess [9]. The spin-orbit coupling is an interaction between the orbital angular momentum, ℓ, and the spin angular momentum, s, to give a potential $V_{LS} \propto \boldsymbol{\ell} \cdot \boldsymbol{s}$. This interaction breaks the degeneracy between

levels with different values of $\mathbf{J} = \boldsymbol{\ell} + \boldsymbol{s}$, lowering $J_>$ that has $\boldsymbol{s} = 1/2$ (i.e. parallel to $\boldsymbol{\ell}$), and raising $J_<$ that has $s = -1/2$. This is the opposite of what one finds in the strictly relativistic orbital electron spin-orbit splitting.

This sequence of improvements in potential, from a harmonic oscillator to a square well, to a Woods-Saxon, to including the spin-orbit, is shown in Fig. 1.5. The observed magic numbers are recreated when the spin-orbit coupling is included and are shown in boxed numbers on the right-hand side.

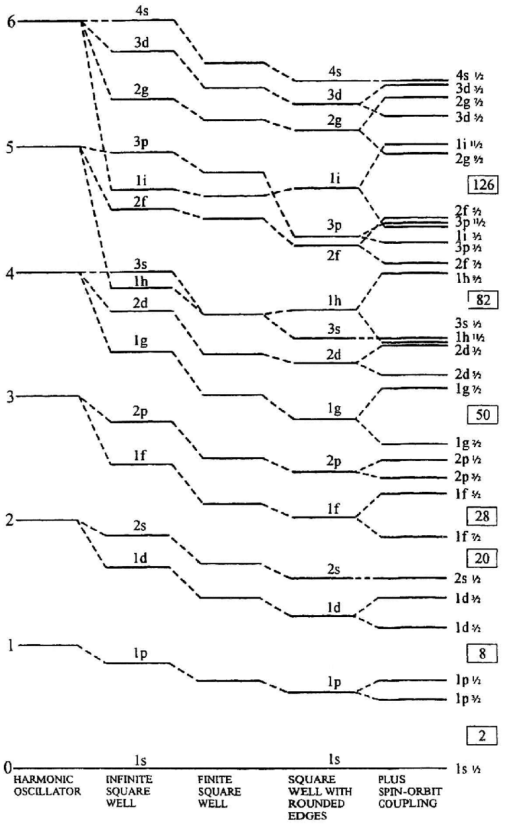

Fig. 1.5: Calculated single-particle levels for different central potentials starting with the harmonic oscillator, then the infinite and finite square wells, then the square well with rounded edges (Woods-Saxon shape), and finally when the spin orbit coupling is added. The final potential results in levels that have gaps at the observed magic numbers shown on the right in boxes at 2, 8, 20, 28, 50, 82, and 126.

1.3.2 Configuration Interactions

In the independent-particle model, we looked at single-particle interactions with a central potential to form single well-defined orbitals. This works well to recreate the magic numbers and can explain structure that is dominated by just one or two unpaired particles or holes. For example, moving from a doubly closed shell like ^{40}Ca with a 0^+ ground state to ^{41}Ca, puts a single neutron in the $f_{7/2}$ orbital, so the ground state will have a spin-parity $J^\pi = 7/2^-$. For most of the chart of nuclides, the picture is more complicated and a many-body physics approach is required.

Configuration interaction (CI) calculations, also commonly called shell-model calculations, is an approach to solve the many-body quantum problem that incorporates valence nucleons defined by occupancies of partially filled single-particle quantum states. The first step in CI is choosing the active model space. From the independent-particle model, you choose an inert core nucleus and a valence space where excitations will take place. The valence space orbits are typically chosen such that a calculation occurs within one or two harmonic oscillator shells from Fig. 1.5 such as the s, p, sd, or pf shells in light nuclei. This reduces the model space and therefore the calculation time. The second part of a CI calculation is determining the effective two-body interaction between nucleons. Removing the inert core nucleons forces the calculation to use an effective interaction to account for those missing nucleons in the calculation. In a phenomenological approach, the interaction is parameterized and then fit to data. Research over time has produced many of these codes and interactions with examples of codes including Oxbash [10], nushell [11], KSHELL [12], and ANTOINE [13] and examples of interactions including USD(A,B,C) [14, 15] or the ZBM2 [16].

The CI or shell-model calculations are a versatile tool for studying light-to-medium mass

nuclei. They have been used to calculate a wide range of observables including: energy levels, radii, matrix elements, spectroscopic factors, magnetic moments, electron scattering, and beta decay. These interactions work reasonably well at reproducing selected experimental data but some consideration is required when attempting to calculate nuclei with large degrees of collectivity and when looking at an open quantum system with excitations in the continuum. Shell model calculations were employed throughout the work presented in this thesis serving as valuable benchmarks.

1.3.3 Electromagnetic transitions

The energy of an electromagnetic radiation field can be described mathematically in terms of a multipole expansion in spherical harmonics, Y_ℓ^m, with orbital angular momentum ℓ and magnetic substates m. The terms in the expansion correspond to the increasing angular momentum quantum numbers that have 2^ℓ-poles in the field. These are named: ℓ=0 for a monopole, ℓ=1 for a dipole, ℓ=2 for a quadrupole, ℓ=3 for a octupole, and so on for higher multipolarities. The strength of each multipole field is proportional to the radius as $r^{-(\ell+1)}$, resulting in a rapid convergence, with the lowest order multipolarity being the most important.

These multipolarities are used to classify transitions between states in a nucleus that couple to the electromagnetic field, such as γ-ray emission or Coulomb excitation. For the emission of a γ-ray with intrinsic spin $s = 1$ and spin projection $m_s = \pm 1$, the photon which couples the transition has angular momentum,

$$\boldsymbol{\lambda} = \boldsymbol{\ell} + \boldsymbol{s}, \tag{1.12}$$

with new magnetic substates, μ, given by,

$$-\mu < \lambda < \mu. \tag{1.13}$$

The change in parity, $\Delta\pi$, depends on on the parity of the photon coupled to the change in orbital angular momentum as $\Delta\pi = (-1)^{\ell+1}$. If the photon changes the charge distribution, it is an electric transition with $\ell = \lambda \pm 1$ and if the photon changes the current distribution, it is an magnetic transition with $\ell = \lambda$. For a given transition from $J_i^{\pi_i} \rightarrow J_f^{\pi_f}$, angular momentum gives the selection rules,

$$\boldsymbol{J}_i^{\pi_i} \rightarrow \boldsymbol{J}_f^{\pi_f} + \boldsymbol{\lambda}, \tag{1.14}$$

and

$$|J_i^{\pi_i} - J_f^{\pi_f}| \leq \lambda \leq J_i^{\pi_i} + J_f^{\pi_f}. \tag{1.15}$$

The monopole, $J_i^{\pi_i} = 0^+ \rightarrow J_f^{\pi_f} = 0^+$ transition is forbidden because the photon has non-zero angular momentum. If the nucleus starts with zero angular momentum and a photon must carry away some in the transition, the final nuclear state cannot also have zero angular momentum. The lowest allowed multipolarity, $\lambda = |J_i^{\pi_i} - J_f^{\pi_f}|$, will dominate the transition rate due to the rapid convergence of the multipole expansion.

For a transition, the decay rate can be calculated using Fermi's golden rule,

$$\Lambda = \frac{2\pi}{\hbar} \left|\langle f|H'|i\rangle\right|^2 \frac{dN(E_f)}{dE}, \tag{1.16}$$

where $\langle f|H'|i\rangle$ is matrix element determined by the overlap of the final and initial wave function with the interaction Hamiltonian, H', treated as a perturbation to the free particle

Hamiltonian. The quantity $dN(E_f)/dE$, is the density of states at the final energy of the transition. For an electromagnetic transition, the Hamiltonian is replaced by the electric or magnetic transition operators. The electric operator is given by,

$$\hat{Q}_{\lambda\mu} = \sum_i e_i \, r_i^\lambda \, Y_\lambda^{\mu*}(\theta_i, \phi_i), \tag{1.17}$$

where e_i is the charge of particle i. The magnetic operator is given by,

$$\hat{M}_{\lambda\mu} = \mu_N \sum_i \left(g_{s,i} \, \boldsymbol{s_i} + \frac{2}{\lambda+1} \, g_{\ell,i} \, \ell_i \right) \cdot \nabla \left[r_i^\lambda \, Y_\lambda^{\mu*} \left(\theta_i, \phi_i\right) \right], \tag{1.18}$$

where μ_N is the nuclear magneton, g_s and g_ℓ are spin and orbital angular momentum gyromagnetic ratios. For an electromagnetic transition, the perturbation Hamiltonian is proportional to the electric or magnetic transition operators. With this replacement, the matrix element in Eq. (1.16) is now $\langle f|\hat{O}_{\lambda\mu}|i\rangle$, where $\hat{O}_{\lambda\mu}$ is either Eq. (1.17) or (1.18), while $\langle f|$ and $|i\rangle$ are short-hand for the relevant final and initial state quantum numbers. Through the Wigner-Eckart theorem, the matrix element can be averaged over the magnetic substates (μ), which are not typically observed individually in experiments, resulting in,

$$\langle f|\hat{O}_{\lambda\mu}|i\rangle = (2J_i+1)^{-1/2} \langle f||\hat{O}_\lambda||i\rangle, \tag{1.19}$$

where the double-bar notation of $|\langle f||O_\lambda||i\rangle|$ is the reduced matrix element. Squaring the matrix element, we define the $B(\pi\lambda)$ as the reduced transition probability (often also called the reduced matrix element), given by,

$$B(\pi\lambda, J_i \to J_f) = (2J_i+1)^{-1} \left| \langle f||\hat{O}_\lambda||i\rangle \right|^2. \tag{1.20}$$

The $B(\pi\lambda, J_i \to J_f)$ can be related to the inverse transition rate $B(\pi\lambda, J_f \to J_i)$ as,

$$B(\pi\lambda, J_i \to J_f) = \frac{2J_f + 1}{2J_i + 1} B(\pi\lambda, J_f \to J_i). \tag{1.21}$$

With the reduced transition probability defined, the decay rate from Fermi's golden rule in Eq. (1.16) can be solved. For an electric transition, the rate is given by,

$$\Lambda(E\lambda) = \frac{e^2 8\pi\,(\lambda+1)}{\hbar\lambda\left[(\lambda+1)!!\right]^2}\, B(E\lambda)\, \left(\frac{E_\gamma}{\hbar c}\right)^{2\lambda+1}, \tag{1.22}$$

and for a magnetic transition, by,

$$\Lambda(M\lambda) = \frac{\mu_N^2 8\pi\,(\lambda+1)}{c^2\hbar\lambda\left[(\lambda+1)!!\right]^2}\, B(M\lambda)\, \left(\frac{E_\gamma}{\hbar c}\right)^{2\lambda+1}. \tag{1.23}$$

With the transition rate, the mean life-time, $\tau = 1/\Lambda$, and the decay width, $\Gamma = \hbar\Lambda$, are also known. Typically the mean life-time ($\tau = t_{1/2}/\ln(2)$)is measured in an experiment, and the reduced transition probability can be extracted from that. Common methods of measuring these extremely short lifetimes (in the range of 10^{-15} to 10^{-9} seconds) include the recoil distance method and the Doppler-shift attenuation method [17], while Chapter 5 discusses the intermediate energy Coulomb excitation method.

The $B(E2, 0^+ \to 2^+)$, measured for ^{36}Ca in Chapter 5, is a reduced electric-quadrupole transition rate. Measurements of $B(E2)$ strength are common because of the availability of even-even nuclei which have a 0^+ ground state and a low lying excited 2^+ state. These can be compared to a single-particle transition rate given by the Weisskopf estimates [18]. Large $B(E2)$ values compared to the Weisskopf estimates indicate a more collective motion of protons and neutrons in the excitation. $B(E2)$ strengths are smallest near closed shells and largest between shells where large deformation can occur. In the Hill-Wheeler param-

eterization [19], the deformation can be modeled as the radius R being deformed, from R_0 as,

$$R(\theta, \phi) = R_0 \left(1 - \beta_2 Y_2^0(\theta)\right), \tag{1.24}$$

where the deformation parameter, β_2, is given by,

$$\beta_2 = \frac{4\pi}{3ZR_0^2}\sqrt{B(E2\uparrow)/e^2}. \tag{1.25}$$

By convention, if β_2 is given as a positive value, the nucleus has a prolate deformation, and if β_2 is negative, the nucleus has an oblate deformation.

1.4 Proton emission to study open quantum systems

As discussed earlier, proton emission can occur in the ground state when the separation energy becomes negative. On the chart of nuclides, negative proton separation energies define the proton drip line. For light isotopes beyond the proton drip line, lifetimes are extremely short and the life-time is measured by the width of the resonance. For a state that has a width of 100 keV, the half-live is only 4.6×10^{-21} s (related through Eq. (1.28) discussed later). For heavy isotopes, the partial proton lifetimes have been observed as large as 100 s for ^{105}Sb where the proton decay branch is competing against the β^+ decay branch [20, 21]. Proton decay can also occur in excited states if the state is above a decay threshold set by the proton separation energy. The work presented in this thesis will handle both cases, with Chap. 3 discussing an excited state in ^{7}Li above the proton decay threshold, Chap. 4 discussing an excited state with a branching ratio between proton and gamma decay, and finally in Chap. 6 discussing ^{34}K, ^{37}Sc, and ^{38}Sc which are isotopes beyond the proton drip line.

The nuclear chemistry group at Washington University in St. Louis has studied a large collection of proton emitting nuclei including 9 first observed by our group and collaborators. The first observations of light proton emitters beyond the proton drip line associated with the WashU efforts are highlighted in green in Fig. 1.6. Among these cases are the two-proton-emitter ^{11}O [22], the four-proton-emitter ^{18}Mg [23], and the recent five-proton-emitter ^{9}N [24]. The work in Chap. 6 discusses ^{34}K, ^{37}Sc, and ^{38}Sc, the heaviest nuclei yet studied by the WashU effort.

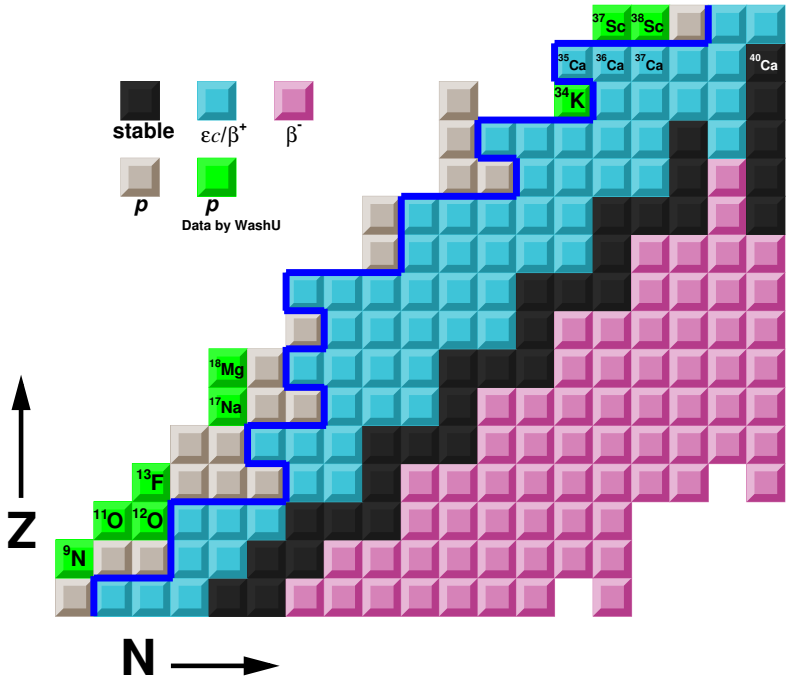

Fig. 1.6: Chart of the nuclides zoomed in on light nuclei. Proton emitters beyond the drip line that have been discovered by the WashU group are highlighted in bright green.

Weakly bound and unbound states can couple strongly to the scattering continuum and therefore are often required to be treated as open quantum systems. The quasi-bound nature of one or more protons leads to extended wave functions that have significant overlap with

continuum wave functions. An example of such an effect is the Thomas-Erhman shift, which lowers the energy of continuum states with large s-wave character compared to the same states in the mirror nucleus which are bound [25, 26]. For weakly-bound systems, or systems with separation energies just above zero, nuclei have been observed to have an extended low-density skin region, resulting in what are called halo nuclei. In order to calculate the properties of halo nuclei, such as the two-neutron halo in ^{11}Li[27] or the proton halo expected for ^{8}B [28], an open quantum system treatment is required. Proton emission provides a test for quantum calculations which include coupling to the continuum as a facet of the many-body problem.

1.4.1 Barriers to proton emission

If a nucleus is unbound to particle emission, it may be quasi-bound if there exists a potential barrier that traps the particle from escaping the nucleus. A proton must tunnel through the Coulomb barrier and perhaps an angular momentum barrier to escape the nucleus. An example of a quasi-bound proton probability distribution trapped by the presence of a presence of a barrier is shown in Fig. 1.7.

Imagine a proton approaching a nucleus. As the positively-charged proton approaches the positively-charged nucleus, the Coulomb potential from Eq. (1.4) is inversely proportional to the radius, r, increasing as $1/r$. This rapidly approaches infinity for a perfect point source but the nucleus has a definite size with radius R $\approx 1.2A^{1/3}$. If the approaching proton has a high enough energy to touch the nucleus, then the strong force overwhelms the Coulomb force and the overall potential becomes attractive. The same barrier that repels the approaching proton also inhibits a proton from leaving the nucleus.

In the classical picture, a nucleon has angular momentum because it is orbiting a core.

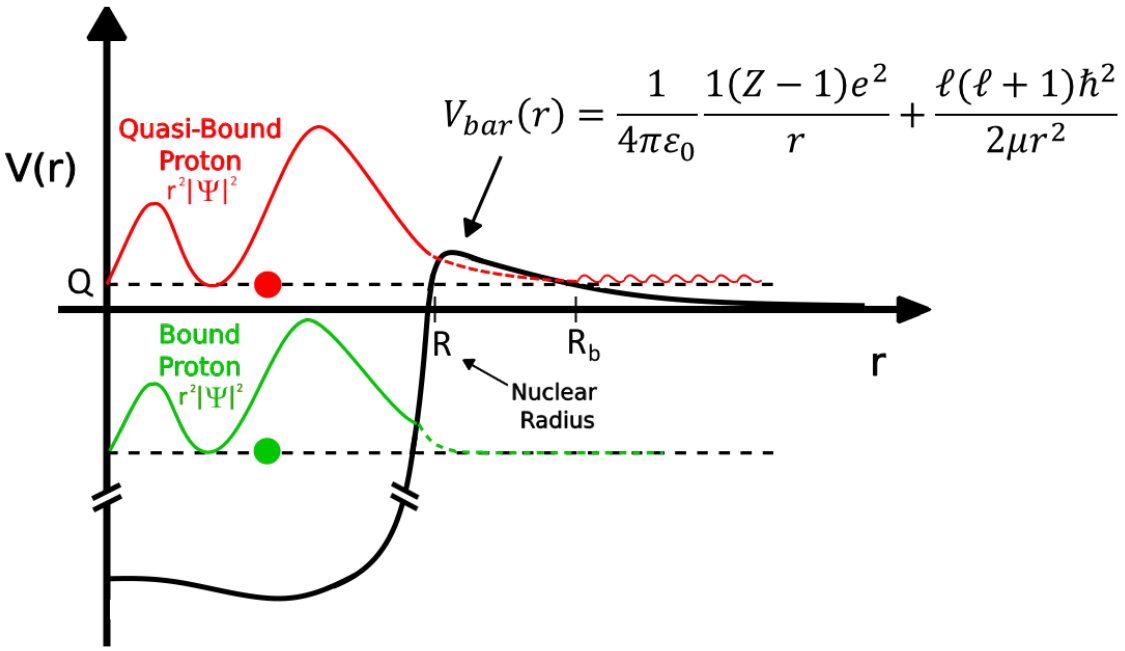

Fig. 1.7: The probability distributions for bound and quasi-bound protons trapped by the presence of the Coulomb and angular momentum barrier V_{bar}.

The angular momentum must be conserved as the nucleon's radius of orbit increases or decreases. For a nucleon with a quantized angular momentum, the barrier is as follows,

$$V(r) = \frac{\ell(\ell+1)\hbar^2}{2\mu r^2}, \tag{1.26}$$

where μ is now the reduced mass between the nucleon and the core. If the particle moves radially inwards, the potential shoots up, requiring more and more energy to conserve angular momentum. The opposite is also true, that as the particle moves outwards, less energy is required creating a repulsive potential. This creates the angular-momentum barrier (or centrifugal barrier) that a particle decay must tunnel through to escape the nucleus. For proton emission, the angular momentum barrier is less significant compared to the Coulomb

barrier as it dies off with a $1/r^2$ form versus the 1/r form in the Coulomb potential but it can play a large role in light nuclei, with small Coulomb barriers, and in neutron emission, for which there is no Coulomb barrier.

1.4.2 Quantum tunneling

Emission rates for a quasi-bound proton follows a theory similar to that used to treat alpha decay. When the energy of the proton is positive but less than the barrier, the proton must tunnel through the classically forbidden region to escape. The partial proton width, Γ_p, can be written as

$$\Gamma_p = (C^2S)F\frac{\hbar^2}{4\mu}T \tag{1.27}$$

where (C^2S) is the spectroscopic factor for finding the proton in the correct orbital, F is a normalization factor discussed in further detail in [29], and T is the transmission coefficient. The partial decay width is related to the decay rate, Λ, and the half-life by,

$$\Gamma_p = \hbar\Lambda, \quad and \quad t_{1/2} = \frac{\hbar\, ln(2)}{\Gamma_p}. \tag{1.28}$$

To calculate the transmission coefficient from a theoretical approach, there are four main methods: Distorted wave born approximation (DWBA), two-potential approach, the Wentzel-Kramers-Brillouin (WKB) approximation, and R-matrix method [30]. The last two of which will be briefly discussed.

In Fig. 1.7, there are three main regions: inside the nucleus with $r < R$, inside the classically forbidden region $R < r < R_b$ where R_b is the radius at which the barrier drops to Q (shown as dotted line for the wave function), and outside the nucleus where the proton is

a free particle with $r > R_b$. The wave vector, κ, is given by,

$$\kappa = \sqrt{\frac{2\mu}{\hbar^2}(Q - V_{bar}(r))}, \tag{1.29}$$

with Q being the Q-value and V_{bar} being the potential barrier. If the barrier is large and the inverse of the wave vector is small and slowly varying compared to the size of the system, then the WKB approximation is valid and the transmission coefficient is,

$$T_{WKB} = exp\left(-2\int_R^{R_b}\sqrt{\frac{2\mu}{\hbar^2}(Q - V_{bar}(r))}dr\right). \tag{1.30}$$

1.4.3 R-matrix

At its core, R-matrix theory is a formulation developed to treat resonances as a result of nuclear scattering. For a complete review of R-matrix theory, I will point to a detailed review article by Lane and Thomas [31], but here I will show enough to demonstrate its usefulness for proton emission. Guidance and arguments are taken from Refs. [32] and [33]. The phenomenological R-matrix method parameterizes various physical processes to determine collision matrices and cross sections. Central to this formulation, the wave function for a scattering channel, c, between two particles is divided into an "internal" region corresponding to the formation of a compound nucleus, and an "external" region corresponding to channels that cause or result from the formation of a compound nucleus. For each scattering partial wave and channel, the division occurs at a sharp surface at radius, a, called the channel radius.

External to the channel radius, incoming and outgoing channels are in the presence of a Coulomb and angular momentum potential. The wave-function solutions for positive-energy incoming and outgoing waves can be expressed in terms of regular (F) and irregular (G)

Coulomb functions. At large r, their asymptotic forms are:

$$F_l(r) \xrightarrow[r\to\infty]{} \sin\left(kr - \eta\log(2kr) - (1/2)\ell\pi + \sigma_\ell\right) \tag{1.31}$$

$$G_l(r) \xrightarrow[r\to\infty]{} \cos\left(kr - \eta\log(2kr) - (1/2)\ell\pi + \sigma_\ell\right), \tag{1.32}$$

where k is the wave vector of a free particle (defined the same as Eq. (1.29) except $V_{bar} = 0$ and $Q = E$ is energy of the free particle), η is the Summerfeld parameter, and σ_ℓ is the Coulomb phase shift. The Summerfeld parameter and Coulomb phase shift are given by,

$$\eta = Z_1 Z_2 e^2 \mu/(\hbar k), \tag{1.33}$$

and

$$\sigma_\ell = \arg\Gamma\left(1 + \ell + i\eta\right). \tag{1.34}$$

where Γ in this one instance is the Euler function, and μ is the reduced mass between the two particles in the scattering channel. The wave-function solutions can now be expressed for the positive-energy incoming, I_l^+, and outgoing, O_l^+, waves as,

$$I_l^+(r) = (G_\ell - iF_\ell)\exp(i\omega_\ell) \tag{1.35}$$

$$O_l^+(r) = (G_\ell + iF_\ell)\exp(-i\omega_\ell), \tag{1.36}$$

where

$$\omega_\ell = \sum_{n=1}^{\ell} \arctan\eta/n. \tag{1.37}$$

Outside, we can define the penetrability P and the shift function S as a function of the energy, E, related to k via Eq. (1.29), which will be useful later. The penetrability is related

to the Coulomb wave functions at the channel radius by,

$$P_\ell(E) = \frac{ka}{F_\ell(ka)^2 + G_\ell(ka)^2} \tag{1.38}$$

and the shift function is,

$$S_\ell(E) = ka\frac{F_\ell(ka)'F_\ell(ka) + G_\ell(ka)'G_\ell(ka)}{F_\ell(ka)^2 + G_\ell(ka)^2}, \tag{1.39}$$

where F'_ℓ and G'_ℓ are the derivatives with respect to kr.

Internal to the channel radius, the full wave function for a channel, Ψ_c, can be expanded in terms of mutually orthogonal eigenfunctions,

$$\Psi_c = \sum_\lambda A_\lambda X_\lambda \tag{1.40}$$

where each X_λ is a resonant state belonging to an eigenenergy of E_λ. The matching boundary condition between internal and external waves is imposed at the channel radius given by,

$$a\left(\frac{dX_\lambda}{dr}\right)|_{r=a} = b\,X_\lambda(a), \tag{1.41}$$

where b is the boundary condition. Both a and b are specified by the user. The value of a is typically chosen just beyond the extent of the nuclear potential for that channel. The final results should be insensitive to small changes in a and independent of the boundary condition.

The expansion coefficients of Eq. (1.40) must satisfy,

$$A_\lambda = \int X_\lambda * \Psi_c\, dV, \tag{1.42}$$

integrating over the full internal volume of the configuraton space. Through an application of Green's theorem [32], the coefficients A_λ are solved for to give,

$$A_\lambda = \sum_c \sqrt{\frac{\hbar^2}{2\mu_c\, a}}\, \frac{\gamma_{\lambda c}}{E_\lambda - E} \left[\Psi_c'(a) - b\, \Psi_c(a)\right]. \tag{1.43}$$

In the equation above, $\gamma_{\lambda c}$ is the reduced width amplitude given by,

$$\gamma_{\lambda c} = \sqrt{\frac{\hbar^2}{2\mu_c a_c}} \int \Psi_c^* X_\lambda dS, \tag{1.44}$$

where the integral is over the surface between internal and external wave function. Using Eq. (1.40), and looking at a transfer between channels, we now have the internal wave function,

$$\sqrt{\frac{\hbar^2}{2\mu_c\, a_c}}\, \Psi_c(r) = \sum_{c'} \frac{\hbar^2}{2\mu_{c'}\, a} \boldsymbol{R_{cc'}} \left[\Psi_{c'}'(r) - b\, \Psi_{c'}(r)\right], \tag{1.45}$$

where we define the R matrix for multiple channels as,

$$\boldsymbol{R_{cc'}} = \sum_\lambda \frac{\gamma_{\lambda c}\gamma_{\lambda c'}}{E_\lambda - E} \tag{1.46}$$

The S matrix, or scattering matrix, can be used to relate the initial and final state in a scattering process. For a single isolated channel, the S matrix is related to a phase shift, δ, as,

$$\boldsymbol{S} = \exp(2i\delta). \tag{1.47}$$

To relate the R matrix to the the S matrix, generally,

$$\boldsymbol{S} = \sqrt{\frac{\hbar^2}{2\mu_c\, a}}\, \frac{H_\ell^- - a\boldsymbol{R}\left(H_\ell^{-\prime} - \frac{b}{a} H_\ell^-\right)}{H_\ell^+ - a\boldsymbol{R}\left(H_\ell^{+\prime} - \frac{b}{a} H_\ell^+\right)}, \tag{1.48}$$

where $H_\ell^\pm$ are the Hankel functions. To simplify this, we look at s-wave neutron scattering on a target so there is no Coulomb or angular momentum potentials. This simplifies the Hankel functions so they are simply $H_0^\pm = e^{\pm ika}$. Choosing the boundary condition to be $b = 0$ gives,

$$\boldsymbol{S} = e^{-2ika}\frac{1 + ika\boldsymbol{R}}{1 - ika\boldsymbol{R}}. \tag{1.49}$$

From comparing this to Eq. (1.47), we can see a split in the phase shift. There is a hard-sphere contribution, e^{-2ika}, and a resonance contribution $(1 + ika\boldsymbol{R})/(1 - ika\boldsymbol{R})$, i.e. the phase shift is now,

$$\delta = \phi + \delta_R, \tag{1.50}$$

with a hard-sphere phase shift $\phi = -ka$ and δ_R representing the resonance phase shift. In the more general case of a isolated resonance, Eq. (1.48) can be written in terms of the shift function and penetrability of a hard sphere to give,

$$\boldsymbol{S} = \frac{1 - \boldsymbol{R}\,(S - b) + i\boldsymbol{R}P}{1 - \boldsymbol{R}\,(S - b) - i\boldsymbol{R}P}\,e^{2i\phi}, \tag{1.51}$$

with resonance phase shift,

$$\delta_R = \tan^{-1}\left(\frac{\boldsymbol{R}P}{1 - \boldsymbol{R}(S - b)}\right). \tag{1.52}$$

To relate Eq. (1.51) to experimental quantities, we choose b=0 and re-write the S matrix using the definition of $\boldsymbol{R}$ such that it is now,

$$\boldsymbol{S} = \frac{E - (E_\lambda - \gamma_\lambda^2 S + i\gamma_\lambda^2 P)}{E - (E_\lambda - \gamma_\lambda^2 S - i\gamma_\lambda^2 P)}e^{2i\phi}. \tag{1.53}$$

If the shift and penetrability are approximately constant across a resonance, then we can

substitute in the formal definitions of the resonance position and width,

$$E_r^f = E_\lambda - \gamma_\lambda^2 S \tag{1.54}$$

$$\Gamma^f = 2\gamma_\lambda^2 P. \tag{1.55}$$

Substituting for the formal definitions, the S matrix can now be written as,

$$\boldsymbol{S} = \frac{E - E_r^f - i\Gamma^f/2}{E - E_r^f + i\Gamma^f/2} e^{2i\phi}. \tag{1.56}$$

One of the benefits of transferring to the S matrix formalism, is that the cross section of elastic scattering can be easily determined. The cross section for a single resonance elastic scattering is given by,

$$\sigma_\ell = \frac{\pi}{k^2}(2\ell + 1)\left|1 - \boldsymbol{S}_\ell\right|^2, \tag{1.57}$$

for one partial wave. If the isolated resonance is sufficiently above the channel threshold in a region where the shift and penetrability are constant, we can substitute in the resonance part of Eq. (1.56) to get a cross section for the resonance elastic scattering,

$$\sigma_\ell \propto \left|1 - \boldsymbol{S}_\ell\right|^2 = 4\frac{\Gamma^2/4}{(E - E_r)^2 + \Gamma^2/4}, \tag{1.58}$$

which is the Breit-Wigner line shape used in fitting peaks in IMS. When the energy dependence does matter, such as in the case of dealing with a very wide resonance or a resonance very close to a threshold, the Thomas approximation is used, which assumes the shift function is locally linear [34]. In general the observed resonance energy and width are given by,

$$E_r^{obs} = E_\lambda - \gamma_\lambda^2[S(E^{obs}) - b] \tag{1.59}$$

$$\Gamma^{obs} = \frac{2\gamma_\lambda^2 P(E_r^{obs})}{1 + \gamma_\lambda^2 S'(E_r^{obs})}, \tag{1.60}$$

where S' is the derivative of the shift function in terms of energy. Another popular choice of the boundary condition is $b = S(E^{obs})$ (natural boundary condition) which makes the resonant energies the same as the eigenenergies of the internal eigenfunctions. The fits in Chapter 3 using R-matrix lineshapes used the energy dependence of E_r^f and Γ^f in Eqs. (1.54) and (1.55) to produce an asymmetric line shape. This was essential for the case of a wide state just above threshold.

1.5 Nucleosynthesis

Nucleosynthesis is the name for a collection of processes that create elements heavier than hydrogen through fusion and other reactions that occur in the Big Bang and in stellar environments. There are many sites in which nucleosynthesis can occur but the first happened at the birth of our universe. Light elements were created during the Big Bang as the hot dense quark-gluon plasma rapidly expanded and cooled, freezing out protons and neutrons. The protons and neutrons reacted to form mostly hydrogen and helium, but also initially created very small percentages of deuterium, tritium (which decays to ^{3}He), ^{3}He, ^{7}Li, and ^{7}Be (which decays to ^{7}Li) through the reaction network shown in Fig. 1.8.

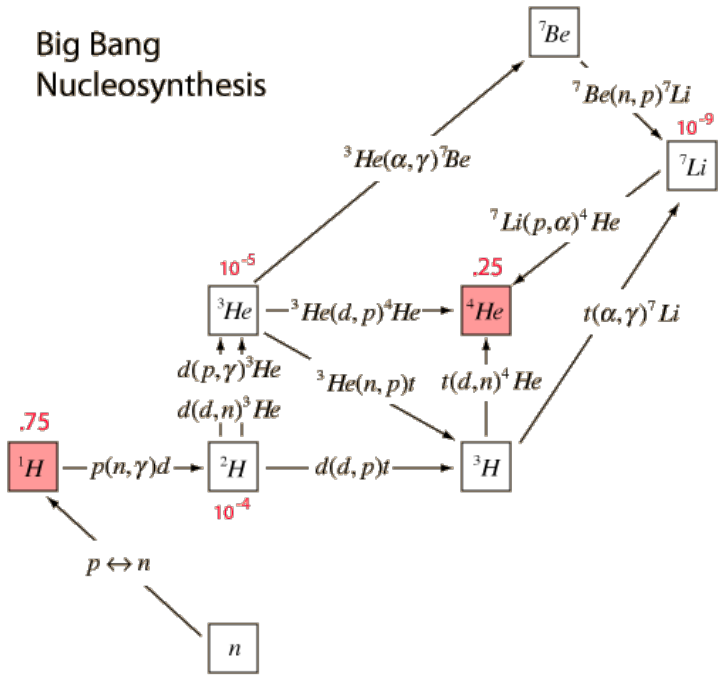

Fig. 1.8: Reaction network modeling the Big Bang nucleosynthesis. Afterwords, roughly 3/4 of all matter was ^{1}H and 1/4 was ^{4}He with very small fractions of the other isotopes shown in red. [35]

The next place to look for the creation of elements is in stars, forming from the hydrogen and helium created in the Big Bang which coalesce as gravity slowly pulls large amounts of matter together. It is in the core of stars that the pressure and temperatures are high enough that fusion reactions can occur. The proton-proton chain (pp-chain) is a fusion process that converts four protons into a helium nucleus. The main branch of the proton-proton process is seen in Fig. 1.9(a). The initial step in hydrogen burning, $p+p \rightarrow d+e^{+}+\nu$, is slow and is the rate limiting step, requiring the weak force to convert a proton into a neutron. In older, more massive stars, temperatures can get high enough that instead of waiting for the pp-chain, the Carbon-Nitrogen-Oxygen cycle (CNO cycle) accelerates hydrogen burning in stars. The CNO cycle follows the chain of reactions in Fig. 1.9(c), in essence, ^{12}C acts as a nuclear reaction catalyst which outcompetes the slow initial step in the pp-chain.

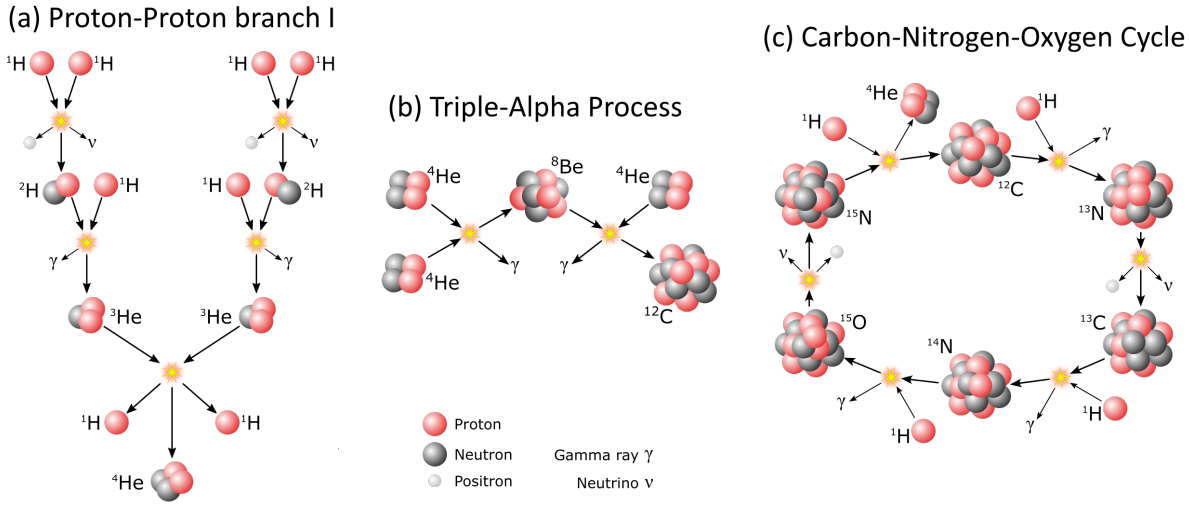

Fig. 1.9: (a)Proton-proton chain Branch-I makes up the majority of proton fusion in stars to make ^{4}He. (b) Triple-alpha process fuses three ^{4}He nuclei together to form ^{12}C. (c) The CNO cycle accelerates the fusion of protons to create ^{4}He nuclei at high temperatures [36].

An important quirk of the chart of nuclides is that there are no stable A=5 or A=8 systems. This makes proton capture infeasible for explaining the abundances of heavier nuclei as they produce the A=5 and A=8 systems which immediately fall apart instead of β^+-decaying. To get to carbon, specifically ^{12}C that makes up 99% of the carbon in the universe, the triple-alpha process is needed. After a star has a large enough concentration of ^{4}He nuclei, the star will start the triple-alpha process, as seen in Fig. 1.9(b). Further discussion on the triple-alpha process and the Hoyle state can be found in Section 3.1.

The next process of Nucleosynthesis that occurs in stellar burning is the slow neutron-capture process, or s-process. In the core of thermally pulsing asymptotic giant branch stars, two key reactions,

1. $^{13}\mathrm{C} + {}^4\mathrm{He} \rightarrow {}^{16}\mathrm{O} + n$ and

2. $^{22}\mathrm{Ne} + {}^{4}\mathrm{He} \rightarrow {}^{25}\mathrm{Mg} + n$,

produce a weak neutron flux which fuels the s-process [37]. These neutrons capture on other seed nuclei in the star, resulting in an isotope with one higher atomic mass. This can create unstable nuclei with β^--decay lifetimes smaller than the time it would take for another neutron capture to occur. This process slowly steps up stable nuclei, like in Fig. 1.10 showing a section of the chart of nuclides, producing heavy elements all the way up to lead.

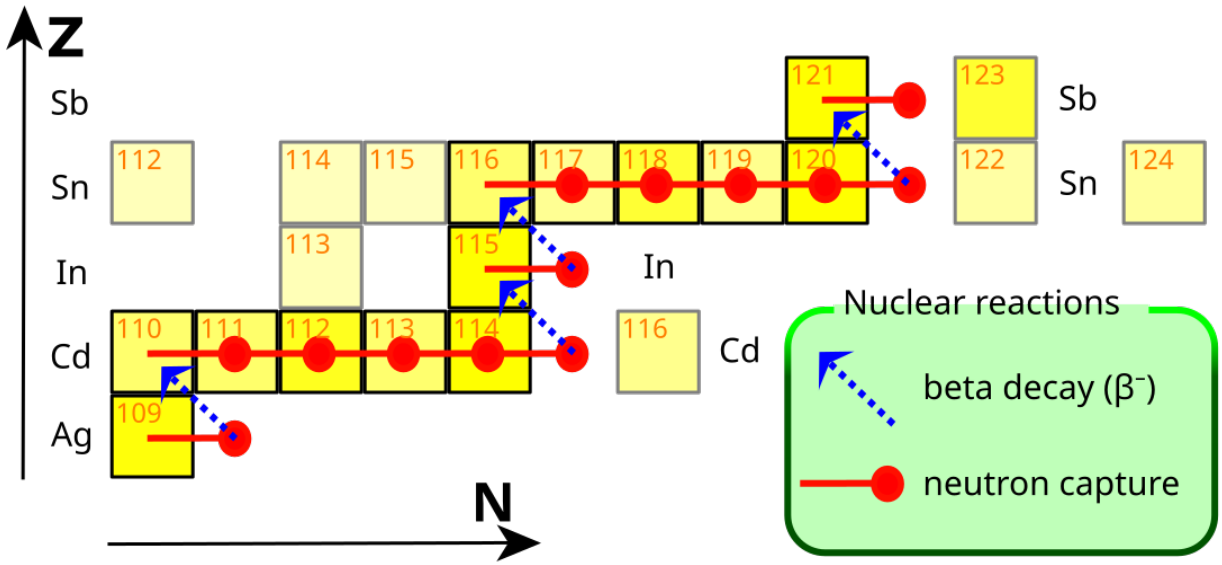

Fig. 1.10: Illustration of the path s-process neutron capture takes, ranging from Ag to Sb. The yellowness of the isotope block represents relative abundance on the earth [38]. Not every isotope observed can be produced in the s-process.

The s-process is insufficient to explain the abundances of many observed isotopes. Examples of this are the neutron-rich ^{136}Xe which is observed at 8.9% abundance or the neutron-poor ^{124}Xe observed at 0.1% abundance. The ^{112,114,115}Sn and ^{122,124}Sn isotopes shown in Fig. 1.10 also are not a result of s-process nucleosynthesis. To understand the observed abundances, we must also look to violent astrophysical events such as Type-II supernovae and neutron star mergers. A Type-II supernova is the explosion at the end of a massive star's

life. The core of this old star quickly burns through fuel as heavier and heavier elements are formed, resulting in a collapse of the core. As the outer shell also collapses inwards, it rebounds off the dense core, exploding and spewing matter outwards. The core can sometimes result in a dense, neutron-rich star called a neutron star, which is another site of interest. Neutron stars can accrete matter onto their surface which is a site of nucleosynthesis but they also can merge with other neutron stars. The merging process again results in spewing matter outwards.

These violent events are thought to be the location of the rapid neutron-capture process, or r-process. In such events, an extremely dense neutron flux is created leading to rapid neutron capture out to isotopes with short β-decay half-lives. This process pushes out to the extremely neutron-rich isotopes on the chart of nuclides which afterwards decay back to stability. The r-process helps explain the abundances of heavier nuclei and neutron-rich isotopes like ^{136}Xe mentioned above. Observationally, a single neutron-star-neutron-star merger has been observed, and the presence of nucleosynthesis was confirmed in that event [39].

A similar process called the rapid proton-capture process, or rp-process, can occur at the surface of neutron stars as their gravitational well accretes matter from a companion star onto the neutron star surface [40]. The matter is accelerated towards the surface such that reactions occur and a large flux of protons is created. This flux of protons fills out the neutron-poor side of the chart of nuclides, helping to explain the small abundances of light proton-rich isotopes. These are observed from earth as X-ray bursts with data from this dissertation in Chapters 4 and 5 being useful in calculating their light curves.

The goal of studying nucleosynthesis is to better understand the origin of matter and predict the natural abundances of elements and their isotopes. One part we don't currently understand is the relative significance of supernovae versus neutron-star mergers as sites

for r-process [41]. To answer the question where nucleosynthesis occurs, large scale nuclear reaction simulations have been performed that take into account a massive amount of nuclear data and make predictions for observables such as the natural abundances [42]. Through the study of nuclear properties, such as resonances and reactions, nuclear data can be used to improve the simulations of stellar environments, resulting in more accurate models of nucleosynthesis.

Chapter 2

Experimental Methods

This chapter presents the experimental techniques, setups, and detectors employed for the measurements in this dissertation. First, invariant-mass spectroscopy is discussed as it is the technique used to measure short-lived particle-unbound states and connects all of the main work on proton emission. Next, two different experimental setups, the Gobbi array and the NSCL setup, are described. Finally, the main types of detectors used are broken down and explained in greater detail including the theory behind how they work.

2.1 Invariant-mass spectroscopy

Invariant mass is the mass independent of the overall motion of the system or the collection of objects that define the parent system. The definition for the invariant mass, M (in energy units), is an extension of the energy-momentum relation for a group of particles given by,

$$\left(Mc^2\right)^2 = \left(\sum_i E_i\right)^2 - \left(\sum_i \overrightarrow{p_i} c\right)^2, \tag{2.1}$$

where E_i and $\overrightarrow{p_i}$ are the total energy and momentum of each fragment and c is the speed of light. The usefulness of this definition comes from that fact this quantity is invariant for

a system in all frames of reference, meaning if you can measure the state for a system of particles in the laboratory frame, the invariant mass is the same for the center-of-mass frame (or any other frame of interest).

For a particle-decaying state, invariant-mass spectroscopy (IMS) is a method that measures the final state energy and momentum of all the decay-products. When working at a radioactive beam facility, this works well for states with short lifetimes, <1 ps, so the state decays in the target and the outgoing parent has a decay vertex to reconstruct back to. For a one-proton decay, Eq. (2.1) is particularised to be,

$$(m_{residue}c^2 + m_p c^2 + E_T)^2 = m_{residue}^2 c^4 + m_p^2 c^4 + 2\left(E_{residue}E_p - |\boldsymbol{p}_{residue}c|\,|\boldsymbol{p}_p c|\,cos(\theta)\right), \quad (2.2)$$

where the decay residue and proton each have a known mass, $m_{p/residue}$, a measured energy, $E_{p/residue}$, and a measured momentum vector, $\boldsymbol{p}_{p/residue}$. The decay energy, E_T, is the energy released in the decay that is put into kinetic energy separating the particles. The decay energy E_T is related to the Q-value and excitation energy of the parent, E^*, as $E_T = E^* - Q$. Finally, θ is the lab angle between the residue and proton. In practice, the position of the residue and proton are measured by the detectors and the angle between them comes from assuming the vertex of the decay is at the center of the target.

IMS is in essence a relative mass measuring technique, requiring as a reference, the masses of the decay products. To measure the particle type, which is required to know the mass and momentum, the standard ΔE-E technique is used. A detector-telescope, comprised of a stack of detectors, gives both a measured ΔE as the particle passes through a thin detector and a total kinetic energy E as the particle deposits the remaining energy in the following thicker detector. This method relies on the fact that charged particles deposit energy in absorbing materials at a rate with respect to the path length, x, according to the

Bethe-Block formula, which to leading order is

$$\frac{dE}{dx} \propto \frac{Z^2 A}{E}. \tag{2.3}$$

The rate of energy loss is thus roughly proportional to the square of the charge of the traversing ion, which is equal to its atomic number Z if fully stripped (giving element separation), and proportional to its mass number A (giving isotopic separation). When plotted, ΔE-E produces bands for each particle type detected as shown in Fig. 2.1.

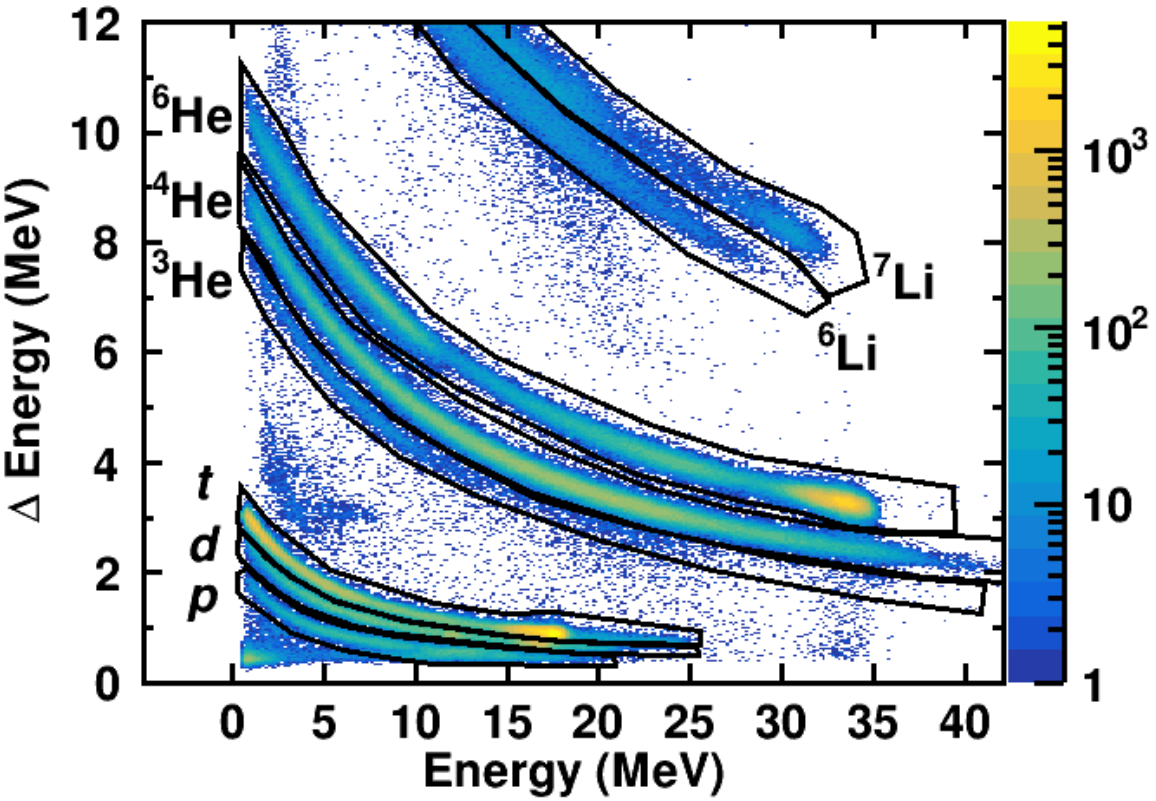

Fig. 2.1: ΔE-E from the Gobbi array with gates showing particle identification for the light charged particles. The ΔE signal is from the thinner transmission detector and the E signal from the downstream stopping detector.

2.2 Exerimental setups

Two different experimental setups were employed for the work presented in this dissertation. Chapter 3 uses the setup in Section 2.2.1 while Chapters 4 and 6 use the setup in Section 2.2.2.

2.2.1 "Gobbi" array

The first experiment, performed at the Texas A&M University Cyclotron institute, detected charged particles using an array of four ΔE-E [Si-Si] telescopes arranged around a square central beam hole, see Fig. 2.2, and locally nicknamed the "Gobbi" array. [1] This setup was previously designed and used to study the $2p$+2α decay of ^{10}C [43] but was used here for detecting the p+^{6}He decay of ^{7}Li at low energies. Each quadrant had two layers of the Micron Semiconductor BB7 design [44] Si previously employed by the HIRA array [45]: a 65-μm-thick ΔE single-sided Si detector with 32 strips, backed by a 1.5-mm-thick Si double-sided E detector with 32×32 strips. Both layers were 64 × 64 mm in area with the quadrants arranged with an offset from the center to produce a 1.6-cm-square hole for the unreacted beam to pass through. A circular beam blocker with $\varnothing_{inner}$=1.6 cm and $\varnothing_{outer}$=3.8 cm was used to protect the inner portions of the Si detectors from the high rate of elastic scattering. The detector array was located 23.5 cm downstream from the the target, a distance that optimized the detection of decay fragments with a low decay energy or little relative energy between them. The angular range spanned lab angles from θ=5° to 20°. Readout of the Si-strip information was performed with HINP16C chips [46], requiring a coincidence between a ΔE and E detector to record data.

[1] This array name was chosen by my advisors to recognize a senior GSI scientist who started to use this geometery effectively in the 1970's (and is not a reference to the Gobi desert).

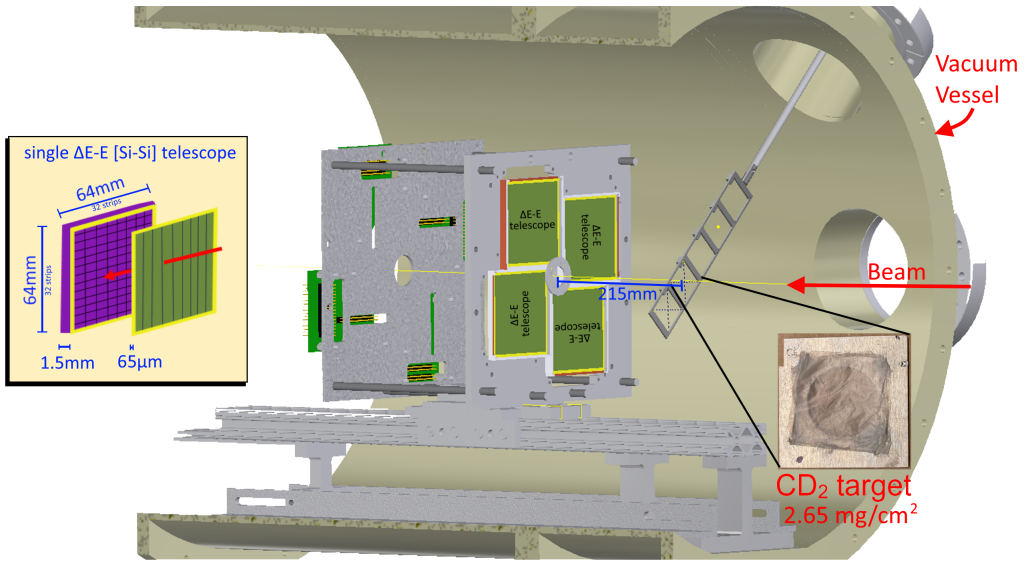

Fig. 2.2: CAD drawing of the Gobbi array in the experimental setup with the beam direction from right to left. Included on the left is an expanded view of a telescope and on the right is a picture of the target. The entire detector setup was housed in a high-vacuum chamber coupled to the accelerator.

2.2.2 NSCL setup

The second experiment, performed at the National Superconducting Cyclotron Laboratory (NSCL), was set up to be sensitive to both γ- and proton-decay branches using the combination of detectors diagrammed in Fig. 2.3. The photon detector was the CAESium-iodide scintillator ARray (CAESAR) [47] which was centered around the Be target. CAESAR was arranged in 8 rings with a total of 163 working scintillators spanning 55° to 163°. The two most upstream rings, labeled A and B, consisted of 3"x3"x3" CsI(Na) crystals while the other six rings, labeled C-H, were 2"x2"x4" crystals. Protons were detected using a $\Delta E - E$ [Si-CsI(Tl)] telescope ring array covering from 1° to 9°. This array consisted of a 1-mm-thick S4 annular double-sided silicon strip detector (DSSD), manufactured by Micron Semiconductor [44], backed by an annular array of CsI(Tl) detectors. The S4, as used, was wired into 128

concentric annular rings and 128 pie-shaped wedged sectors. The CsI(Tl) crystals, were arranged directly behind the S4 detector in two concentric rings of 4 (inner) and 16 (outer) crystals.

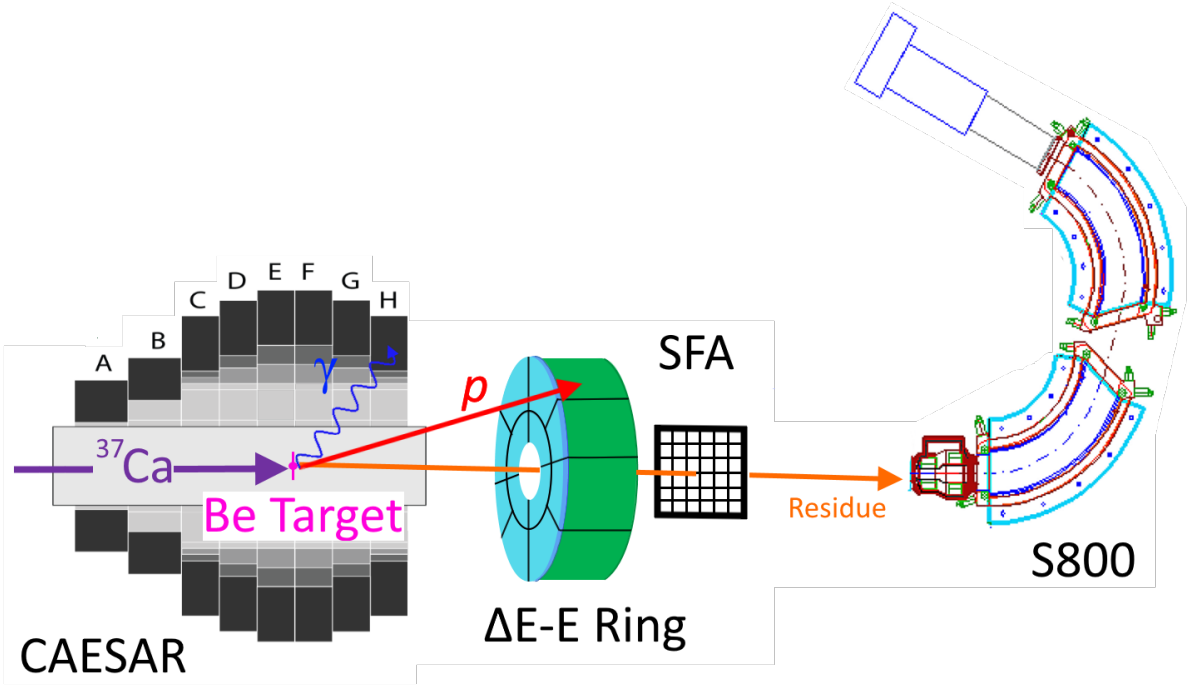

Fig. 2.3: Schematic of the experimental apparatus in the NSCL setup. The beam direction is from left to right. CAESAR was used to measure the γ rays, the $\Delta E - E$ [Si-CsI(Tl)] telescope ring array measured light charged particles (such as protons), the SFA and S800 spectrograph measured the heavy residue.

The heavy residue passed through the center of the ring array, hitting the scintillating-fiber array (SFA) made of an orthogonal pair of scintillating fiber ribbons. Each ribbon consists of 64 fibers of square (250 μm x 250 μm) cross section. This array records precise angular information for the heavy residue, increasing the decay-energy resolution. After passing through the SFA, the residues then entered the S800 spectrograph where the particle

type and momentum were identified. Two magnetic rigidity settings were used, one tuned for the best acceptance of ^{36}Ca while blocking some ^{37}Ca beam particles ($B\rho = 1.9696$ Tm) and the second tuned for the best acceptance of ^{35}K ($B\rho = 2.0468$ Tm).

2.3 Silicon detectors

Semiconductor crystals, notably Si and Ge, make useful detectors. Most electrons in the crystal, are bound to specific lattice sites, while excited electrons are free to migrate from site to site. The band of electronic states that are the least-bound is called the valence band and the lowest-energy delocalized states form a band called the conduction band. The energy difference between these bands is the band gap. Insulators have a very large band gap, requiring a large amount of energy to excite an electron into the conduction band. Metals have a overlapping valence and conduction band, meaning ground state electrons are free to jump from site to site, making them excellent conductors. Silicon as a semi-conductor, has a band gap larger than $k_B T$ (Boltzmann's constant $\times$ temperature) but small enough to make particle-hole excitations easy. When charged particles move through a crystalline material, they deposit energy per unit length in proportion to their stopping power, Eq. (2.3), creating electron-hole pairs in proportion to the energy they deposit. For silicon, it takes an average of about 3.6 eV, at 300 K, to generate one electron-hole pair, meaning a charged particle at 3.6 MeV would create around one million excitations [48].

Pure silicon crystals are typically doped with different elements and sandwiched together to form a p-n diode junction. P-doped silicon is created when an electron acceptor is added to the lattice using elements from group III of the periodic table and n-doped silicon is created when an electron donator is added to the lattice using elements from group V. In a p-n junction where the two types are combined, the n-doped donates electrons to the p-doped,

forming a region that is neutral and charge depleted. When reversed biased, i.e. applying a negative charge to the p-doped side and a positive charge to the n-doped side, the charge depleted region grows. This depleted region becomes the active volume of the detector where electron-hole pairs form and, subjected to the reverse bias, the charge carriers drift to the contacts, creating a signal that can be read out by electronics. In a practical device, all but the very thin surface regions are depleted and therefore part of the active detector volume.

The DSSD are named so because they have surface contacts on both sides separated by thin inactive SiO_2 regions. The strips can be read out individually and are used in both setups to provide position information for the charge deposited as a front and back strip overlap in only one Cartesian position. For the BB7 design Si used in Gobbi, the strips form an x-y grid to give a position within a 2×2 mm Cartesian pixel. For the S4 design used in the NSCL setup, the front is divided into pie-shaped sectors and the back is divided into concentric rings, essentially providing the polar coordinates of the impinging particle.

2.3.1 Calibration

The silicon detectors were calibrated with a ^{226}Ra alpha source using the five main peaks found in Table 2.1 which lists the decay chain. A high-energy calibration point was also included in the fit and was obtained using elastic scattering of ^{7}Li on a Au target at 38.6 MeV. The result of the calibration for one front strip of the 1.5 mm thick silicon used in Section 2.2.1 is shown in Fig. 2.4.

Tab. 2.1: Decay chain of the ^{226}Ra with decay branches above 1% included. The five highest intensity alpha decays were used in calibrating the silicon strip detectors. ^{226}Ra is isolated from uranium samples and is the great grand daughter of ^{233}U.

Parent	$t_{1/2}$	decays	E_α (MeV)	Int.
^{226}Ra	1600 yr	α	4.784	94%
			4.601	6%
^{222}Rn	3.82 d	α	5.489	100%
^{218}Po	3.10 m	α	6.002	99.98%
^{214}Pb	27.1 m	β-	-	-
^{214}Bi	19.7 m	β-	-	-
^{214}Po	163 μs	α	7.687	99.98%
^{210}Pb	22.2 yr	β-	-	-
^{210}Bi	5.01 d	β-	-	-
^{210}Po	138.4 d	α	5.304	100%
^{206}Pb	stable	-	-	-

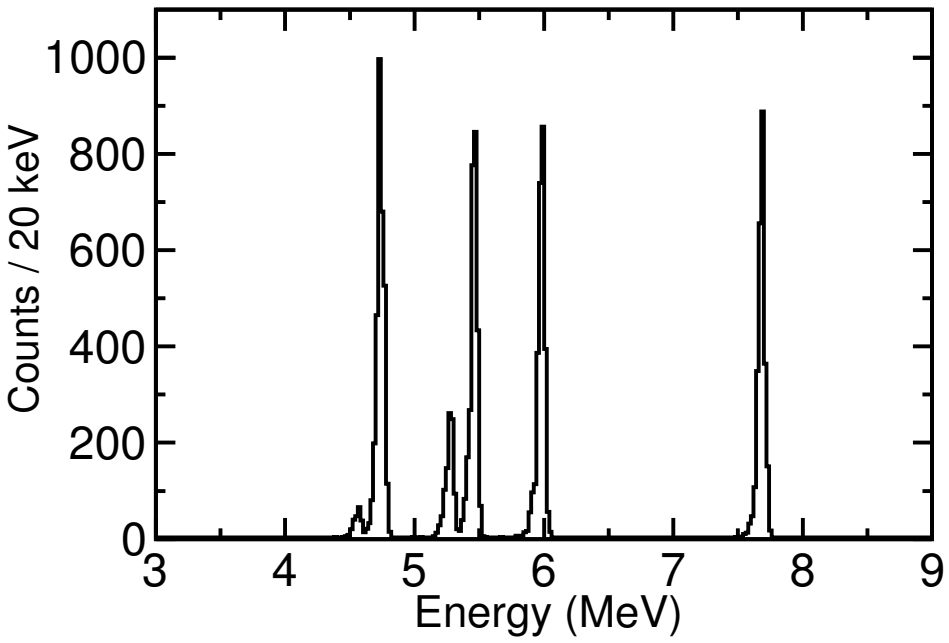

Fig. 2.4: Typical 5-peak energy spectrum for a calibrated front strip of a Si detector. The peaks seen here are the decays listed in Table 2.1.

2.4 Scintillators

2.4.1 CsI(Tl)

In the NSCL setup, the CsI(Tl) detectors sit directly behind the S4 detector in two concentric rings of 4 (inner) and 16 (outer) crystals. These are the 50-mm-thick stopping detectors for the light charged particles such as protons that have been emitted. Each detector is comprised of an inorganic crystal of CsI that has been doped with Tl at the part per thousand level with a photodiode attached to the back. These inorganic scintillators are modestly priced and it is possible to grow them in large volumes. Similar to semiconductors, particle hole excitations are formed when energy is deposited in the material, exiting the electron into the conduction band of the crystal. Here however, the crystals are insulators with band gaps exceeding the visible part of the electromagnetic spectrum. Excited electrons moves freely within the crystal until they are trapped by impurities such as the Tl dopant. The dopant introduces levels within the band gap and the deexcitation proceeds via the emission of a visible photon. The photons are collected in the photodiode and the amount of light detected is roughly proportional to the energy of the radiation.[2]

The CsI(Tl) detectors were calibrated using a 76 MeV/u proton beam with a 0.5% $\Delta p/p$ acceptance which was degraded with two different absorbers, a 1-mm-thick Be and a 9.65-mm-thick Al absorber. After passing through the absorber, a 3.175 mm Al plate in front of the telescope, and the 1.5 mm Si, the proton beam produced calibration points at 66.3 MeV and 44.9 MeV for the CsI(Tl). The small angles for the inner ring $\theta = 2.75^\circ$ and outer ring $\theta = 5.49^\circ$ as well as the slight deviation in angle across a CsI(Tl) due to light collection were corrected for in the calibration procedure.

[2] It is the lack of proportionality that allows some crystals to have the ability to identify particles. This capability, called pulse-shape discrimination or PSD, is not used in this work.

2.4.2 CAESAR

The CAESAR array was used for gamma-ray detection in the NSCL setup, using a slightly different inorganic scintillator CsI(Na). The CsI(Na) crystals are similar to CsI(Tl) except the crystal dopant is switched to Na, resulting in about twice the light output. This also results in the crystal being very hygroscopic, requiring the crystal to be hermetically sealed in a can.[3] The extra material isn't an issue for CAESAR, as it is designed for detecting gamma rays, which interact differently than charged particles.

The intensity, I, of gamma rays in a material drops exponential through a material according to,

$$I(x) = I_0\, exp(-\mu x), \tag{2.4}$$

where μ is the linear absorption coefficient specific to the material and x is the distance traversed through the material. The Al can containing the CsI(Na) crystals only slightly reduced the total efficiency as most photons pass through this low Z material without interacting. A photon interacts with the detector or medium in three main ways:

1. Through the photoelectric effect, the photon transfers all of its energy to an electron and produces a single "photopeak" in the spectrum.

2. Through Compton scattering, the photon scatters off an electron transferring only a fraction of the initial photon energy (dependent on the scattering angle), creating a continuum below the photopeak in the spectrum. The spectrum of deposited energy always corresponds to the energy transferred to electrons.

3. Through pair production, if the photon has sufficient energy, it interacts with another body, either a nucleus or an electron, and an electron-positron pair is simultaneously

[3] For the CsI(Tl), the crystal is only slightly hygroscopic, requiring no material to seal the crystal which would degrade the energy of the charged particles.

created. In this case the initial photon energy is transformed into the rest mass of the e^+ and e^- and the kinetic energies of these particles. Typically, the positron finds an electron and annihilates, releasing two photons which can escape the detector volume. This results in absorbed energy peaks, one and two electron rest-mass equivalents less than the energy of the initial photon, called escape peaks.

Combined, these three processes lead to spectroscopy features in gamma-ray spectra schematically diagrammed in Fig. 2.5.

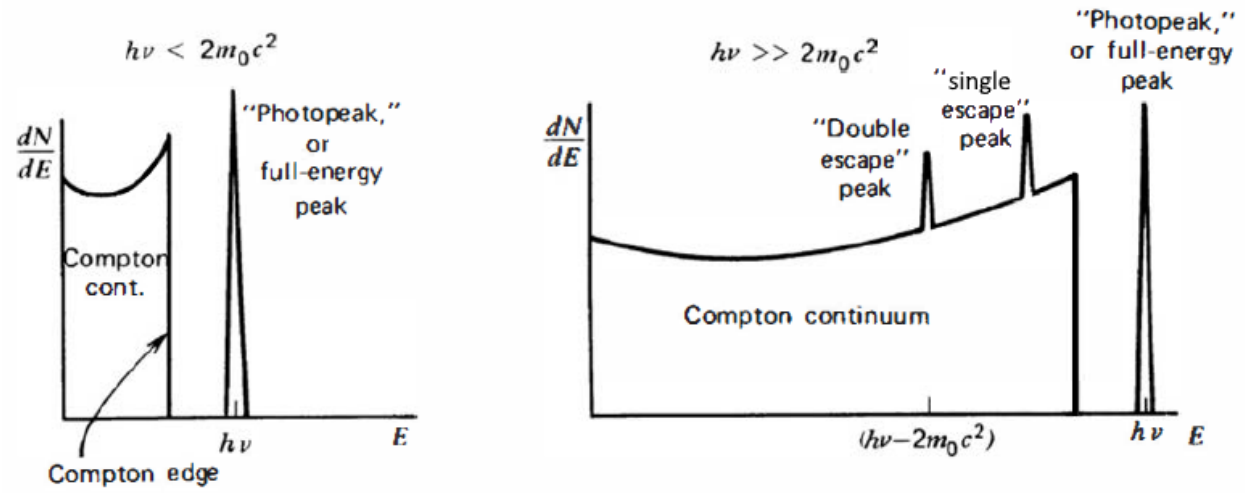

Fig. 2.5: (left) Schematic of the detector response to gamma rays with an energy less than 1022 keV and (right) to an energy much greater than 1022 keV. Adapted from Ref. [48].

CAESAR has a full-energy-peak efficiency for a 3-MeV γ ray of $\sim$ 15%. This rather high efficiency comes with the trade off of only modest energy resolution, $\sim$ 8% FWHM at this energy. Every crystal in CAESAR was energy calibrated using several standard γ-ray sources with the energies given in Table 2.2.

For gamma decays from excited nuclei in-flight, the energy of the observed gamma is Doppler shifted relative to the energy emitted in the rest frame. A γ-ray emitted forward

Tab. 2.2: Gamma-ray sources used to calibrate CAESAR. γ-rays from the AmBe source are the result of ^{9}Be(α,γ)^{12}C reactions which populates the first excited 2^{+} state in ^{12}C at 4440 keV.

Source	$t_{1/2}$	E_γ (keV)	Int.
^{60}Co	5.27 yr	1332.5	100%
		1173	99.9%
^{88}Y	106.6 d	1836	99.2%
		898	93.7%
^{137}Cs	30.08 yr	662	85.1%
Am-Be	432.6 yr	4440	85.1%

relative to the emitter's velocity is blue shifted towards higher energies while a γ-ray emitted backward is red shifted towards lower energies. In the NSCL setup, the radioactive ion beam used was about $1/3^{rd}$ of the speed of light ($\beta = v/c = 0.33$) or $v \approx$10 cm/ns. For a γ-ray observed with lab energy E_{lab}, originating from a parent nucleus with a relativistic velocity, the Doppler shift can be largely accounted for using the first-order relation,

$$E_{rest} = E_{lab}\frac{1 - \beta\, cos(\theta)}{\sqrt{1-\beta^2}}, \tag{2.5}$$

where θ is the observed lab angle with respect to the beam direction.[4] The gamma-decay spectrum for CAESAR is reconstructed using angles from the target to the center of the crystal hit. This assumes a short lifetime, which is a good assumption the for low multipolarity transitions and high energies studied in Chapter 4.

[4] This expression does not account for the finite solid angle of the detector.

2.4.3 Fibers

The SFA is comprised of two fiber ribbons each with 64 plastic scintillating fibers with square cross section. As the heavy residue passes through the SFA, a fiber from each ribbon lights up, giving an x-y position with 250 μm accuracy. Each strand of the fiber ribbon was coupled to a Hamamatsu H8500C multianode photomultiplier tube (PMT), where all 64 pins were connected through a resistive network, similar to that seen in the discretized positioning circuit of [49]. Each of the four corners, labeled A, B, C, and D, were read out with a charge to digital converter (QDC). The voltage readouts were combined in analysis to give a position on the face of the PMT as,

$$X_{pos} = \frac{(V_A + V_B) - (V_C + V_D)}{V_A + V_B + V_C + V_D} \tag{2.6}$$

and,

$$Y_{pos} = \frac{(V_A + V_C) - (V_B + V_D)}{V_A + V_B + V_C + V_D}. \tag{2.7}$$

Events for the vertical strand of fibers PMT are shown in Fig. 2.6 with the grid showing the gates used to determine fiber number. The fiber number starts in the bottom left corner for y = -7.875 mm and follows a boustrian pattern, snaking back and forth as you move up rows. The second row from the bottom starts on the right side and the third row starts back on the left side, ending at the top left corner for y = +7.875 mm.

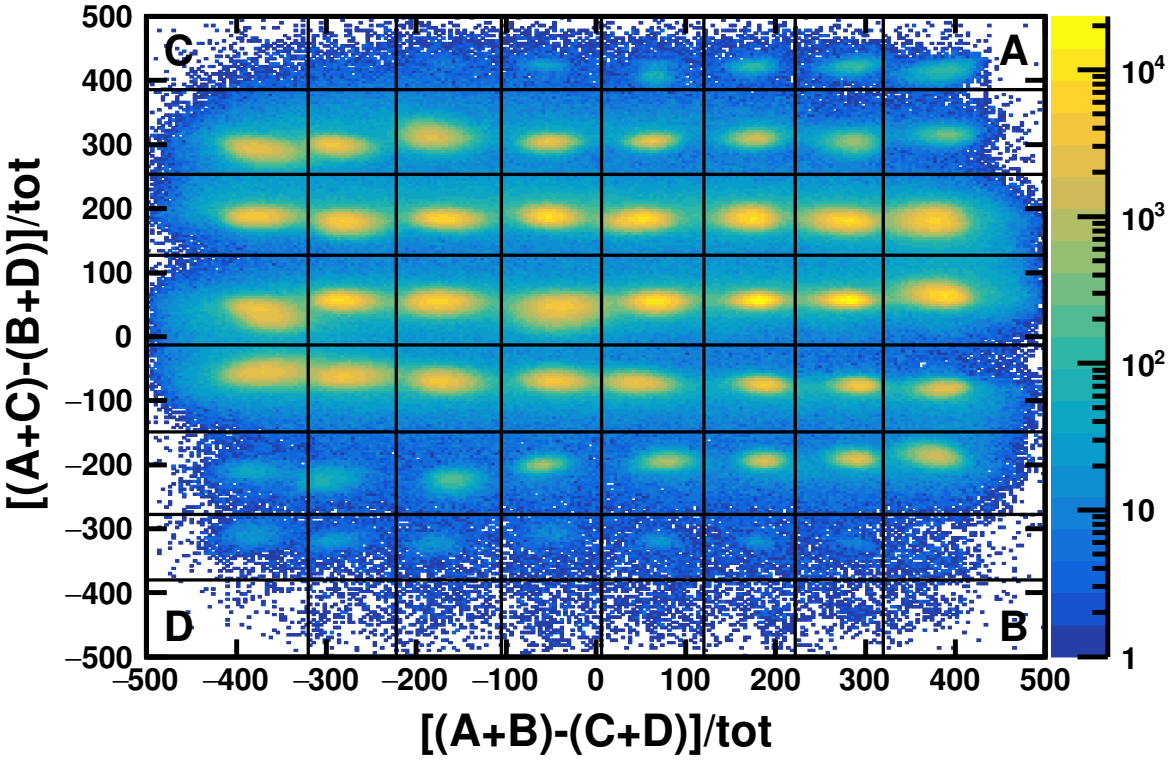

Fig. 2.6: Plot showing gates applied to the vertical ribbon of the SFA to assign the y-value of the heavy residue. The axis labels give the voltage algebra required to determine position.

2.5 Magnetics

The S800 is a superconducting spectrograph designed to measure the momentum and scattering angle of reaction products to high precision [50]. The S800 is comprised of two parts diagrammed in Fig. 2.7(a), the analysis line before the target and the spectrograph after the target. The analysis line starts after the A1900 spanning from the object position to the target with a total length of 22 m. The time-of-flight (ToF) between a fast plastic scintillator at the A1900 focal plane relative to the S800 focal plane and the ToF between a fast plastic scintillator at the S800 object plane relative to the S800 focal plane provides the beam

identification used to discriminate between different projectiles. The gates used for different projectiles in the beam are shown in Fig. 2.8.

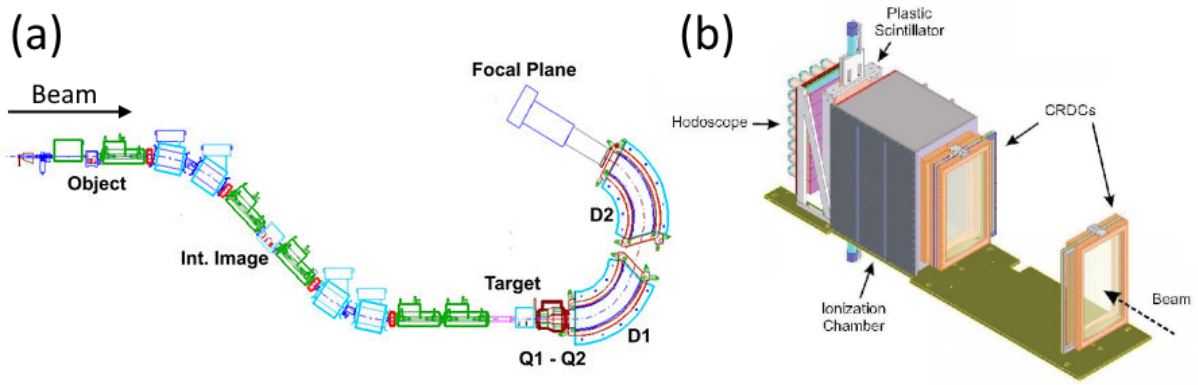

Fig. 2.7: (a) Engineering drawing of the S800 spectrograph with labeled stations and (b) detectors in focal plane at the end of the S800. [51]

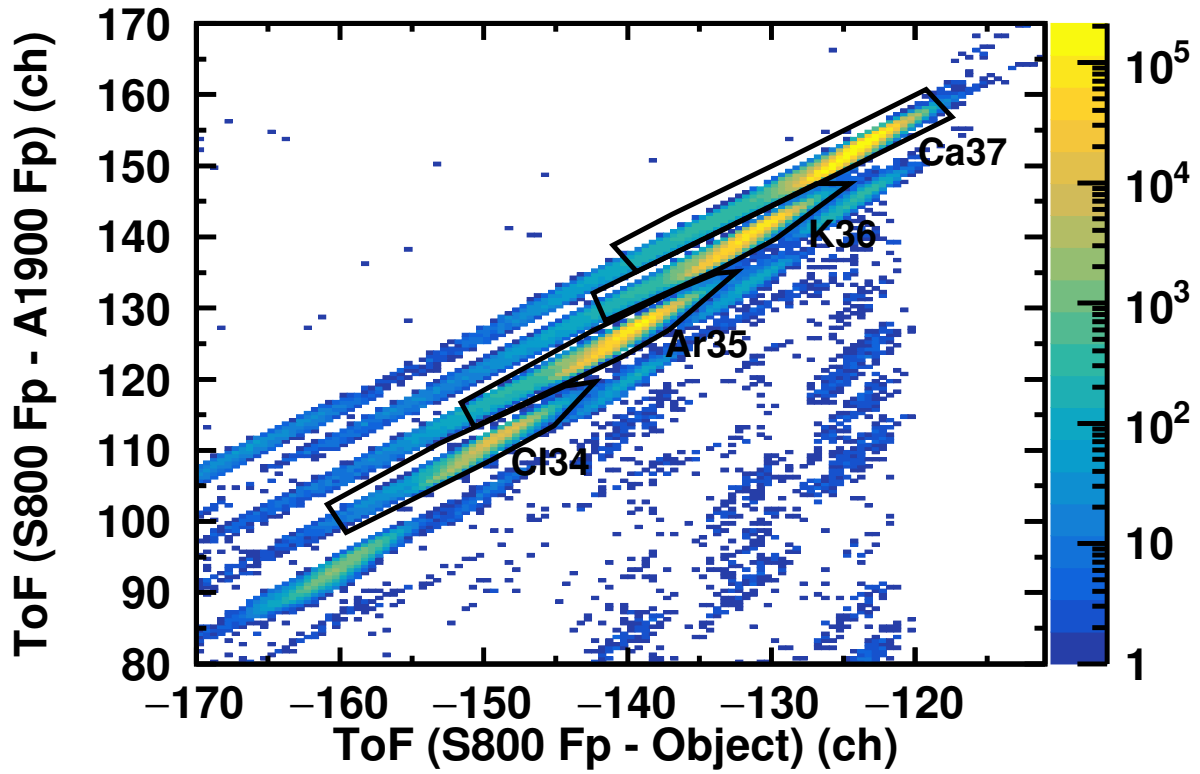

Fig. 2.8: The ToF between the S800 focal plane (Fp) and A1900 Fp versus the ToF between the S800 Fp and S800 object plane gives the projectile type in the secondary beam.

The spectrograph section starts with two quadrupole and a sextupole magnet used to focus the transmitted particles and correct for aberrations. The two massive superconducting dipoles bend the charged particles, separating them in the dispersive plane by their magnetic rigidity before they reach the focal plane of the spectrograph. At the focal plane, there is a collection of detectors, shown in Fig. 2.7, including two cathode-readout drift chambers (CRDC), an ionization chamber, and a plastic scintillator [52].[5] The CRDCs are used to track the trajectory of the transmitted particle, giving the momentum when the particle type is known with the help of an inverse map. To get the particle type, the ionization chamber and plastic scintillator are required. The ionization chamber is comprised of 16 independent

[5] This work does not use the hodoscope indicated in Fig. 2.7.

gas-filled parallel-plate chambers. This device separates out different charges based on the energy loss using Eq. (2.3). The focal plane plastic scintillator provides a time giving the ToF between the object location, in the analysis line (see Fig. 2.7(a)), and the spectrometer focal plane (see Fig. 2.7(b)). This information separates particles based on their mass if their momentum is known. Plots of the energy lost in the ion chamber vs the ToF are given in Figs. 2.9 and 2.10 for the two different magnetic rigidity settings used.

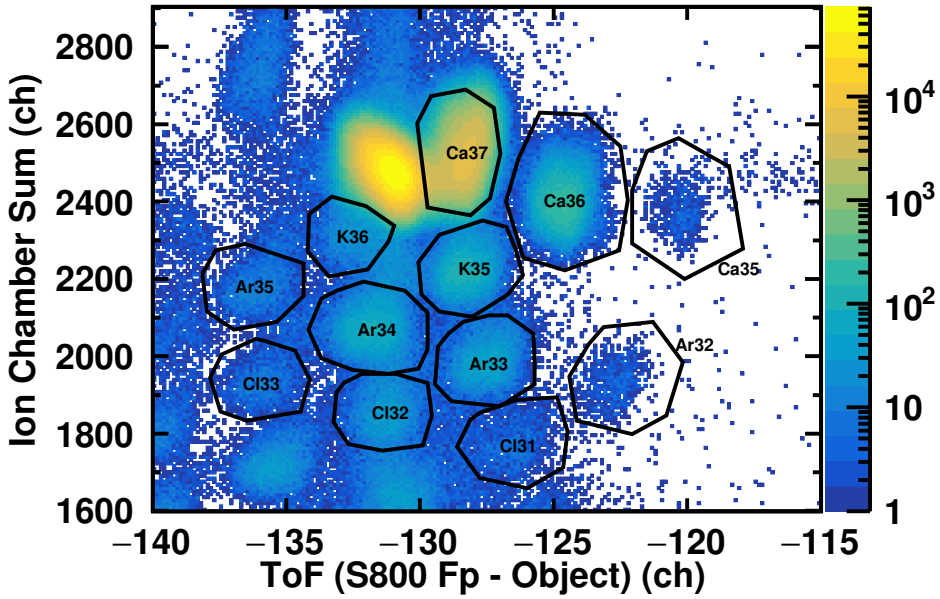

Fig. 2.9: Particle identification plot from the S800 with $B\rho = 1.9696$ Tm, tuned for the best ^{36}Ca acceptance. The extra (unlabled) lobe to the left of ^{37}Ca was likely due to the presence of a beam blocking slit.

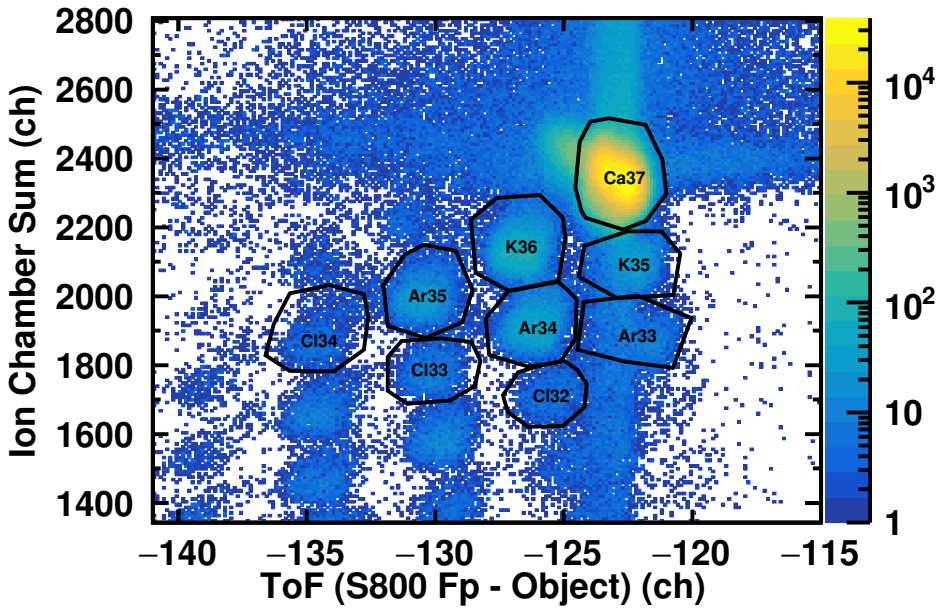

Fig. 2.10: Particle identification plot from the S800 with $B\rho = 2.0468$ Tm, tuned for the best ^{35}K acceptance.

Chapter 3

Null Result for a Near-threshold s-wave Resonance in ^{7}Li

Light nuclei are an important testing ground for nuclear *ab initio* calculations as their properties can be calculated with few approximations. In this chapter, we will examine a prediction from the No Core Shell Model with Continuum (NCSMC) which recently predicted an s-wave resonance just above the proton-decay threshold of ^{7}Li at an excitation energy of 10.2 MeV [53]. This prediction motivated a search for the resonance as a test of the calculation's predictive capabilities for states in the continuum. This case was also the perfect case for IMS as the resonance was above three open decay channels where two could be observed with charged-particle detectors.

3.1 Near-threshold resonances

A near-threshold resonance is an excited state or resonance of the nucleus that is close in energy to a particle-decay threshold. Many-nucleon correlations in this quasi-bound system result in the formation of clusters via narrow resonances that match the structure of the decay threshold. The properties of near-threshold resonances can be dominated by the clustering of

nucleons composite subsystems. These resonances play an important role in nucleosynthesis such as the triple-alpha process or the ^{13}C(α,n)^{16}O reaction.

A famous example of a near-threshold state is the Hoyle state in ^{12}C. As discussed earlier in Section 1.5, the triple-alpha process in stellar nucleosynthesis fuses three ^{4}He nuclei together to create ^{12}C, skipping the particle-unstable A=5 or A=8 systems. In the 1950s, Fred Hoyle identified that the observed elemental abundances of Carbon cannot be explained with the direct capture or resonant capture of three ^{4}He nuclei through the states known at the time [54]. He predicted the presence of an unobserved state just above the threshold energy of $\alpha + \alpha + \alpha$, such that the fusion rate is increased through resonant capture to the excited state. This prediction lead to finding the near-threshold 0_2^+ state of ^{12}C just 285 keV above the α+^{8}Be threshold and 378 keV above the $\alpha + \alpha + \alpha$ threshold [55], see Fig. 3.1. In *ab initio* calculations, both the structure of $^{8}\text{Be}_{g.s.}$ and $^{12}\text{C}(0_2^+)$ can be accurately described by α clustering [56, 57].

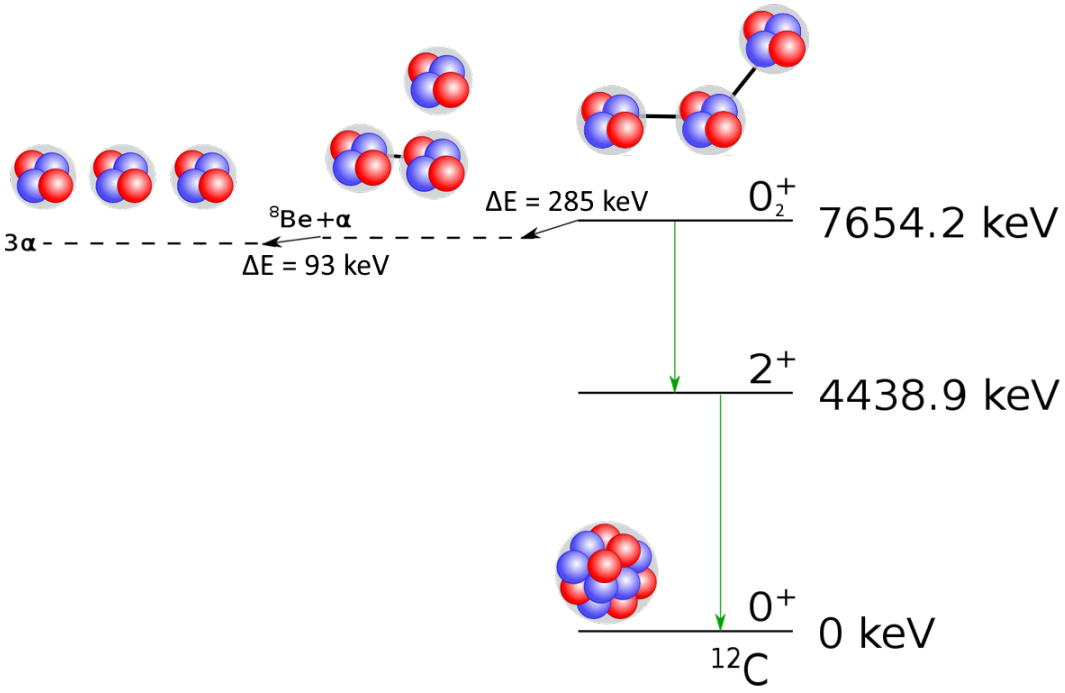

Fig. 3.1: Level diagram of ^{12}C including the level thresholds for $\alpha + \alpha + \alpha$ and α+^{8}Be. In the triple-alpha process, $\alpha + \alpha + \alpha$ resonant capture is enhanced through the 0_2^+ state, having a small chance to de-excite through gamma decays down to ground state ^{12}C.

A second example of an important near-threshold resonance occurs in ^{17}O at the α+^{13}C particle-decay threshold. Stars that are hot enough to utilize the CNO fusion cycle and that have been seeded with ^{12}C from previous stars, have some ^{13}C, enabling the ^{13}C(α,n)^{16}O reaction. This is one of the two major reactions that produce a neutron flux in stars which fuels the s-process. The properties of the wide $1/2^+$ resonance just below the threshold at 6.36 MeV relative to the ^{17}O ground state, dictate the ^{13}C(α,n)^{16}O reaction rate within the Gamow window [58]. The Gamow window represents the sweet spot where stellar fusion is most likely to occur, resulting from the overlap between the kinetic energy distribution in stars, which is a Maxwellian distribution, and the Coulomb barrier tunneling probability,

which exponentially grows as the kinetic energy of the interacting particles increases. The astrophysical S-factor, a quantity which takes the exponential tunneling probability into account, for the α+^{13}C reaction is plotted in Fig. 3.2(a) with the Gamow window highlighted in blue exactly where the s-factor depends most on structure of the $1/2^+$ state in ^{17}O.

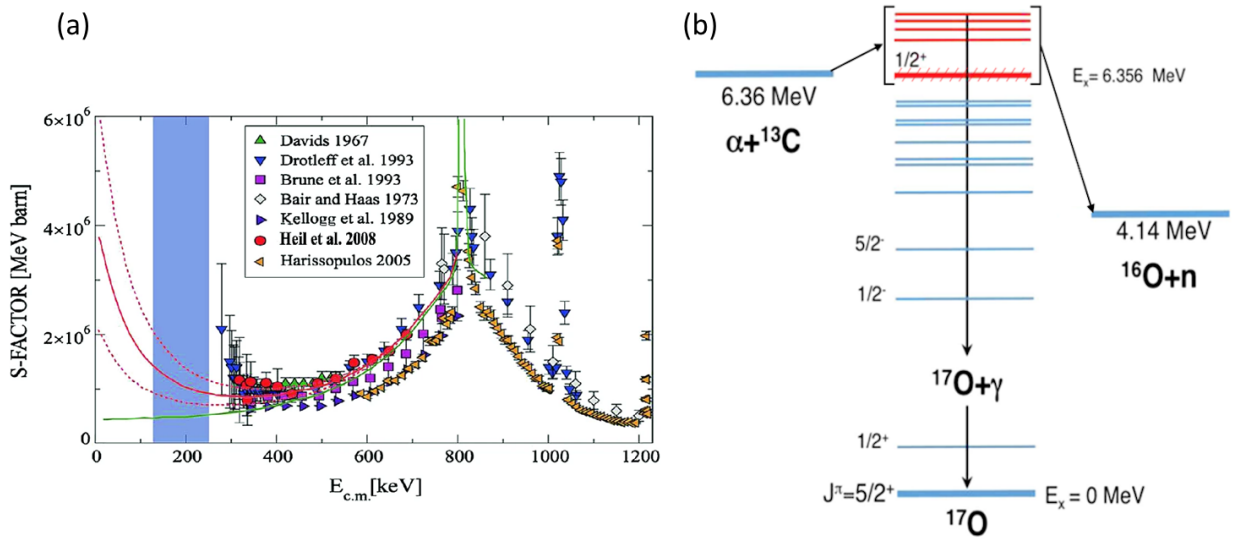

Fig. 3.2: (a) Data from various experiments measuring the astrophysical S-factor of α+^{13}C with the Gamow window highlighted in blue. The solid red curve (with dotted-line error bars) shows an extrapolation including the near-threshold resonance. The green curve shows an extrapolation with no near-threshold resonance [59]. (b) Level diagram of ^{17}O showing the compound-nucleus intermediate states for the ^{13}C(α,n)^{16}O reaction.

What is the origin of these near-threshold resonances? For the states mentioned in ^{12}C and ^{17}O, an anthropic argument can be offered to rationalize their existence [60]. If they didn't exist or their properties were different, we might not be here to observe them. If one wishes to know about the true quantum-mechanical origin of a state, one must turn to a first-principle or *ab initio* calculation. *Ab initio* methods are important in calculating properties of light nuclei as they retain the the complexity arising from many-nucleon correlations

and currents. The No Core Shell Model and its extension the No Core Shell Model with Continuum (NCSMC) [61] belongs to this class of methods which are detailed in the next section.

3.2 No Core Shell Model with Continuum

The No Core Shell Model (NCSM) [62] belongs to a class of nuclear theory calculations called *ab initio* methods. The Latin term *ab initio* translates to "from the beginning", indicating that a method attempts to calculate the properties of nuclei from first principles, i.e. starting with protons and neutrons as the degrees of freedom and using effective interactions between nucleons to build up a multi-nucleon system. This is a much more fundamental approach compared to the common CI-based or shell-model calculations with an inactive core discussed in Section 1.3.2. The goal of most *ab initio* methods is to solve the Schrödinger equation using nucleons as the degrees of freedom in "a systematically improvable approach for quantitatively describing nuclei using the finest resolution scale possible while maximizing its predictive capabilities" [63]. There are many *ab initio* approaches to solving the Schrödinger equation including Green's function Monte Carlo (GFMC) [64], Coupled cluster (CC) [65], Self-consistent Green's function (SCGF) [66, 67], and In-medium similarity renormalization group (IM-SRG) [68] to name a few, but here the NCSM and NCSMC will be discussed.

The NCSM solves the Schrödinger equation for a system of A point-like nucleons,

$$\hat{\mathcal{H}} \left|\Psi_A\right\rangle = E \left|\Psi_A\right\rangle , \tag{3.1}$$

where all nucleons are active and there is no inert core. The Hamiltonian is comprised of either two- or two-plus-three nucleon interactions that correlate nucleons in pairs and triplets

and can be written as,

$$\hat{\mathcal{H}} = \frac{1}{A}\sum_{i<j}\frac{(\boldsymbol{p_i}-\boldsymbol{p_j})^2}{2\mu} + \sum_{i<j}V_{ij} + \sum_{i<j<k}V_{ijk}, \tag{3.2}$$

where the first summation is over the relative kinetic energy between all nucleons using $\boldsymbol{p_i}$ as the momentum of particle i and μ as the reduced mass between nucleons. The second and third summations are over the effective interactions V_{ij} which represents the two-nucleon interaction potential, and V_{ijk} which represents the added three-nucleon interaction potential. These interactions, representing the strong nuclear force, could in theory be derived by quantum chromodynamics (QCD), except that at low energies where nuclear physics occurs, QCD is non-perturbative, making it currently intractable to solve even on the scale of a few nucleons. Thus, *Ab initio* methods must rely on effective two- and three-nucleon interactions constrained to fit a large collection of nucleon-nucleon scattering data, as well as the binding energies and other properties of light nuclei [69].

Recently, first principle approaches have incorporated many-nucleon interactions derived from χEFT. Introduced in the 1990's by Weinberg [70, 71, 72], chiral effective field theory (χEFT) is a low-energy approximation of QCD that preserves the symmetries of QCD within the low-energy nuclear physics domain. It provides Lagrangians that describe interactions among bound states of QCD - such as pions, nucleons, and deltas - which are then used to construct many-nucleon interactions. χEFTs are systematically improvable. They are formulated in terms of a small perturbative parameter Q/Λ_b, where Q represents the low-momentum characteristic of nuclear physics, and Λ_b denotes the high-energy scale at which the chiral-expansion breaks down.

To actually compute the eigenvector problem in the NCSM, the wave-function is expanded

in harmonic Oscillator (HO) basis states, $|\Phi_i\rangle$'s,

$$|\Psi_A\rangle = \sum_i^{N_{max}} c_i \, |\Phi_i\rangle \, , \tag{3.3}$$

up to a truncated maximum energy $N_{max}\hbar\Omega$ where Ω is the HO frequency. Increasing N_{max} will result in better and better approximations of the wave-function until the solution converges. The width of a HO potential is related to $\hbar\Omega$ and is an important choice to get the rapid convergence behavior of a HO wave-function. Poor choice in width results in a much larger N_{max} required to converge. The constants, c_i, from Eq. (3.3) are unknown but solving for the constants turns this problem into an eigenvector problem with a large matrix. The matrix dimensions scale rapidly with total nucleons, A, and N_{max}, requiring supercomputers to calculate eigenvalues and wave functions for even light nuclei.

The NCSM has become a commonly used method and has achieved good agreement between its calculated levels and experimental measurements. It has reached isotopes as heavy as ^{16}0 [73] and even up to ^{20}C [74]. Matrix elements[75] and quadrupole moments, such as those for ^{6}Li [62], have also been calculated by this method.

The No Core Shell Model with continuum (NCSMC) combines the NCSM with the addition of eigenstates from specific scattering mass partitions. The inclusion of scattering mass partitions makes the NCSMC well-suited to describe unbound resonances and clustering structure. The NCSMC from Vorabbi *et al.* [53] starts with the NNChiral interaction developed by Entem and Machleidt [76]. To build the wave-function for ^{7}Li, the 7-body harmonic oscillator states from the NCSM are mixed with the cluster expansion of scattering states,

$$\left|\Psi^{J^\pi T}_{A=7,\frac{1}{2}}\right\rangle = \sum_\lambda c^{J^\pi T}_\lambda \left|^7 Li \lambda J^\pi T\right\rangle + \sum_\nu \int dr \, r^2 \frac{\gamma^{J^\pi T}_\nu(r)}{r} \mathcal{A}_\nu \left|\Phi^{J^\pi T}_{\nu r,-\frac{1}{2}}\right\rangle . \tag{3.4}$$

In the right term of Eq. (3.4), $\gamma^{J^\pi T}_\nu(r)$ represents the continuous relative-motion ampli-

tudes, while $\mathcal{A}_\nu$ represents the antisymmetrizer. The antisymmetrized channel state can be expanded to represent scattering between mass partitions, in this case the p+^{6}He antisymmetrized channel state reads

$$\left|\Phi^{J^\pi T}_{\nu r,-\frac{1}{2}}\right\rangle = \left[\left(\left|^6He\lambda_6 J_6^{\pi_6} T_6\right\rangle \left|p\tfrac{1}{2}^+\tfrac{1}{2}\right\rangle\right)^{sT} Y_\ell(\hat{r}_6,1)\right]^{J^\pi T}_{\frac{1}{2}}, \tag{3.5}$$

where you can see the use of the NCSM results for ^{6}He included ($|^6He\lambda_6 J_6^{\pi_6} T_6\rangle$). Similar formulations are used for α+t and n+^{6}Li scattering channels, relevant for different excited ^{7}Li states.

Recently, the NCSMC method was used to predict a resonance in ^{7}Li just above the p+^{6}He threshold. The predicted resonance, discussed in Vorabbi et al. [53] Sec. III.B and throughout the rest of this chapter, is s-wave in nature (J^π=$1/2^+$), isospin T= 1/2, with a predicted excitation energy of E^*=10.2 MeV and width of Γ=130 keV. Such a state would be the lowest-energy positive-parity state in ^{7}Li. This prediction motivates the experiment presented in this chapter as a test of the predictive capabilities of the NCSMC method for near-threshold resonances.

3.3 Experimental methods

This experiment was performed at the Texas A&M University Cyclotron Institute with a primary ^{7}Li beam produced using the K150 cyclotron. The ^{7}Li(d,^{3}He)^{6}He reaction along with the Momentum Achromat Recoil Spectrometer (MARS), described in Appendix A.2, were used to produce a ^{6}He secondary beam at 6.4 MeV/nucleon with 75% purity (25% ^{3}H contaminant). The beam intensity, monitored by a 1-inch-diameter plastic scintillator at zero degrees, varied through the experiment between 1-8$\times10^4$ pps. The momentum acceptance

of MARS was ±1.2% with a beam spot approximately 10 mm in diameter at the target. The ^{6}He beam impinged on a secondary 2.65 mg/cm^2 CD_2 target, and the ^{6}He(d,n) reaction produced excited states of ^{7}Li.

The Gobbi setup, described in Section 2.2.1, was employed at a distance of 23.5 cm downstream from the the target. In the analysis, "Punch-through" protons with an energy higher than 15.5 MeV were gated out of the data because the range approaches the 1.5 mm thickness of the E detector. A gate on the relative time between the ΔE and E pairs was applied to each particle identification as well as a requirement that strips spatially match between layers.

The particle-unbound excited states of light nuclei around ^{7}Li were studied using the invariant-mass method, where correlations between decay fragments are reconstructed to give the parent excitation energy [77]. Selected, well known, states in ^{6,7}Li and ^{8}Be were used to confirm the calibration as well as constrain simulations. These calibration resonances are shown in Fig. 3.3 with fit values summarized in Table 3.1. The intense ^{6}Li ($J^\pi=3^+$) resonance, shown in Fig. 3.3(a), was checked to be consistent across all decay angles to ensure the transverse decays perpendicular to the beam axis (primarily dependent on position information) and longitudinal decays parallel to the beam axis (primarily dependent on the energy calibration) reconstructed to the same excitation energy. The ^{7}Li ($J^\pi=7/2^+$) resonance, shown in Fig. 3.3(b) decaying to the t+^{4}He channel, was measured to be 9 keV lower than the evaluated energy but a width 23 keV wider. Three states of ^{8}Be, shown in Fig. 3.3(c)(d), were found to agree with their evaluated parameters except for the extremely narrow ground-state width that was outside of our sensitivity range and the energy of the 1_2^+ level which was only slightly out of agreement and likely due to the choice of background. Comparing the evaluated and measured energies in Table 3.1, a systematic uncertainty of 10 keV is deduced.

Tab. 3.1: Comparison between the TUNL evaluations [78, 79] and the current measurements for states in ^{6,7}Li and ^{8}Be. Uncertainties on the measured values represent the statistical uncertainty of the fit.

		Evaluated [78, 79]		Measured	
Nuclei	state	E^* (MeV)	Γ (keV)	E^* (MeV)[a]	Γ (keV)
^{6}Li	3^+	2.186(2)	24(2)	2.187	-[b]
^{7}Li	$7/2^+$	4.652	69	4.643(1)	92(4)
^{8}Be	0^+, g.s.	0	5.5×10^{-3}	0.0017(3)	0.004(1)
	1^+_1	17.640(1)	10.7(5)	17.646(2)	15(4)
	1^+_2	18.150(4)	138(6)	18.170(10)	158(27)

[a] Decay energies are measured and then shifted by the reaction Q-value determined from the ground state energies of the AME2020 mass evaluations [2].
[b] Fixed.

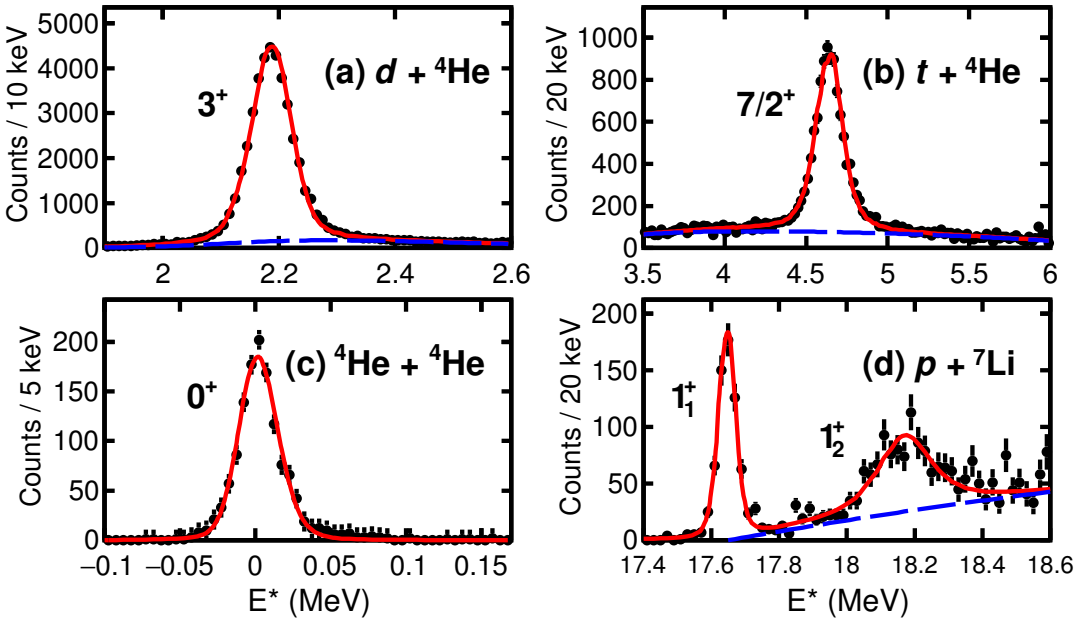

Fig. 3.3: Efficiency-corrected invariant-mass reconstructions along with simulations fitted to determine the energy and width for: (a) ^{6}Li (3^{+}) from charge exchange of the ^{6}He beam, (b) inelastically excited ^{7}Li ($7/2^{-}$) from a primary ^{7}Li beam on the CD_2 target, and (c), (d) near-threshold states ^{8}Be (g.s.), ^{8}Be (1^{+}_{1}), and ^{8}Be from proton pickup on a primary ^{7}Li beam. In each fit, the red solid line indicates the total fit with the background component indicated by a blue dashed line.

3.4 Results

The efficiency-corrected excitation-energy spectrum of ^{7}Li from detected p+^{6}He fragments is shown in Fig. 3.4. This figure shows the total fit (red solid line) with two resonances (green dotted lines) and a linear background (blue dashed line). The first and most prominent resonance observed is at $E^{*}_{1} = 11.295 \pm 0.010(syst.)$ MeV, $\Gamma_1 = 184 \pm 13(stat.)$ keV which is the Isobaric Analog state (IAS) with (J^{π},T) = ($3/2^{-}$, 3/2) [80]. This high-resolution experiment also revealed a high-energy shoulder to the IAS indicating a previously unreported state at $E^{*}_{2} = 11.66 \pm 0.04(stat.)$ MeV, $\Gamma_2 = 320 \pm 90(stat.)$ keV.

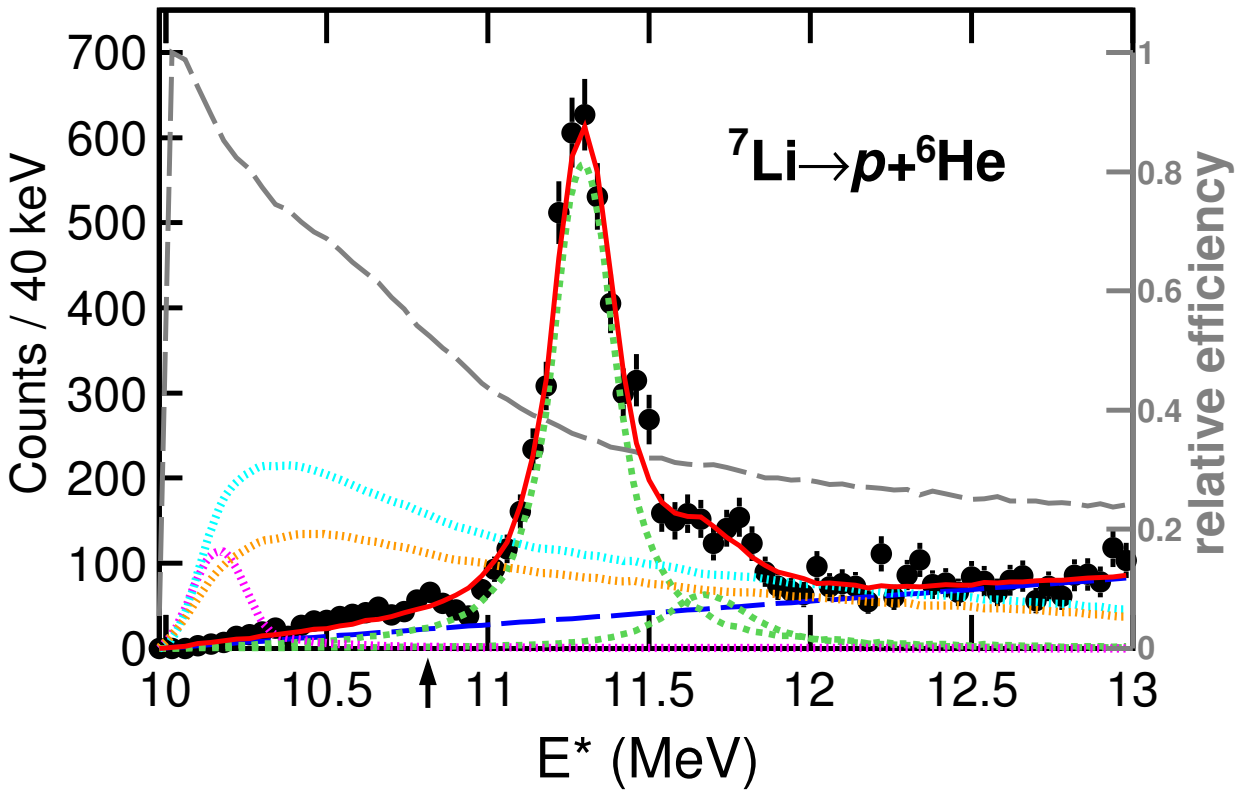

Fig. 3.4: Efficiency-corrected and fitted excitation-energy spectrum for ^{7}Li→p+^{6}He. The dotted lines represent the simulated resonances where the blue dashed line is a linear background. The magenta finely-dotted peak (not included in the fit) represents the predicted $1/2^+$ state with Breit-Wigner line shape and a small spectroscopic factor ($C^2S = 0.02$). The sharply rising and slowly decaying cyan and orange finely-dotted lines are two-channel R-matrix line shapes (including n and p decay channels). The cyan (orange) line corresponds to a resonance energy at E^*=10.2 (10.04) MeV. The detector efficiency is overlaid in a grey dashed line with a separate axis on the right. The thresholds for the p+^{6}He and n+^{6}Li (0^+,1) channels are at E^*=9.975 MeV (edge of axis) and E^*=10.813 MeV (arrow on axis), respectively.

Peaks were assumed to have Breit-Wigner intrinsic line shapes with the experimental resolution and efficiency included via a Monte Carlo simulation taking into account the geometry, energy deposition, and energy thresholds [77]. Realistic beam properties such as

momentum distribution and beam size were also included in the sampling. The simulation used energy deposition determined per particle based on energy losses calculated from the SRIM software package [81] while the thresholds were taken from the experiment. Simulation parameters for scattering angle and energy resolution were tuned to fit the energy and width of the ^{6}Li (3^+) state for both longitudinal and transverse decays relative to the beam line.

The plots of the heavy fragment angle, θ_H, vs. decay energy from the simulation are seen in Fig. 3.5. The background distribution in Fig. 3.5(a) matches the simulation of a uniform decay energy distribution in Fig. 3.5(b), effectively showing the efficiency as a function of decay angle and decay energy. The telescope geometry was located at a large distance from the target to optimize the detection efficiency for low p+^{6}He relative energies while sacrificing the efficiency at high energies. The ^{7}Li$\rightarrow$ p+^{6}He efficiency shown (gray dashed line) in Fig. 3.4, is a projection of the uniform decay energy simulation seen in Fig. 3.5(b).

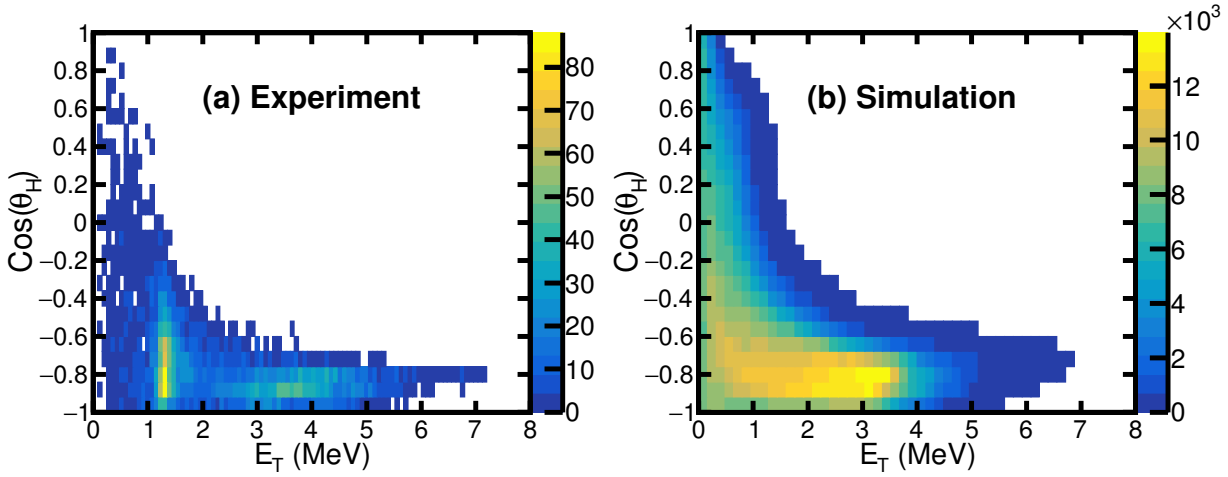

Fig. 3.5: (a) Data for the cosine of the heavy fragment's angle relative to the beam direction vs the decay energy. The IAS is clearly visible at ≈1.3 MeV but the background distribution is what should be compared. (b) Simulation of a uniform decay distribution to give the efficiency as a function of decay energy and decay angle.

The fitted parameters for the IAS of $E_1^* = 11.295 \pm 0.010(syst.)$ MeV, $\Gamma_1 = 184 \pm 13(stat.)$

keV are an update to the evaluated energy and width of $E^*_{IAS} = 11.24 \pm 0.30$ MeV, $\Gamma_{IAS} = 260 \pm 35$ keV [78]. This is also higher in energy than Ref. [82], which measured $E^*_1 = 11.262 \pm 0.015(syst.)$ MeV, but does agree with the measured width from that work [82] of $\Gamma_1 = 191 \pm 41(stat.)$ keV. With low statistical uncertainty compared to the systematic uncertainty, the presumed systematic uncertainty was assigned for the IAS. For the previously unobserved state at $E^*_2 = 11.66 \pm 0.04(stat.)$ MeV, with $\Gamma_2 = 320 \pm 90(stat.)$ keV, the uncertainties result from the correlated statistical uncertainties which dominate. The broader evaluated width for the IAS may have been a result of this broad unresolved second state at E^*_2.

Using the NCSMC method, the near-threshold resonance in ^{7}Li at E*=10.2 MeV was predicted as a positive-parity proton s-wave resonance with (J^π,T) = ($1/2^+$, 1/2) [53]. A sharp increase in phase shift in the p+^{6}He scattering with an intrinsic width of Γ=130 keV was a robust prediction from this implementation of the NCSMC with a note that this state could have implications to the astrophysical S-factor in the ^{6}He(p,γ)^{7}Li radiative-capture reaction [53]. An estimate of the cross section for such a state was calculated using FRESCO [83], a general purpose reaction code. For both observed states, optical-model parameters for the d+^{6}He entrance channel and p+^{6}He exit channel were taken from d+^{6}Li scattering [84] and p+^{6}Li scattering respectively [85]. The differential cross sections resulting from FRESCO were used in the simulation of the efficiency.

To check for consistency, the yield of the IAS was studied. The cross section for the IAS was calculated using a spectroscopic factor of 0.199 obtained in the p-shell model space with the CKPOT Hamiltonian [86] using the code Oxbash [10]. As most IAS decays are to the open n+^{6}Li (0^+,1) channel, the predicted cross section of the IAS peak was reduced by the proton branching ratio of 0.35 calculated in a two-channel R-matrix approximation with resonance parameters constrained to the measured values. The deduced cross section of the IAS peak, using the number of incident beam particles measured with the plastic scintillator

at zero degrees and adjusted for the spectroscopic factor and branching ratio, was found to be consistent with the FRESCO cross section.

Simulation of the proposed $1/2^+$ state (magenta finely-dotted line in Fig. 3.4), with no neutron branch but with a tiny spectroscopic strength of only $C^2S = 0.02$, is shown in Fig. 3.4. The observed yield is far less than even this and in fact no evidence of a narrow state at 10.2 MeV is seen at all.

Line shapes obtained from two-channel R-matrix calculations [31] were also considered to see the affect of some n+^{6}Li strength in the wave function. The neutron reduced width was set to be 10% of the proton value with the latter set equal to the Wigner limit [87]. The inclusion of the small strength for the n+^{6}Li channel makes the width of the state quite wide and the p+^{6}He line shape has a very long tail. The final p+^{6}He line shape was further modified by scaling with the excitation-energy dependence of the FRESCO predictions for the resonance yield. Predictions with a spectroscopic factor of 0.9 in FRESCO and for R-matrix resonant energies of 10.2 MeV and 10.04 MeV, are also shown in Fig. 3.4 by the finely-dotted cyan and orange lines respectively. Adding the n+^{6}Li channel allows proton penetration through the high-energy tail of a wider resonance and, as a consequence, the proton branching ratio is only weakly affected by decreasing resonance energy. In both of the two-channel cases considered, one expects to observe a sharp increase in the p+^{6}He yield near the threshold followed by a long decreasing tail. As these features are not observed, these data also exclude a resonance with energy from just above the proton threshold to that of the IAS (11.3 MeV), unless the neutron reduced width exceeds the proton reduced width.

3.5 Conclusion

This experiment shows no evidence for a s-wave resonance in ^{7}Li just above the p+^{6}He decay threshold. As our experiment was sensitive to both narrow and sharply rising but broad proton resonances, the latter expectation from two-channel R-matrix calculations, we can exclude any state with energy between the proton threshold and the IAS with large proton spectroscopic strength. While a state could exist in this energy region that primarily decays through the n+^{6}Li or ^{4}He+d+n channels, it is not clear how such a state is related to the predicted narrow proton resonance just above the proton threshold.

The theory work that predicted this state mentions three issues in the calculations which could explain why this state might not exist [53]. First, the calculation only includes two-body interactions while the structure of this state is in the three-body ^{4}He+d+n continuum. Perhaps there is an analogy to the structure of ^{6}He, which is thought of as a halo nucleus consisting of a ^{4}He core and two valance neutrons. This suggests a three-body treatment [27]. Another potential problem is that the mass partitions are not coupled. A calculation including the coupling of the open two-body mass partitions might provide an explanation of why we did not observe this resonance, should it exist. The final potential issue is that the calculations only use a two-nucleon chiral interaction where a chiral three-nucleon interaction might yield different results. However, the omission of the three-nucleon interaction is unlikely to erase a resonance that is so conspicuous, being seen in both the n+^{6}Li and p+^{6}He mass partitions, with only the two-nucleon interaction. Unfortunately the likely explanation, the first mentioned above, is also the hardest to test. The resonance might disappear in a calculation that considers the three-body ^{4}He+d+n continuum, an approach the NCSMC is currently unequipped to perform.

The newly observed wide state at E_2^*=11.66(4) MeV might match a different prediction

from the NCSMC results, namely a (J^π,T) = ($3/2^-$, 1/2) resonance which is only seen in the p+^{6}He mass partition. This prediction suggests a $p_{3/2}$ resonance at E^*=11.92 MeV with a width of Γ = 410 keV, an overprediction of approximately 260 keV in energy. The IAS was similarly calculated higher in energy by about 420 keV but over-shot the width by a large margin. With a ($3/2^-$, 1/2) spin-parity assignment and an energy near the IAS, this could indicate the observed resonance is a part of the collectivized anti-analog strength, having the same spin and parity as the isobaric analog but with T=1/2 [88].

Chapter 4

Measurement of the p/γ Branching Ratio for the 2^+ State of ^{36}Ca

4.1 Motivation

While the ground state of ^{36}Ca is bound, with a β^- decay half-life of 100.1 ms [89], the first 2^+ state at E* = 3.049 MeV is unbound to proton emission. This quasi-bound excited state has a large Coulomb barrier relative to its available one proton decay energy of 0.449 MeV, making gamma emission and one proton emission competitive. Figure 4.1 shows a simplified energy level diagram indicating this $J^\pi = 2^+$ state with its decay paths. The simultaneous emission of two protons to ^{34}Ar is also energetically allowed for the 2^+ state but is kinetically suppressed because the Coulomb barrier is about twice as large as that for one-proton emission.

In the next chapter, Chapter 5, the measurement of the $B(E2; 0_1^+ \rightarrow 2_1^+)$ for ^{36}Ca is presented, a result that relies on measuring the Coulomb-excitation cross section for producing the 2^+ state. In that work, only the gamma decay was measured, making the experiment blind to an excitation which decayed through proton emission. To account for excitations which proton decayed, the p/γ branching ratio is measured and reported in this chapter.

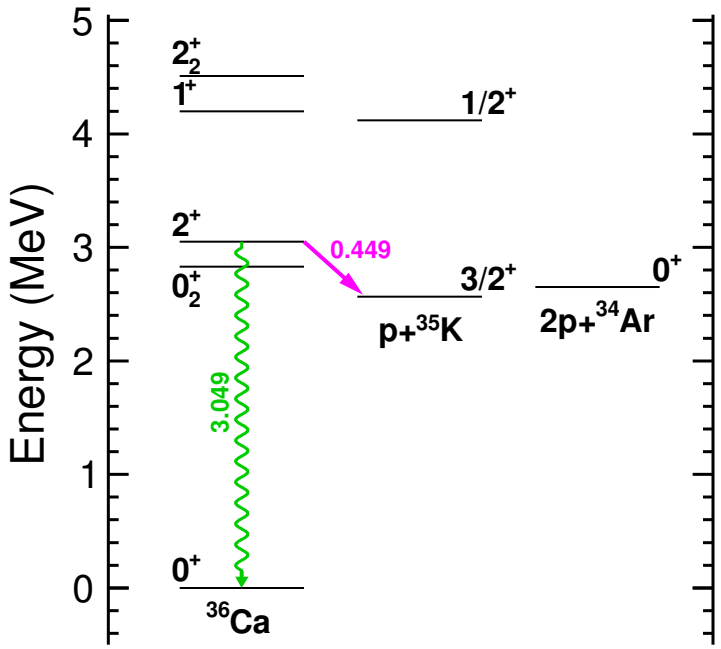

Fig. 4.1: Level schemes for ^{36}Ca showing levels relevant to this paper. The one- and two-proton separation energies for ^{36}Ca are adapted from Ref. [90] with levels in ^{36}Ca taken from this work.

The branching ratio measurement, paired with the $B(E2; 0^+_1 \rightarrow 2^+_1)$ value, also gives the partial proton decay width Γ_p.

4.2 Experimental methods

This experiment used the NSCL setup, described in detail in Section 2.2.2, and was sensitive to both γ- and proton-decay branches. A primary 140-MeV/nucleon ^{40}Ca beam impinged on a Be target to remove three neutrons and the A1900 fragment separator was used to produce a ^{37}Ca secondary beam with a purity of 40%. This secondary beam at 72 MeV/nucleon impinged on a 0.5-mm-thick Be target. The subsequent knock out of one more neutron populated states of ^{36}Ca, including the ground and 2^+ states of interest [91].

Gamma rays detected by CAESAR gated on a ^{36}Ca residue recorded in the S800 provide the number of $^{36}\mathrm{Ca} + \gamma$ events. Protons detected in the $\Delta E - E$ ring telescope in coincidence with ^{35}K residues are used for the invariant-mass reconstruction. These two quantities constitute the branching ratio measurement as,

$$B_p = \frac{\#(^{35}K + p)}{\#(^{36}Ca + \gamma) + \#(^{35}K + p)} \,. \tag{4.1}$$

To relate the quantities in this equation to experimental observables, we define N_p and N_γ as the number of detected proton and γ-ray decays, and ε_γ as CAESAR's γ-ray efficiency, ε_p for the $\Delta E - E$ ring-telescope efficiency for protons, and $\varepsilon_{35K}/\varepsilon_{36Ca}$ for a relative S800 & SFA efficiency for the two residues. A beam intensity I_p or I_γ is required to normalize the counts from the different S800 settings required for the two decay paths. Employing these quantities and efficiencies, the branching ratio measurement is,

$$B_p = \frac{N_p/\varepsilon_p}{(\frac{N_\gamma}{\varepsilon_\gamma})(\frac{\varepsilon_{35K}}{\varepsilon_{36Ca}})(\frac{I_p}{I_\gamma}) + \frac{N_p}{\varepsilon_p}} \,. \tag{4.2}$$

4.3 Gamma-decay branch

The CAESAR γ-ray energy spectrum recorded in coincidence with ^{36}Ca in the S800 is plotted in Fig. 4.2. Each event was Doppler corrected according to Eq. (2.5) using the measured velocity of the ^{36}Ca residue in the S800 and an angle between the target center and the center of the CAESAR crystal that registered the highest energy deposition. No add-back between neighboring detectors was applied.

For an estimate of the background, the $^{35}\mathrm{K} + \gamma$ channel was employed as only ^{35}K(g.s.) is particle-bound with no excited states that decay through γ-ray emission. All detected γ rays in coincidence with ^{35}K must be from background processes. This background was

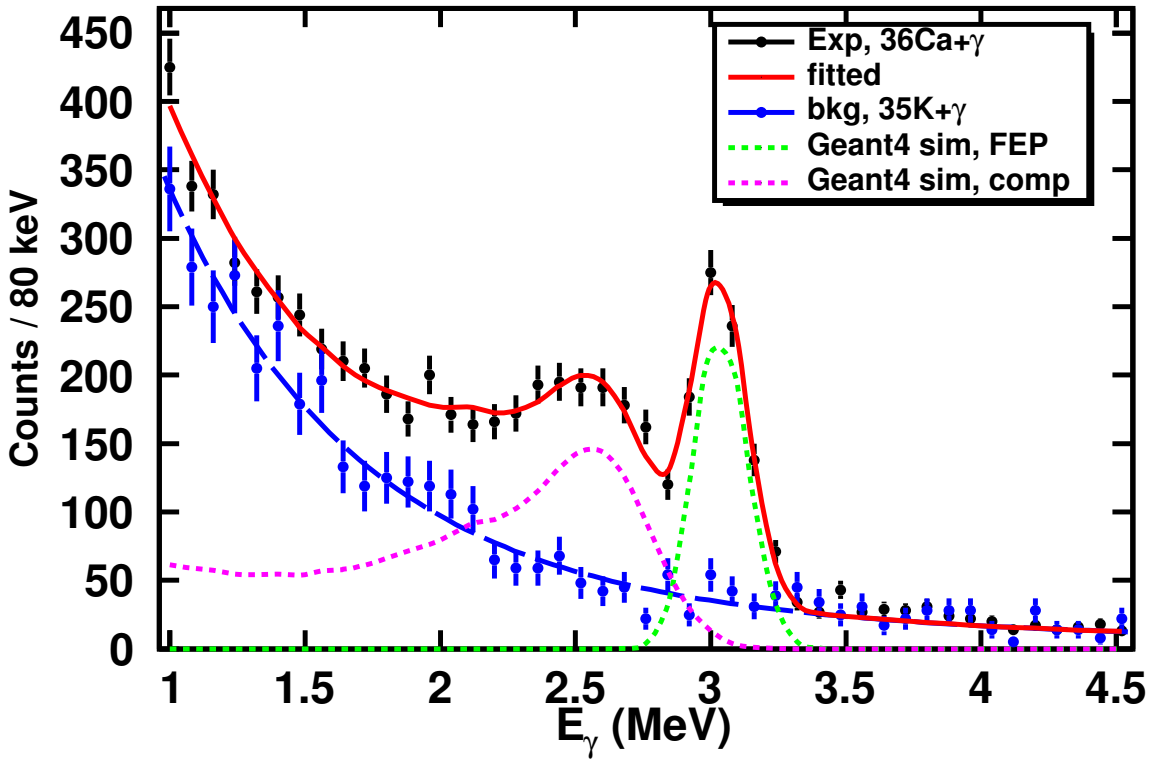

Fig. 4.2: Fit of the γ-ray-energy spectrum in coincidence with an identified ^{36}Ca residue. The shape of the background component (blue curve) taken as a double exponential fit to the blue data points from ^{35}K+γ events. The full-energy peak (green curve) and Compton-scattering and pair-production components (magenta curve) were obtained from GEANT4/UCCAESAR simulations. The magnitudes of all three components were varied in the fit with the scaling of the FEP giving $N_\gamma/\varepsilon_\gamma$.

incorporated into the fit shown in Fig. 4.2 in three ways: by fitting a double exponential to this background data, by applying a smoothing function to this background data, or by scaling the contribution based on the ratio of ^{35}K to ^{36}Ca residues detected in the S800. The last of which yielded an efficiency that was consistently between the other two and within the systematic error reported.

UCCAESAR [92, 93], a simulation code built on the GEANT4 [94] toolkit, was used to handle the detector efficiency and response. The efficiency was used to convert the number

of detected γ-ray events into the number of ^{36}Ca(2^+) events that decayed through γ-ray emission, $N_\gamma/\varepsilon_\gamma$. The detector response was split into the full-energy-peak (FEP) detection and Compton-scattered or escape peaks (comp).

Through multiple fits, it was determined that $N_\gamma/\varepsilon_\gamma = 7800 \pm 356(stat.) \pm 470(syst.)$. The origin of the systematic uncertainty comes from the different methods used to fit the simulation of the 3.049-MeV γ ray. First, the plot was fitted with a double exponential describing the background where the detector resolution was varied as well as the range of the fit. Varying the resolution and range of the fit both gave values within the average statistical uncertainty and resulted in a value of $N_\gamma/\varepsilon_\gamma = 8063 \pm 309(stat.)$. This process was repeated with the same background, except a smoothing function was applied before fitting, resulting in a lower value $N_\gamma/\varepsilon_\gamma = 7539 \pm 355(stat.)$. This larger statistical uncertainty was chosen for the overall statistical uncertainty. For the systematic uncertainty, the highest and lowest value from all of these fits gives the range of N_γ, where the range/2 is used for a systematic uncertainty. The systematic uncertainty was calculated to be $\delta(N_\gamma/\varepsilon_\gamma)(syst.) = 470$.

4.3.1 Efficiency Test Case, ^{8}B $\Rightarrow$ ^{6}Li(IAS) + 2p

In order to gain some confidence in our procedure for determining $N_\gamma/\varepsilon_\gamma$, a test case was used from a different experiment that used CAESAR combined with IMS. Here we examined the ^{6}Li + 2p decay of ^{8}B fragments produced from the proton knockout of an $E/A = 68$ MeV ^{9}C beam [95]. The ^{6}Li + 2p invariant-mass spectra of Fig. 4.3(a) shows the 0^+ excited state of ^{8}B as a prominent peak sitting on a background free region [95]. This state is the IAS of ^{8}C$_{g.s.}$ with an isospin of T=2. The only isospin-allowed decay available is the 2p decay to the (0^+, T=1) IAS state at E*=3.563 MeV in ^{6}Li which is known to γ-decay. This decay path is shown in the insert of Fig. 4.3(a).

Gating on the (0^+, T=2) state in the two-proton decay, the coincidence γ-decay spectrum is examined in Fig. 4.3(b). Each of the 4125 two-proton decays in the red gate feeds the IAS of ^{6}Li resulting in a gamma emission. Fitting the γ-decay spectrum with the GEANT4/UCCAESAR simulations gives the total number of gamma decays, $N_\gamma/\varepsilon_\gamma$, to be $4086 \pm 108(stat.)$ a number only 0.94% different than expected from the number of ^{8}B(0^+, T=1) parents counted which always feed the ^{6}Li(IAS). The background for this fit was taken from gamma decays in coincidence with ^{3}He+^{4}He fragments from the decay of ^{7}Be which should not produce any gamma decaying excited states. Qualitatively, the fit in the ^{6}Li(IAS) case isn't as good as the ^{36}Ca $+\gamma$ case because the energy of the emitted gamma decay was fixed in simulation. In addition, the FEP statistics are lower than the ^{36}Ca $+\gamma$ case, but since the value of $N_\gamma/\varepsilon_\gamma$ reproduces the number of events determined by the invariant-mass gate, we are confident in our efficiency and determination of $N_\gamma/\varepsilon_\gamma$ in the ^{36}Ca $+\gamma$ case.

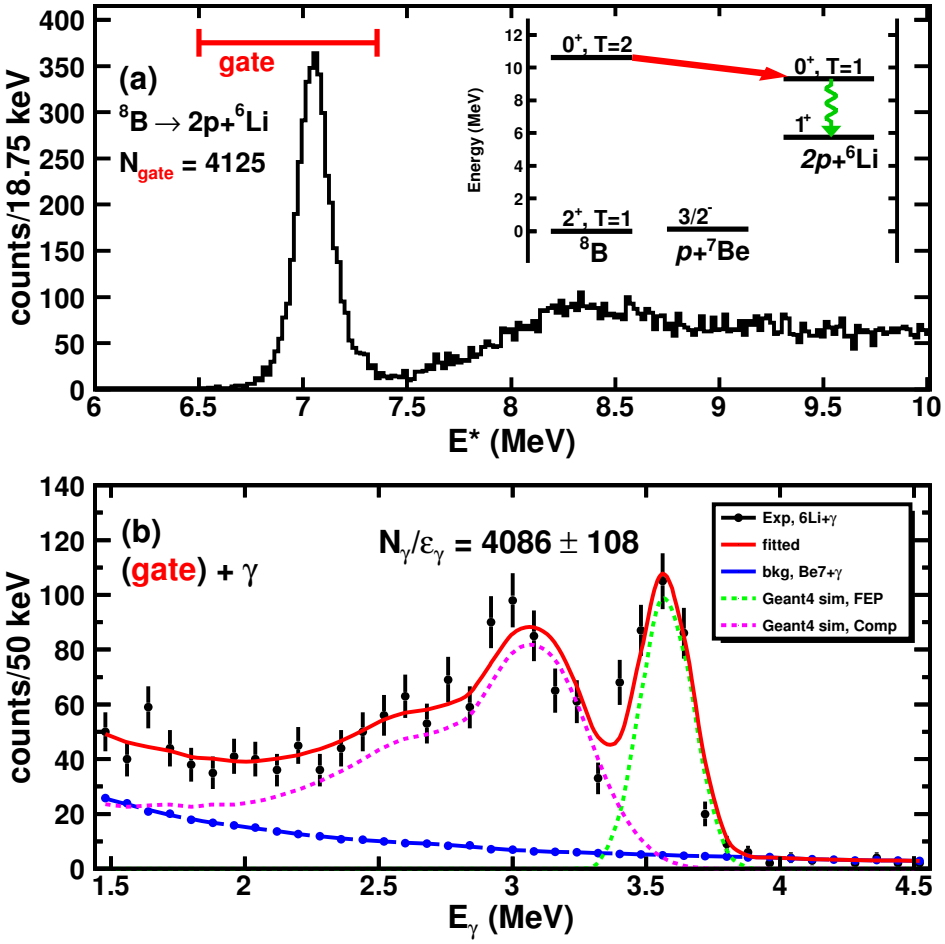

Fig. 4.3: (a) Invariant-mass spectrum of ^{8}B decaying to $2p$ + ^{6}Li. The peak centered at 7.06 MeV results from populating the IAS in ^{6}Li, each of which can only decay via emitting a 3.563 MeV γ ray. (b) Gamma events in coincidence with the above gate, fitted to extract $N_\gamma/\varepsilon_\gamma = 4086 \pm 108$ which is within tolerance of the expected value of 4125.

4.4 Proton-decay branch

The ^{36}Ca excitation spectrum obtained with the invariant-mass method is shown in Fig. 4.4 where the gate used to select the events from the decay of the 2^+ state is shown in magenta. The 2^+ peak in ^{36}Ca lies in a region of the experimental spectrum with virtually no back-

ground and thus the peak can be directly integrated to find the number of detected proton decays, $N_p = 292 \pm 17(stat.)$.

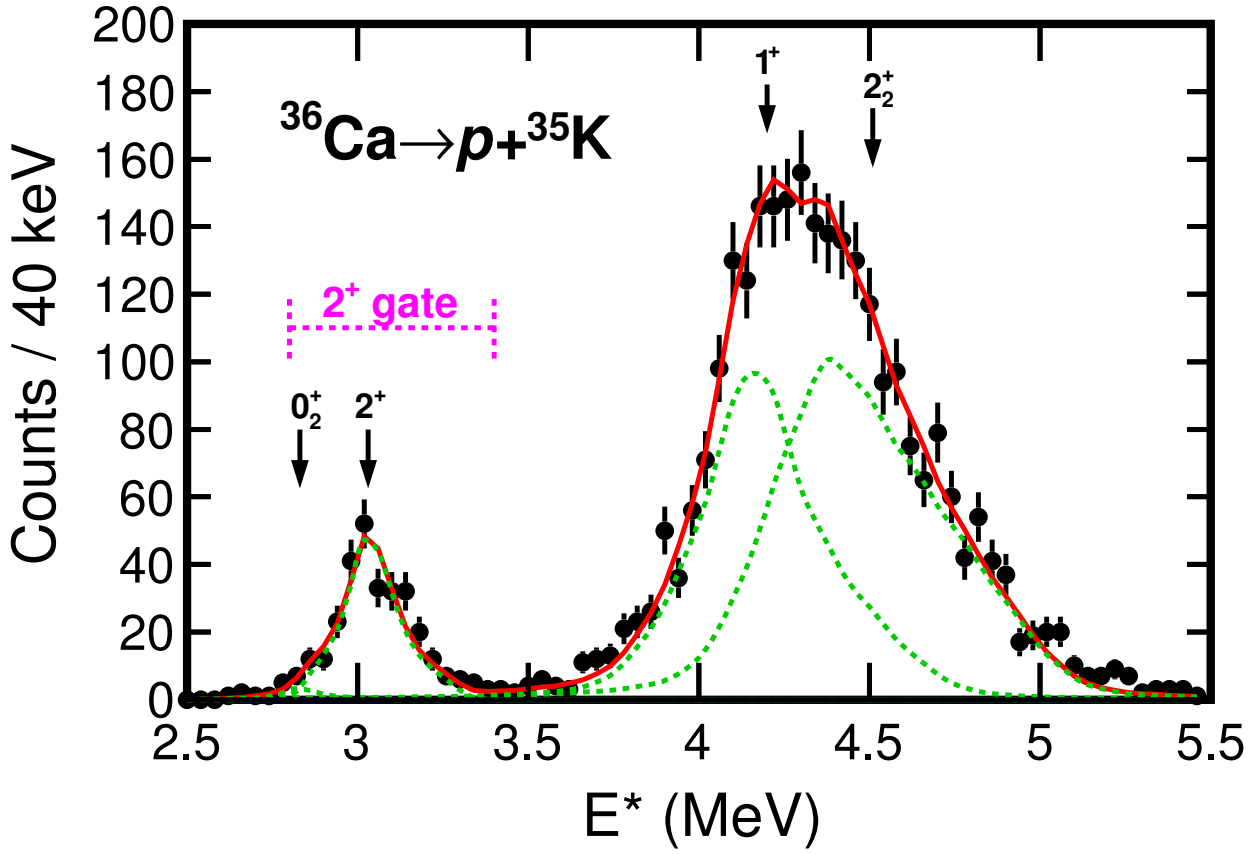

Fig. 4.4: Excitation-energy spectrum of ^{36}Ca fitted (red line) with four peaks (green dotted curves) and with arrows indicating the spin-parity. No background was required in fitting the ^{36}Ca data. The magenta-dotted gate indicates the upper and lower limits of the 2^+ state which were integrated to determine N_p.

There is a question on possible contributions from the decay of the 0^+_2 state which is expected to have a similar excitation energy as the 2^+_1 state. The recent measurement of Lalanne *et al.* [96] found the 0^+_2 state lies 230(13) keV below the 2^+_1 state [96] and was isolated by gating on a ^{36}Ca fragment in their zero-degree detector. The 0^+_2 state is included in the fit of Fig. 4.4 at a fixed energy primarily to show there was little to no detected

events. This suggests that if the 0_2^+ state proton decays, it would have a long lifetime. The excited residue would travel a substantial distance before decay and miss our charged-particle telescope. Indeed with its lower excitation energy, the d-wave partial proton decay width of this state is heavily retarded. Single-particle estimates with the quoted level energy are $\approx 10^{-9}$ eV suggesting that we should not have observed any contributions from this state in our invariant-mass spectrum. Additionally, we do not expect the 0_2^+ state to be significantly populated as the spectroscopic factors for neutron knockout from ^{37}Ca to the 2_1^+ and 0_2^+ states are 0.42 and 0.02, respectively (calculated using the ZBM2 interaction [16]).

The proton detection efficiency was simulated with the S800 acceptance, using Monte Carlo simulations taking into account the geometry as well as other constraints [77]. The simulation resulted in a detection efficiency of $\varepsilon_p = 0.764(5)$. One important contribution to the detection efficiency was the effect of a gap in the ring telescope between the inner and outer rings of CsI(Tl) crystals. In the gap, protons can pass through the inner ring and either stop in the wrapping material of the crystals or cross into the outer ring of crystals, resulting in a loss of proton identification efficiency. The magnitude of this loss was determined using singly-detected protons with kinetic energy in the same range as those associated with the decay of the 2^+ state. The yield of these identified protons, shown in Fig. 4.5, varies smoothly as a function of the ring number of the S4 silicon detector except for ring numbers from 45 to 55 where a dip in the yield from this effect is observed. A correction to the proton detection efficiency for these rings is determined from the reduction relative to a linear interpolation based on the neighboring strips (shown by the red line in Fig. 4.5). In addition to this, an efficiency loss of $\sim 5\%$ due to protons undergoing nuclear reactions in the CsI(Tl) crystals was also taken into account [97].

Included in the uncertainty evaluation of the simulated proton efficiency is the reported uncertainty of the proton decay energy of the 2^+ state $E_r = 449(6)$ keV [98]. Starting from a

spin 2^+ state and decaying by either a $s_{1/2}$ or $d_{3/2}$-wave proton to the $J=\frac{3}{2}$ residue produces an isotropic emission pattern. We assumed isotropic emission in the simulation. Mixing of the $s_{1/2}$ and $d_{3/2}$ components could lead to some deviation from isotropy but such a deviation could not be discerned.

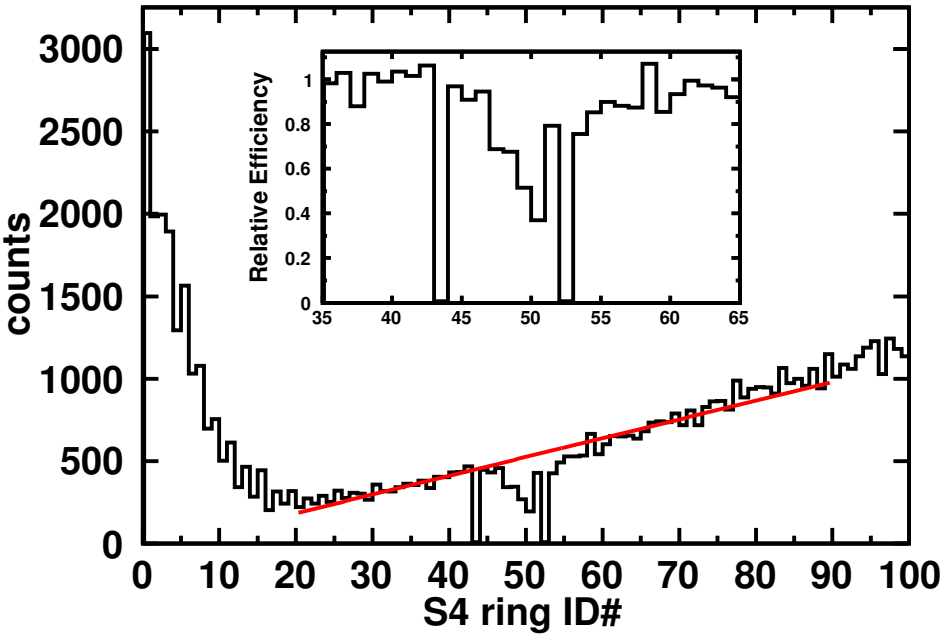

Fig. 4.5: Distribution of identified protons as a function of S4 ring number. The dip in the distribution from ring numbers 45 to 55 occurs near the location where the inner and outer CsI(Tl) crystals meet. This region also includes the two rings of the S4 which acquired no usable data. The inset shows the contribution to the efficiency as a function of silicon ring number used in the simulation to incorporate these effects.

4.5 Relative efficiency and beam current

To get the relative detection efficiency for ^{35}K vs ^{36}Ca residues, simulations with relativistic kinematics and the geometry of the setup were performed. The results of the efficiency simulations gave $\varepsilon_{35K}/\varepsilon_{36Ca} = 1.03(3)$.

The simulations were set up with a beam-momentum width of ±1% and a radial beam profile that was either Gaussian or uniform in shape. The difference between these simulations is included in the uncertainty estimates. The beam radius was adjusted such that 70% of the beam was transmitted through the $\Delta E - E$ ring telescope to the S800, a value matching what was measured. Variation in beam profile and radius only result in a ±1% effect on the value of $\varepsilon_{35K}/\varepsilon_{36Ca}$.

Energy-loss calculations were performed for the target and SFA. Efficiency losses through the SFA were assumed to be the same for ^{36}Ca and ^{35}K fragments and thus do not modify the ratio. Transverse and longitudinal momentum distributions after one-neutron knockout of ^{37}Ca to ^{36}Ca(2^+) were calculated with the code MOMDIS [99], assuming 80 : 20 mixing of the $\ell = 0 : 2$ momentum transfers [91]. The longitudinal momentum distributions from MOMDIS, which does not conserve energy, were terminated at the maximum possible value consistent with energy and momentum conservation removing the predicted high-energy tail of this distribution. Variations in the momentum distribution were considered by increasing or decreasing the momentum scale by ±20%. Overall, the details of the momentum distributions have a minor effect on $\varepsilon_{35K}/\varepsilon_{36Ca}$ resulting in a ±3% effect on the ratio.

Different rigidity settings of the S800 were used, one optimized for the detection of ^{36}Ca that was used for the γ-ray spectrum and the other optimized for ^{35}K that was used for the p-decay spectrum. The S800 nominally has ±3% momentum acceptance in focus mode, but for the detection of ^{36}Ca fragments a blocking slit was used to reduce the rate of ^{37}Ca at the focal plane in order to increase acquisition live-time. This blocker restricted the S800 high-momentum acceptance further. The high-rigidity cutoff from this blocker was determined from the S800 rigidity spectrum for ^{37}Ca. The location of this cut-off was varied in the simulation to fit the measured distribution. The uncertainty from this fit gives the largest contribution to the uncertainty for ε_{36Ca}. The final simulated ^{35}K rigidity distribution

associated with the 2^+ state matches the experiment quite well and can be seen in Fig. 4.6 where the ^{36}Ca gated on the 2^+ gamma peak (blue) has the $\approx 25\%$ background removed based on the rigidity of all ^{36}Ca in the S800.

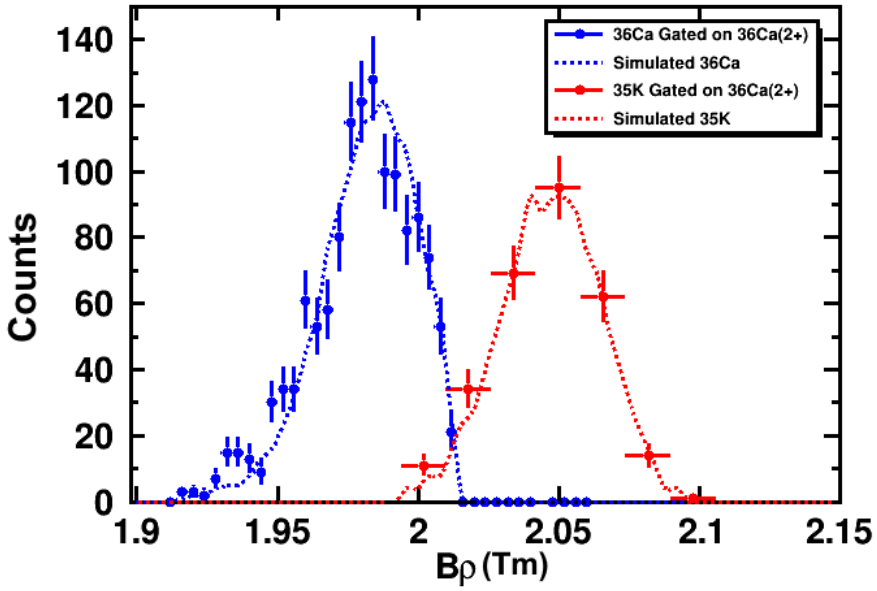

Fig. 4.6: Data (points) vs simulation (dotted lines) of the resulting rigidity for ^{36}Ca (blue) gated on the 2^+ gamma peak and ^{35}K (red) gated on the 2^+ invariant-mass peak. Simulation results were scaled to the experimental results based on the total number of events.

The number of projectiles was determined by integrating the gates for beam identification in Fig. 2.8 that plots the ToF between the A1900 focal plane scintillator and S800 object plane scintillator. The total integrated beam was $I_p = 2.02 \times 10^9$ particles during the S800 setting sensitive to ^{35}K and $I_\gamma = 4.05 \times 10^9$ particles during the S800 setting sensitive to ^{36}Ca. A random pulser was used to determine the different acquisition dead times for the two settings. Beam purity was constant throughout the experiment.

4.6 Branching-ratio measurement

For the 2^+ state in ^{36}Ca, the observed gamma-decay branch corrected for efficiency was determined to be $N_\gamma/\varepsilon_\gamma = 7800 \pm 356(stat.) \pm 470(syst.)$. Assuming the statistical and systematic errors are uncorrelated, the uncertainties are added in quadrature, resulting in a total uncertainty of 590 counts or a 7.5% fractional uncertainty, resulting in the largest contribution to the final measured branching ratio uncertainty. The observed proton-decay branch corrected for efficiency was determined to be $N_p/\varepsilon_p = 382 \pm 22(stat.)$. The relative residue detection efficiency was simulated to be $\varepsilon_{35K}/\varepsilon_{36Ca} = 1.03(3)$ and the ratio of beam intensity was determined to be $I_p/I_\gamma = 0.499$. Using these measured values in Eq. (4.2) gives a proton branching ratio of $B_p = 0.087(8)$. This value is a small correction to the observed Coulomb-excitation cross section leading to γ-ray emission, a measurement repoted in Chapter 5.

Our measured B_p is not in agreement with the value deduced using the ^{37}Ca(p,d)^{36}Ca transfer reaction (0.165(10)) [98] but agrees well with the value measured using ^{36}Ca scattering on ^{nat}Pb ($0.091\ ^{+0.034}_{-0.019}$) [100]. With three independent measurements, it is clear there is a discrepancy in measured values. Looking at the origin of these numbers the higher measured B_p value from Ref. [98] was measured using data from a transfer reaction in two ways, one through integrating the angular correlation function and the other through the observed counts in the feeding of the 2^+ state from different gates. There was a strong agreement between the two methods within the same report, but the proton decay branch was observed and fit using only 2-3 data points. In this report, no mention of efficiency corrections were discussed. In the result from Ref. [100], which was in agreement with the branching ratio measured here, the result was highly limited by statistics of both decay branches and the resolution of the proton decay branch. Their measurement was very similar to the one pre-

sented in this chapter where the γ- and p-decay branch were measured except a Coulomb excitation reaction was employeed to populate the state. The work in this chapter was at a much higher resolution and the determination of the efficiency contributed the most to the uncertainty.

Chapter 5

Analysis of the $B(E2\uparrow)$ Strengths of ^{36}Ca and ^{38}Ca

5.1 Introduction

The reduced electric quadrupole transition probability or $B(E2)$ strength between the 0^+ ground state and the first 2^+ excited state in even-even nuclei is an important quantity that provides information on nuclear structure. Background on electromagnetic transitions is found in Section 1.3.3. The $B(E2)$ is a probe of collectivity which has been observed for a wide range of even-even nuclei with 0^+ ground states and low lying 2^+ excited states. Pushing this probe towards the drip lines can be interesting as trends in the $B(E2)$ values across an isotopic or isotonic chain have been used to probe the breakdown of magic numbers. As one removes protons from ^{40}Ca, the $N = 20$ magic number is known to disappear at ^{32}Mg, the center of a so-called "island of inversion". Here, neutron intruder pf-shell orbitals are strongly occupied in the ground state (see Ref. [101] and references within). The mirror of ^{32}Mg is ^{32}Ca, a nuclide well beyond the proton drip line and difficult (perhaps impossible) to study. Currently, ^{36,38}Ca are the lightest even-even Ca isotopes that can provide crucial evidence for the evolution of the $Z = 20$ shell towards the proton drip line through measured

$B(E2)$ strengths.

In explaining the nuclear charge radii of calcium isotopes within the shell model, Caurier *et al.* [16] argued that even near ^{40}Ca, the $Z = 20$ and $N = 20$ shell closures were weakened with substantial occupancy of both neutron and proton pf shells in the ground state. The interaction obtained, now referred to as ZBM2, has been used to calculate charge radii, for both ground and isomeric states, and to compare to the available data in this mass region [102, 103]. Other recent studies have employed shell-model interactions which predict very little proton pf occupancy in the ground state. One example is the work of Lalanne *et al.* [98] in which an estimated $B(E2)$ value is used for ^{36}Ca to evaluate the $^{35}\mathrm{K}(p,\gamma)^{36}\mathrm{Ca}$ reaction rate, a rate of significance for type I X-ray burst calculations.

The recent measurement of the charge radii of ^{36,38}Ca were interpreted with nuclear density functional theory by Miller *et al.* [104]. They indicate that the charge radius is strongly impacted by nuclear superfluidity and the weakly-bound nature of the protons. For ^{36}Ca, the proton $f_{7/2}$ level was predicted to be located above the Coulomb barrier, indicating properties of the nuclei would be strongly affected by the proton continuum. In these calculations the proton pf-shell occupancy for $^{36}\mathrm{Ca}_{g.s.}$ is about 13%.

To the extent that the $Z = 20$ shell closure is complete, the $B(E2)$ strengths for ^{36,38}Ca should be very small as the 2^+ states would be neutron excitations. Any ground-state proton pf occupancy would greatly inflate the $B(E2)$ value and thus this quantity is very sensitive to the extent of the $Z = 20$ shell closure. This chapter analyzes the $B(E2, 0_1^+ \rightarrow 2_1^+)$ strength for ^{36}Ca. The measurement of the de-excitation γ rays following intermediate-energy Coulomb excitation was performed and discussed in [105], but to account for the competing proton decay branch, and thus deduce the total Coulomb-excitation cross section, the p/γ branching ratio from Chapter 4 is used.

An additional motivation in this analysis of the $B(E2)$ strength of ^{36}Ca comes from the

proposal of Brown to use the difference in a mirror pair's rms charge radii to determine L, the density dependence of the symmetry energy [106, 107]. In order to deduce L, it is essential to correct for any difference in the deformations of the mirror pair due to the calculations being based on a spherical model space [108]. The $B(E2)$ strength is a metric linked to collectivity and deformation of the nucleus. The inferred deformation can be used to correct the rms charge radii of mirror pairs for any collectivity difference. To perform this correction, the rms charge radii and the $B(E2)$ values for both members of the pair must be known. With the recent hyperfine spectrum measurements by Miller *et al.* [104] that deduced the rms charge radius of ^{36}Ca, only the $B(E2)$ for ^{36}Ca remained undetermined to employ this logic for the ^{36}Ca - ^{36}S pair.

The $B(E2)$ strength is also intrinsically linked to the γ-ray partial width that, when combined with the proton partial width, can be used to look at astrophysical (p,γ) capture rates. The γ-ray and proton partial widths impact the rp-process through the ^{35}K$(p,\gamma)^{36}$Ca reaction rate. The proton branch returns flux to ^{35}K, and to the ^{34}Ar$(p,\gamma)^{35}$K - ^{35}K$(\gamma, p)^{34}$Ar equilibrium. The (p,γ)-(γ,p) equilibrium creates a waiting point in the rp-process which is escaped through resonance capture to the 2^+ state in ^{36}Ca and, via the γ branch and subsequent β decay, populating ^{36}K.

Simulations of the *rp*-process determined that the ^{35}K$(p,\gamma)^{36}$Ca reaction was an important component to the shape of X-ray-burst light curves [109]. This reaction is dominated by resonant capture through the 2^+ state in ^{36}Ca and the predicted light curves were found to be sensitive to large changes in this resonance capture rate. This is a case where reducing the nuclear data uncertainties impacts the interpretation of expected astrophysical observations.

5.2 Coulomb excitation of ^{36,38}Ca with γ-ray spectroscopy

Intermediate-energy Coulomb excitation has been shown to successfully assess the low-lying states with quadrupole or octupole collectivity in rare isotopes that are available as beams of fast ions [110]. Within this experimental scheme, rare isotopes at velocities exceeding 30% of the speed of light are scattered off stable high-Z targets and are detected in coincidence with the de-excitation γ rays that tag and quantify the inelastic process [111, 112]. While beam energies in classical Coulomb excitation reactions are below the Coulomb barrier to prevent nuclear contributions to the excitation process, peripheral collisions corresponding to large minimum impact parameters must be selected in the regime of intermediate-energy Coulomb scattering to exclude nuclear contributions. Coulomb excitation cross sections for a given multipole transition, $\sigma_{\pi\lambda}$, are integrated out to a maximum scatting angle and then translated into $B(E2)$ values using the Alder-Winther model of intermediate-energy Coulomb excitation [113]. The relationship between cross section and the $B(\pi\lambda, 0 \rightarrow \lambda)$ is given by,

$$\sigma_{\pi\lambda} \approx \left(\frac{Z_{pro}e^2}{\hbar c}\right)^2 \frac{\pi}{e^2 b_{min}^{2\lambda-2}} B(\pi\lambda, 0 \rightarrow \lambda) \begin{cases} (\lambda-1)^{-1} & \text{for } \lambda \geq 2 \\ 2\ln\left(b_a/b_{min}\right) & \text{for } \lambda = 1\,, \end{cases} \tag{5.1}$$

where b_{min} is the minimum impact parameter in the experiment and b_a is the impact parameter found in Ref. [111].

In a companion experiment to the one presented in this dissertation, ^{36}Ca was impinged on a Au target and through the technique of Intermediate-energy Coulomb excitation, γ decays for the 2^+ state in ^{36}Ca were measured [105]. This experiment was blind to the

proton decay branch, so to get a cross section for excitation, the branching ratio measured in Chapter 4 was applied as a correction to the observed number of gamma decays. This cross section was used in Eq. (5.1) to determine the resulting $B(E2, 0^+ \rightarrow 2_1^+)$ for ^{36}Ca which was found to be 131(20) e^2 fm^4. The table, from Ref. [105], is reproduced in Table 5.1 to summarize the results for the measured $B(E2)$ values.

Tab. 5.1: Cross sections and $B(E2\uparrow)$ values for the projectile (p) and target (Au) excitations. The cross sections are integrated from 0 to a maximum scattering angle of $\theta_{max}^{lab} = 55$ mrad for the ^{38}Ca, ^{36}Ca, ^{34}Ar, and ^{37}K projectiles at 62.6, 70.5, 64.3, and 59.8 MeV/nucleon mid-target beam energies, respectively. The cross section for the excitation of the proton-unbound 2_1^+ state in ^{36}Ca was corrected for the proton branch reported in this work. The $B(E2\uparrow)$ for the beam contaminant ^{34}Ar was determined as well and found to agree with the literature value of 220(30) e^2fm^4 [114] within two sigma.

proj	$E(2_1^+)$ (keV)	σ_I^p (mb)	$B(E2\uparrow$; proj) (e^2fm^4)	σ_I^{Au} (mb)	$B(E2\uparrow$; Au) (e^2fm^4)
^{38}Ca	2213(2)	17.5(19)	101(11)	49.5(18)	4570(170)
^{36}Ca	3049(3)	22.4(34)	131(20)	52.8(30)	4820(280)
^{34}Ar	2091(2)	52.1(29)	293(16)	44.2(16)	4960(180)
^{37}K	-	-	-	45.2(32)	4620(330)

5.3 Shell-model calculations of $B(E2\uparrow)$ and Γ_p

The following analysis considers the $B(E2)$ values for ^{36,38}Ca and the corresponding mirror nuclei's transition probabilities from Ref. [115]. The experimental and theoretical $B(E2)$ values are given in Table 5.2 and are compared in Fig. 5.1. The calculated values are from the ZBM2 Hamiltonian in the $(0d_{3/2}, 1s_{1/2}, 0f_{7/2}, 1p_{3/2})$ shell-model space [16], the USDB Hamiltonian in the *sd* model space [14], and based on the sdpfu-mix plus Coulomb interaction

in the $sd-pf$ model space where zero or two protons are allowed to be excited from sd to pf orbitals [116].

Tab. 5.2: Comparison of $B(E2;0^+ \rightarrow 2_1^+)$ values between experiment and theory. The ZBM2 and USDB results use effective charges of e_p=1.36 and e_n=0.45. The sdpfu-mix result [116] uses e_p=1.31 and e_n=0.46.

	$B(E2\uparrow)$ (e^2fm^4)			
	exp	ZBM2 [16]	USDB [14]	sdpfu-mix [116]
^{36}Ca	131(20)	179	11.8	23.5
^{36}S	89(9)	116	108	98
^{38}Ca	101(11)	110	14.0	-
^{38}Ar	125(4)	179	128	-

The wavefunctions in the ZBM2 model space can be decomposed into components labeled by $F_q(N_q)$ where F_q is the fraction of the q=proton/neutron part of the wavefunction that contains N_q protons/neutrons excited from $(0d_{3/2}, 1s_{1/2})$ to $(0f_{7/2}, 1p_{3/2})$. For the sd model space $F_n(0) = F_p(0) = 1$ is always true as there is no pf shell included. For the ZBM2 Hamiltonian, the ^{36}Ca ground-state has $F_n(0)(^{36}\text{Ca})= 0.91$, with the largest proton components at $F_p(0)(^{36}\text{Ca})= 0.55$ and $F_p(2)(^{36}\text{Ca})= 0.32$. For the $sd-pf$ wavefunction of [116], the ^{36}Ca ground state has $F_n(0)(^{36}\text{Ca})= 1$ and $F_p(0)(^{36}\text{Ca})= 0.92$ [96]. As a result of the ZBM2 model assuming isospin symmetry, the ^{36}S ground state occupations are the same as ^{36}Ca with the protons and neutrons interchanged.

Figure 5.1(a) and (b) shows the $B(E2)$ vs $F_p(0)$ correlation for ^{36}Ca and $F_n(0)$ for ^{36}S respectively. Figure 5.1(c) and (d) shows the same plots for the ^{38}Ca, ^{38}Ar pair. The red circles represent the sd model space in which $F_n(0) = F_p(0) = 1$ is fixed. The red crosses, present only for ^{36}Ca and ^{36}S, are based on the $sd-pf$ calculations from the sdpfu-mix interaction where there is a small increase in the pf shell population in the ground state.

The black point shows the results from the ZBM2 interaction where the line shows the ZBM2 interaction calculated with different $(0d_{3/2}, 1s_{1/2}) - (0f_{7/2}, 1p_{3/2})$ energy gaps. The green crosses indicate an 250 keV increase in the gap for the ZBM2gap interaction [117]. This ad hoc modification on the shell gap is useful to show the relationship between population in pf shell and the resulting B(E2) value.

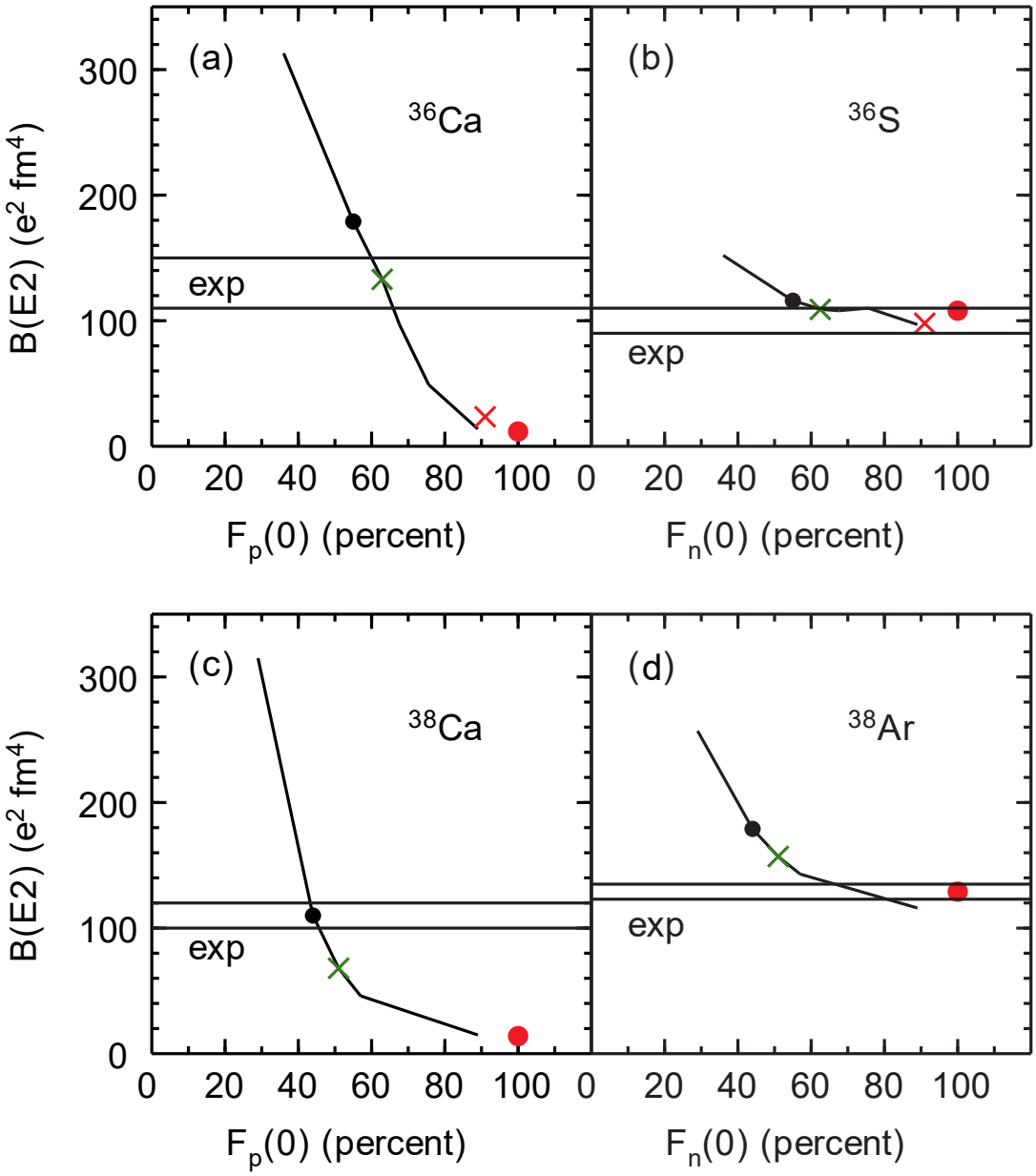

Fig. 5.1: $B(E2)$ values plotted vs $F_p(0)$ percent for (a) ^{36}Ca and its mirror (b)^{36}S as well as for (c) ^{38}Ca and its mirror (d) ^{38}Ar. As $F_q(0)$ decreases, you increase occupation into the pf-shell. The red circles are based on the sd shell calculations with the USDB Hamiltonian [14]. The red crosses are based on the $sd-pf$ calculations from the sdpfu-mix interaction [116] with the the $B(E2)$ and F values given in [96]. The black point is from the ZBM2 model space calculations with the lines using different sd-pf shell gaps. The green crosses indicates the ZBM2 with a 250 keV increase in the gap.

The $B(E2)$ values for ^{36}S are not very sensitive to the decreasing fractional occupation of neutrons in the *sd*-shell because $F_p(0)(^{36}\mathrm{S}) \geq 0.88$. In contrast, the $B(E2)$ for ^{36}Ca are very sensitive to $F_p(0)(^{36}\mathrm{Ca})$. Modifications to the ZBM2 interaction where the energy gap between the *sd* and *pf* shell were artificially increased or decreased gave different fractional occupations. For a small energy gap, the $B(E2)$ shoots up (about 500 e^2 fm^4) while $F_p(0)(^{36}\mathrm{Ca}) = 0$ and $F_p(2)(^{36}\mathrm{Ca})$ dominates the occupation. The opposite is also true where a large energy gap gives a smaller $B(E2)$ (11 e^2 fm^4) while $F_p(0)(^{36}\mathrm{Ca}) = 1$.

For ^{36}Ca, the experimental $B(E2)$ is a factor of 10 larger than that obtained in the *sd* model space. With the results shown in Fig. 5.1(a), we deduce that the ZBM2 interaction better reproduces the experimental $B(E2)$ values with $F_p(0)(^{36}\mathrm{Ca}) = 0.55(5)$ than the *sd* model-space result ($F_p(0)(^{36}\mathrm{Ca}) = 1$), and the $sd - pf$ calculations ($F_p(0)(^{36}\mathrm{Ca}) = 0.92$) obtained from Ref. [116, 96]. This points to ^{36}Ca having increased proton pf-shell occupancy compared to the expected $Z = 20$ closed shell. The results for ^{38}Ca are similar to those for ^{36}Ca. For ^{38}Ca, the experimental $B(E2)$ value is a factor of 7 larger than that obtained in the *sd* model space. This similarly indicates a large pf-shell occupancy in the ground state.

We note that independent of the effective charges assumed, the $B(E2)$ values for the sets ^{36}Ca and ^{38}Ar and for ^{38}Ca and ^{36}S are similar with the ZBM2 interaction as the calculated E2 transition amplitudes for protons and neutrons are similar within these pairs. This similarity of $B(E2)$ values within these pairs is confirmed experimentally (Table 5.2).

From the experimental partial-γ-decay width, Γ_γ (a value directly related to the $B(E2)$ calculated using Eq. (5.5) discussed later), and the measured branching ratio, the partial-proton-decay width, Γ_p, can be calculated as these quantities are related through the expression,

$$B_p = \frac{1}{1 + \Gamma_\gamma / \Gamma_p} \,. \tag{5.2}$$

The resulting partial-proton-decay width of ^{36}Ca is Γ_p=0.53(9) meV. Theoretically this decay width is calculated from the shell-model spectroscopic factor times the single-particle decay width. For the latter we use the same value as in Ref. [98]. Spectroscopic factors for the three shell-model calculations are listed in Table 5.3 and resultant partial widths are also given. Of the three shell-model calculations, only the ZBM2 result is consistent with the experimental Γ_p value. Thus the ZBM2 calculation is clearly superior in that it is the only one that reproduces both Γ_γ and Γ_p.

Tab. 5.3: Predicted spectroscopic factors $C^2S_{1/2}$ for the emission of an $s_{1/2}$ proton from the 2^+ state in ^{36}Ca and the corresponding proton partial decay widths calculated with various interactions.

	exp	ZBM2 [16]	sd [14]	$sd-pf$ [116]
$C^2S_{1/2}$	0.0057(10)	0.0056	0.009	0.009
Γ_p (meV)	0.53(9)	0.52	0.87	0.84

Figure 5.2 shows trends in both the excitation energies of 2_1^+ states and the $B(E2\uparrow)$ values across the Ca isotopes. The mid-neutron shell around ^{44}Ca shows a sharp increase in $B(E2)$ values relative to the value for ^{40}Ca while the measured $B(E2)$ values of ^{36,38}Ca are larger than predicted by the *sd* calculations where the trend was expected to dip towards low $B(E2)$ values. Predictions with the ZBM2 interaction give a good overall agreement with both E(2^+) and the $B(E2)$ isotopic trends but consistently overpredicts the $B(E2)$ values. Other shell model interactions, including the GXPF1A (using e_p=1.5 and e_n=0.5) [118], included for $A = 42-50$, have agreement with the E(2^+), but are unable to reconstruct the trend in $B(E2)$ values. The GXPF1A interaction only models neutron occupancy into the pf shell and thus results in small $B(E2)$ values. This shows that $B(E2)$ values between neutron closed shells $N = 20, 28$ are sensitive to the degree of $Z = 20$ shell closure and supports

the argument for an incomplete $Z = 20$ shell closure. Similarly, the USDB Hamiltonian models neutron occupancy in the *sd* shell and excludes proton excitations resulting in under predicted $B(E2)$ values in ^{36,38}Ca.

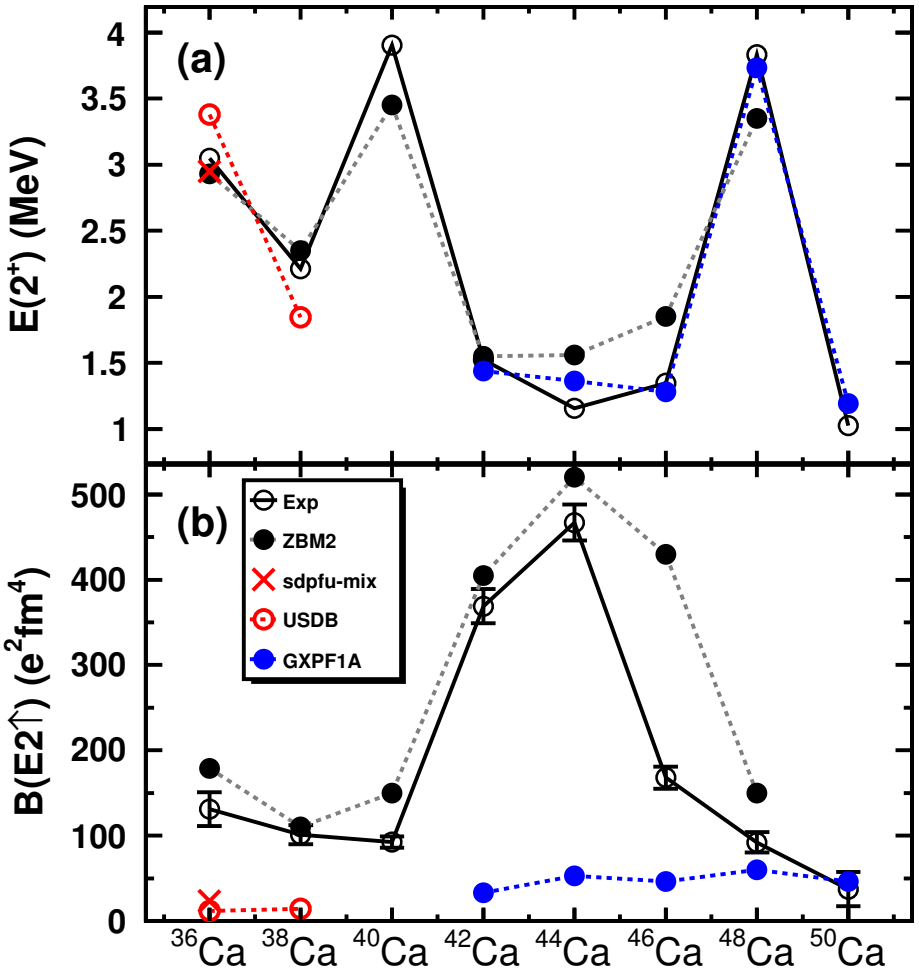

Fig. 5.2: Comparison of experimental and predicted trends in (a) 2_1^+ excitation energy and (b) $B(E2\uparrow)$ values across the Ca isotopes.

The strong occupancy of the pf-shell is at odds with the recent nuclear density functional calculations of the charge radius of ^{36}Ca [104]. The occupation probability of this shell

for the ground state is approximately 13% and as we expect this occupancy is from $(pf)^2$ configurations, then $F_p(0) \approx 0.94$. This value is much closer to the results of the USDB and sdpfu-mix shell-model calculations and thus it seems this model would not explain the observed $B(E2)$ value.

The ZBM2 model has also found success in Ref. [117] calculating the 2-neutron knockout cross section of ^{38}Ca . This knockout reaction from ^{38}Ca to ^{36}Ca was found to be sensitive to the single-particle configurations of the removed neutrons. The measured inclusive cross section populating any state in ^{36}Ca and the ratio of measured exclusive cross sections between the 2_1^+ and both 0^+ states (the $0^+_{g.s.}$ and 0_2^+) were reproduced only with the two-nucleon amplitudes from the ZBM2 effective interaction. Here, increasing the shell gap in the ZBM2 model by 250 keV (dubbed the ZBM2gap interaction) better reproduced the ratio between the 2_1^+ and 0^+ cross sections. The results of ZBM2gap for $B(E2)$ values are marked as green crosses in Fig. 5.1. These calculations do a better job reproducing the measured $B(E2)$ values for all nuclei except ^{38}Ca. This agrees with the conclusion in Ref. [117] that the increased shell gap between the sd and pf shells would be important for a shell-model effective interaction local to neutron-deficient Ca isotopes.

It is conceivable that evidence for the high occupancy of the proton pf-shell could be obtained from proton removal reactions. For ^{40}Ca, spectroscopic factors for the removal of $\ell = 0, 1, 2, 3$ protons have been extracted from measurements of the $(d,^3\mathrm{He})$ and the $(e,e'p)$ reactions [119, 120]. The extracted spectroscopic factors are compared to the ZBM2 results in Table 5.4. This comparison shows the ZBM2 over-predicts protons occupying the $f_{7/2}$ shell and to a lesser extent the the $p_{3/2}$ shell. The spectroscopic factors from the $(e,e'p)$ data have been reanalyzed within the dispersive optical model to give spectroscopic factors of 2.84(16) and 1.20(6) for the $d_{3/2}$ and $s_{1/2}$ states respectively which do more closely match the ZBM2 predictions [121]. The cross section for proton removal from the $^{36}\mathrm{Ca}_{g.s.}$ to the $3/2^-$ and $7/2^-$

states in ^{35}K would be of interest. Presently only proton and neutron knockout reactions from $^{36}\mathrm{Ca}_{g.s.}$ to $^{35}\mathrm{K}_{g.s.}$ and $^{35}\mathrm{Ca}_{g.s.}$, respectively, have been studied experimentally [122] but the predicted spectroscopic factors for these cases only decrease by 10-20% with the ZBM2 interaction compared to the *sd* calculations and thus these cross sections are rather insensitive to the extent of pf occupancy.

Tab. 5.4: Evaluated proton removal spectroscopic factors from the ^{40}Ca(d,^{3}He)^{39}K reaction [119] and the ^{40}Ca(e,$e'p$)^{39}K reaction to different levels in ^{39}K compared with predicted spectroscopic factors from the ZBM2 for ^{40}Ca.

			C^2S		
E_x (keV)	J^π	ℓ	(d,^{3}He) [119]	(e,e'p) [120]	ZBM2
0	$d_{3/2}$	2	2.20	2.58(26)	2.92
2520	$s_{1/2}$	0	1.66	1.02(10)	1.48
2815	$f_{7/2}$	3	0.32	0.38(4)	0.77
3020	$p_{3/2}$	1	0.05	0.010(2)	0.08

It is interesting to consider the consequences of the incomplete $Z = 20$ shell closure for the neighboring even-even nucleus ^{34}Ca which has yet to be observed. This nuclide is of interest as it potentially has a bubble structure [123], is possibly a double-magic nucleus [124, 125], and is a candidate for a two-proton ground-state emitter [126, 127, 128]. Most calculations of the nuclear structure and $2p$ decay of ^{34}Ca consider only valence protons in the *sd* shell. With the possibility of both negative and positive parity orbits contributing, then interference effects could lead to a strong diproton configuration for the unbound protons [129, 130, 131]. From the ZBM2 Hamiltonian, the two-nucleon amplitudes for removal of two protons from $^{34}\mathrm{Ca}_{g.s.}$ to $^{32}\mathrm{Ar}_{g.s.}$ are 0.912 for $(d_{3/2})^2$, 0.313 for $(s_{1/2})^2$, -0.713 for $(f_{7/2})^2$, and -0.224 for $(p_{3/2})^2$.

5.4 Difference in mirror charge Radii update for ^{36}Ca-^{36}S

In Ref. [107], the charge radius of ^{36}Ca was used to calculate $\Delta R_{ch} = R_{ch}(^{36}\text{Ca}) - R_{ch}(^{36}\text{S}) = 0.150(4)$ fm and deduce a value of of $L = 5 - 70$ MeV for the symmetry energy in the nuclear equation of state. The energy-density functional (EDF) and covariant-density functional (CODF) theory calculations that were used for the connection between ΔR_{ch} and L were based on spherical calculations in the *sd* model space. Deformation corrections to this type of calculation are outlined in [108] and Section 1.3.3 where the β_2 parameter of the Bohr shape parameterization is deduced from the experimental $B(E2)$ value. In [108], the ΔR_{ch} for $A = 54$ was corrected for the changed radii (implied by the β_2's) and applied to deduce a value for L.

Using the present results for ^{36}Ca of $B(E2\uparrow) = 131(20)$ e^2 fm^4, the deformation correction gives $\beta_2(^{36}\text{Ca}) = 0.139$ and $\delta R_{ch}(^{36}\text{Ca}) = 0.012(2)$ fm. For ^{36}S with the experimental $B(E2)$ = 89(9) e^2 fm^4 [115], we obtain $\beta_2(^{36}\text{S}) = 0.143$ and $\delta R_{ch}(^{36}\text{S}) = 0.013(2)$ fm. Thus one should add $\delta R_{ch}(^{36}\text{Ca}) - \delta R_{ch}(^{36}\text{S}) = -0.001(3)$ fm to the results of the spherical calculations. We conclude that the deformation correction to the $A = 36$ mirror radius difference is small and inconsequential compared to the large uncertainty in deducing L.

The single-particle energies for the pf protons for ^{36}Ca are in the continuum (unbound), but the pf separation energies in the correlated ground-state wavefunction of ^{36}Ca are positive (e.g., effectively bound). The DFT and CODF calculations used in Ref. [107] assumed a $Z = 20$ closed shell for ^{36}Ca. An extension of the calculations used in Ref. [107] to include the pf orbitals needs to be developed. In Ref. [132], β_2 corrections to the rms radii are not included. Rather, the odd-even oscillations in the rms charge radii are obtained from the addition of a pairing term in the Fayans EDF functional [133]. This difference leads to a

decrease in the correlation between ΔR_{ch} and L observed in Ref. [132] which casts doubt oon the logic for extracting L from mirror charge radii.

5.5 ^{35}K$(p,\gamma)^{36}$Ca reaction rate update

The astrophysical capture reaction rate through a narrow resonance can be evaluated at the resonance energy E_r to give [134],

$$\langle \sigma v \rangle = \left(\frac{2\pi}{\mu k_B T} \right)^{3/2} \hbar^2 \, (\omega\gamma) \, e^{-E_r/k_B T}, \tag{5.3}$$

where μ is the reduced mass, $k_B T$ is the Boltzmann constant times the temperature in Kelvin, and $(\omega\gamma)$ is the resonance strength. The resonance strength for the ^{35}K$(p,\gamma)^{36}$Ca reaction can be expressed in terms of the spins and partial widths Γ_i to give,

$$(\omega\gamma) = \frac{2J_i + 1}{(2J_p + 1)(2J_{35K} + 1)} \frac{\Gamma_{\gamma,i}\Gamma_{p,i}}{\Gamma_{\gamma,i} + \Gamma_{p,i}}. \tag{5.4}$$

With the 2^+ state being the resonance of interest, we have $J_i = 2$, $J_p = 1/2$, and $J_{35K} = 3/2$. The energy of this resonance is determined, to high accuracy, to be $E_r = 0.449(6)$ MeV [98]. Only the partial widths make significant contributions to the uncertainty on the reaction rate. The 1^+ and 2_2^+ states in ^{36}Ca, first measured at GANIL [98] and also observed here, can also contribute to the reaction rate but are not significantly populated within the 0.5-2 GK temperature range of an X-ray burst.

The reduced electric transition probability for a transition can be related to the gamma-decay partial width using Eq. (1.22) and the relation between decay rates and decay widths

to give,

$$\Gamma_\gamma(E\lambda) = \frac{8\pi(\lambda+1)}{\lambda[(2\lambda+1)!!]^2}\left(\frac{E_\gamma}{\hbar c}\right)^{2\lambda+1} B(E\lambda). \tag{5.5}$$

A $B(E2,\, 0_1^+ \rightarrow 2_1^+) = 131(20)\ e^2\mathrm{fm}^4$ or $B(E2,\, 2_1^+ \rightarrow 0_1^+) = 26.2(40)\ e^2\mathrm{fm}^4$ in combination with $E_\gamma = 3.049(3)$ MeV results in $\Gamma_\gamma = 5.6(8)$ meV.

These values are used here in an update to the results by Lalanne [98]. The latter used the $sd-pf$ configuration space to calculate the $B(E2)$ strength, with an assumed 50% uncertainty, and the branching ratio they measured. The parameters relevant for the 2^+ state from the present work and those from the GANIL study are given in Table 5.5. In the present study we measured both the proton decay branch and the $B(E2)$. Our rate is a factor of 3 larger than that of [98] in the astrophysical region (0.5-2 GK) and has a smaller uncertainty based entirely on experiment. The details of the input for the new reaction rate are given in Table 5.6.

The reaction rate is plotted in Fig. 5.3 along with the ratio of the present rate to the GANIL results. The recommended results of the GANIL study were ≈10% smaller than those of Iliadis *et al.* [135] in the 0.5 to 2 GK range. The latter were used as the default in the sensitivity study of Cyburt *et al.* [109]. In this sensitivity study, increases in the rate by a factor of 100 caused significant modifications in the predicted X-ray burst light curve. As our results imply an increased rate by only a factor of three, the conclusion of the GANIL study, that the $^{35}\mathrm{K}(p,\gamma)^{36}\mathrm{Ca}$ reaction does not affect the shape of the X-ray bust light curve, stands.

5.6 Conclusion

The measurement for the $B(E2,\, 0_1^+ \rightarrow 2_1^+)$ value of ^{36}Ca required a correction due to the 2^+ state being unbound to proton decay, requiring the proton branching ratio. This resulted

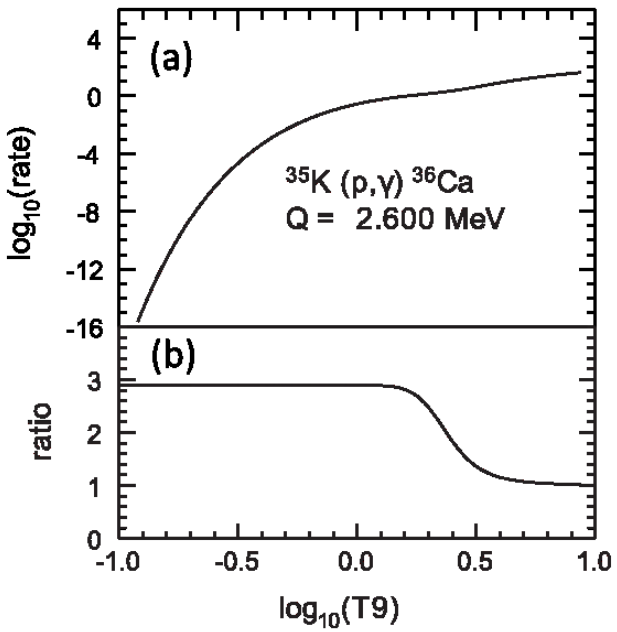

Fig. 5.3: (a) Present result for the ^{35}K(p,γ)^{36}Ca reaction rate. (b) Ratio of the present rate divided by the rate obtained in [98].

in a $B(E2)$ value of 131(20) e^2 fm^4. Here, the improved $B(E2)$ measurement for ^{38}Ca, determined to be 101(11) e^2 fm^4, was also used in the analysis. The $B(E2)$ value for ^{36}Ca was found to be a factor of 10 larger than predicted by the *sd* shell model and a factor of 5 larger than the $sd-pf$ shell model which is an indication of a collective excitation.

The present analysis shows that the ^{36}Ca ground-state wavefunction contains a significant amount of proton excitation from the *sd* to the pf shell. The single-particle energies for the pf protons for ^{36}Ca are in the continuum (unbound), but the pf separation energies in the correlated ground-state wavefunction of ^{36}Ca are positive (e.g., effectively bound). Hence, energy density and covariant density functionals containing correlations involving the pf orbitals need to be developed.

The measured $B(E2)$ value was used to account for deformation of the nucleus. Because the $B(E2)$ values in the ^{36}Ca/^{36}S mirror pair are similar in value, the correction almost

Tab. 5.5: Results for the contribution of the first 2^+ state of ^{36}Ca to the ^{35}K(p,γ)^{36}Ca reaction rate. Results from [98] and the present work are compared.

	GANIL [98]	Present work
B_p	0.165(10)	0.087(8)
$B(E2\downarrow)$ (e^2 fm^4)	4.7(2.3)	26.2(40)
Γ_γ (meV)	0.99(45)	5.6(8)
Γ_p (meV)	0.20	0.53(9)
Γ (meV)	1.19(60)	6.1(8)
$(\omega\gamma)$ (meV)	0.10(5)	0.30(7)

cancels out, leaving the difference in charge radii unaffected. This means that the previously reported result for the determination of L from the A=36 stands [107]. Our values for the $B(E2)$ and proton branching ratio have been used to update the ^{35}K$(p,\gamma)^{36}$Ca reaction rate. The rate is increased by a factor of 3 compared to the previous study [98] within the Gamow window of an X-ray burst. While the uncertainties are greatly reduced, the updated rates will not significantly modify the predicted X-ray burst light curves [109].

Tab. 5.6: Properties for the relevant rp-process resonance states of ^{36}Ca. Only the resonance strength for $J^\pi = 2^+$ is restrained from experiment while the higher energy resonances rely on shell-model calculations with the ZBM2 model [16] for the spectroscopic factors.

n	J^π	k	E^*(th)	E^*(exp)	E_{res}	C^2S	C^2S	Γ_γ	Γ_p	$\omega\gamma$
			(MeV)	(MeV)	(MeV)	$\ell = 0(1)$	$\ell = 2(3)$	(eV)	(eV)	(eV)
2	2^+	1	3.252	3.049	0.449	5.8×10^{-3}	2.3×10^{-6}	5.6×10^{-3}	5.3×10^{-4}	3.0×10^{-4}
3	1^+	1	5.098	4.270 [a]	1.670	2.4×10^{-3}	1.4×10^{-4}	9.5×10^{-2}	7.3×10^{1}	3.5×10^{-2}
4	2^+	2	4.639	4.730 [b]	2.130	6.8×10^{-4}	7.4×10^{-3}	3.3×10^{-2}	1.1×10^{2}	2.1×10^{-2}
5	0^+	3	4.924		2.324		6.6×10^{-2}	3.3×10^{-4}	5.4×10^{2}	4.1×10^{-5}
6	4^+	1	5.005		2.405			1.1×10^{-3}		
7	2^+	3	5.378		2.778	5.9×10^{-4}	6.9×10^{-3}	5.9×10^{-3}	3.9×10^{2}	3.7×10^{-3}

[a] This value has been updated in this work after the original publication to be E* = 4.199 MeV.
[b] This value has been updated in this work after the original publication to be E* = 4.51 MeV.

Chapter 6

Evolution of Shell Gaps in the Neutron-Poor Calcium Region from Invariant-Mass Spectroscopy of ^{37,38}Sc, ^{35}Ca, and ^{34}K

6.1 Introduction

As was discussed in Section 1.3.1, the magic numbers (2, 8, 20, 28, 50, 82, and 126) arise as a result of the shape of the attractive nuclear interaction and spin-orbit coupling creating energy gaps between shells for protons and neutrons [8]. Away from stability, the picture of shell closures changes as the classic shell gaps known at stability weaken and new subshell closures appear. The disappearance of the $N = 20$ closed shell is manifested in $^{32}_{12}\mathrm{Mg}_{20}$ by occupation of the $\nu 0f_{7/2}$ intruder orbit in the ground state. This effect leads to a region of the chart of nuclides called the island of inversion [112, 136]. At $Z = 14$ and $N = 20$, $^{34}_{14}\mathrm{Si}_{20}$ was shown to be doubly magic and potentially a proton bubble nucleus [137]. In the

oxygen isotopes, the $N = 16$ subshell closure is observed at $^{24}_{8}O_{16}$ [138] with a gap between the $\nu 1s_{1/2}$ and $\nu 0d_{3/2}$ orbits while the traditional $N = 20$ shell closure is not observed in $^{28}_{8}O_{20}$ [139]. These effects are driven by the monopole component of the nuclear interaction, which has central, tensor, two-body spin-orbit, and three-nucleon components [140, 141].

Mass measurements for neutron-rich calcium isotopes have provided evidence for shell closures at both $N = 32$ and $N = 34$ [142, 143]. For neutron-poor calcium isotopes, a subshell closure at $N = 16$ has also been suggested [144]. These claims arise from a large value for the change in neutron separation energy, ΔS_n. Also occurring in this region, the measurements from Chapter 5 are evidence for a weakening $Z = 20$ shell. This conclusion comes from the apparent need for cross-shell proton excitations to explain the measured B(E2↑) value and two-neutron removal cross sections for neutron-deficient ^{36}Ca and ^{38}Ca [105, 117]. The present work further illuminates the shell gaps in this region through mass measurements of proton unbound isotopes.

6.2 Methods

This was the same experiment discussed in Chapter 4 with further detail on the experimental set-up found in Section 2.2.2. At the NSCL, a primary beam of ^{40}Ca at 140-MeV/nucleon impinged on a Be target. With the A1900 fragment separator, a secondary beam of ^{37}Ca was produced at 72 MeVA with a purity of 40%. By gating on the ToF between the A1900 focal plane scintillator and S800 object scintillator, this work only considers reactions from ^{37}Ca projectiles. This beam impinged on a 0.5-mm-thick Be target resulting in the reactions shown in Fig. 6.1 including inelastic excitation of ^{37}Ca, knockout reactions to populate ^{35,36}Ca and ^{34}K, proton pickup to populate ^{38}Sc, and charge exchange to populate ^{37}Sc. The reaction products were detected with a setup including the CAESAR array [47], a Si-CsI(Tl) ΔE-E

Ring Telescope, a Scintillating-Fiber Array (SFA), and the S800 Spectrograph [52].

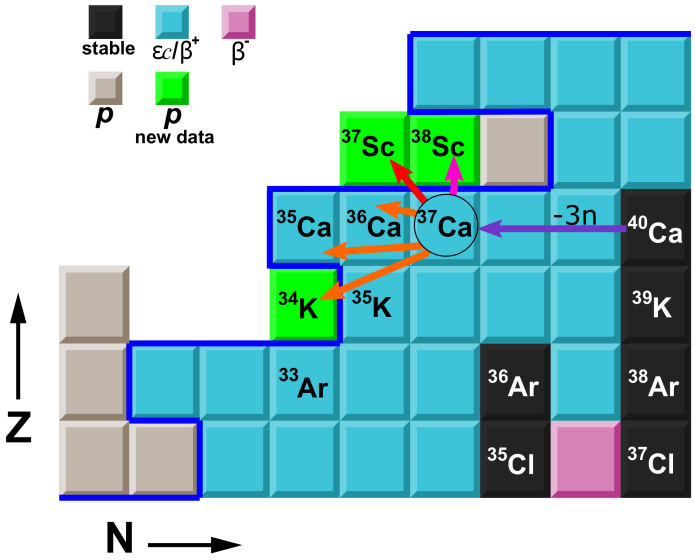

Fig. 6.1: Neutron-poor calcium region of the chart of nuclides with labels on unstable isotopes that are relevant to this work. Knockout reactions from the ^{37}Ca beam are shown in orange arrows, the charge exchange reaction to populate ^{37}Sc is shown by a red arrow, and the $1p$ pickup is shown by a pink arrow.

6.3 Invariant mass fits

Total decay-energy (E_T) spectra were measured using the invariant-mass method. The E_T spectra were typically fit with multiple peaks sitting upon a background. The peaks were assumed to have zero intrinsic decay width as most states were predicted with shell-model calculations (see later) to have intrinsic widths less than 1 keV while the experimental resolution is roughly two orders of magnitude larger. The lineshape due to the detector resolution and acceptance is calculated from Monte Carlo simulations and binned to match that of the experiment [77]. Figure 6.2(b) shows the results for the simulation with a uniform

decay energy, effectively showing the relative detection efficiency as a function of decay energy and decay angle of the heavy fragment relative to the beam axis (θ_H). The simulation matches the observed experimental efficiency compared in the distributions shown in Fig. 6.2(a) and (b). At E_T larger than 2 MeV, the simulated peak shape flattens as the efficiency drops for transverse decays (decay axis perpendicular to the beam axis) as such events miss the ring telescope and only longitudinal decays remain. This can be seen in Fig. 6.3 for the simulated resonance decays for two different decay energies of ^{38}Sc. The lineshape observed in Fig. 6.3(a) has good decay-energy resolution for transverse decays that have $-0.3 < \cos(\theta_H) < 0.3$ because the invariant mass reconstruction depends mostly on the angle between the detected fragments. Conversely, longitudinal decays outside of that range have increasingly worse decay-energy resolution as the invariant mass depends primarily on the energy difference of the detected fragments [77, 145]. The lineshape that results from the higher energy state shown in Fig. 6.3(b) has a flat top because transverse decays are missing, leaving only the poor resolution longitudinal decays. Backgrounds for the ^{35}Ca, ^{37}Ca, and ^{34}K data were included via event mixing with the procedure developed previously for knockout reactions [146]. Backgrounds in the data for ^{37,38}Sc are discussed individually in the results section.

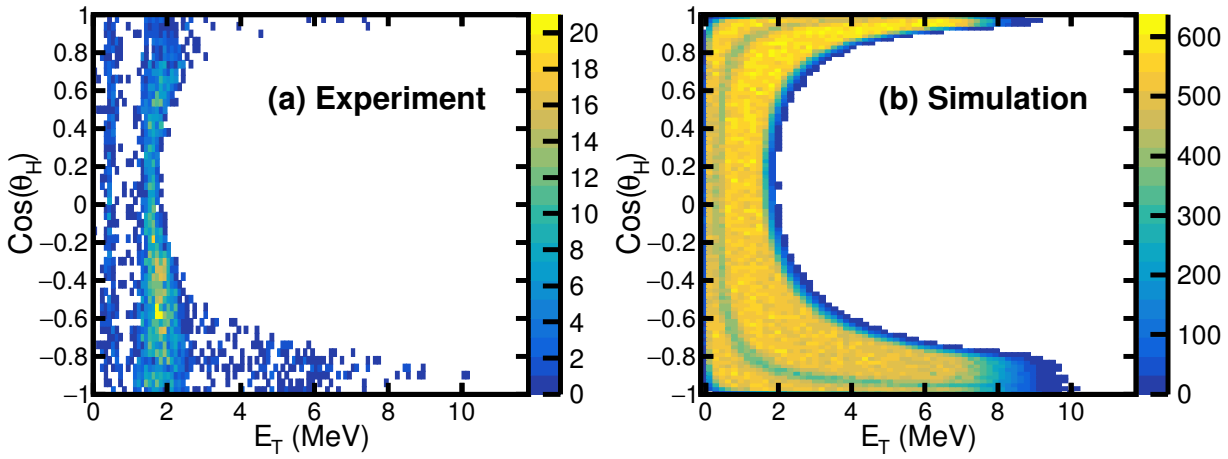

Fig. 6.2: (a) Decay angle of the heavy fragment relative to the beam axis vs the decay energy for the detected p+^{35}K fragments. (b) Simulation of a uniform decay energy to show which fragments hit the ring telescope, resulting in a plot of the relative efficiency. The simulation roughly matches the background distribution of detected fragments.

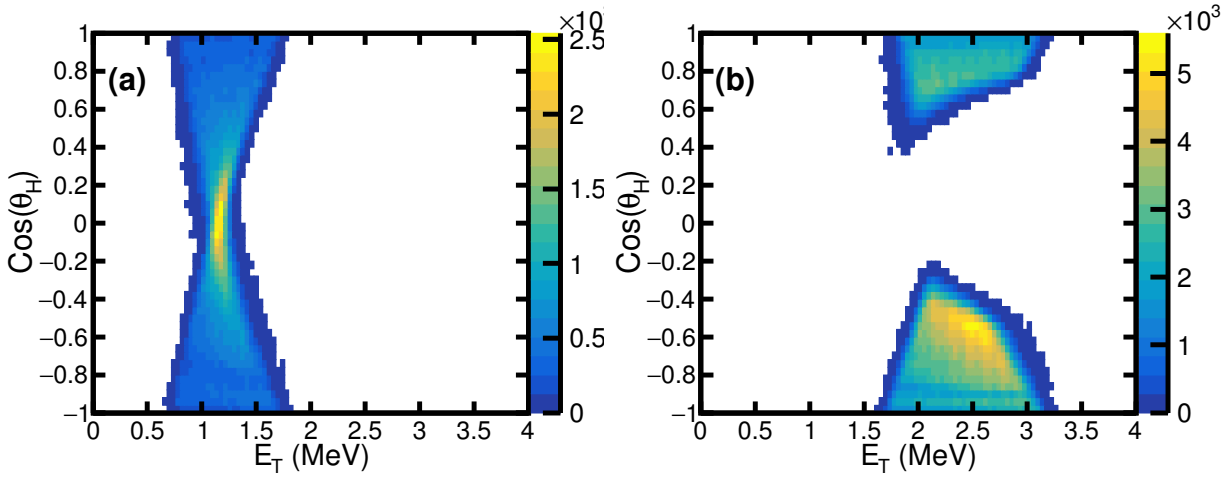

Fig. 6.3: Simulated decay distributions for (a) the E_T = 1.191 MeV resonance and (b) the E_T = 2.40 MeV resonance in ^{38}Sc. It is clear that at higher decay energies, transverse decays miss the ring telescope, resulting in poor energy resolution and an abnormal lineshape.

Our invariant-mass resolution for low decay energies was exemplified by two states studied previously, see Figs. 4.4 and 6.4 for ^{36}Ca and ^{37}Ca respectively. The 2^+ state in ^{36}Ca has been measured multiple times through in-beam gamma spectroscopy and the resulting weighted average excitation energy is E* = 3.0459(18) MeV [89, 147, 91, 105].[6] The value from the present study, see Fig. 4.4(a), is E* = 3.031 MeV with a 8 keV statistical uncertainty from the fit and a 5.6 keV uncertainty in the employed mass of ^{36}Ca [148]. The excitation of the $3/2^+$ state in ^{37}Ca has E* = 3.842(4) MeV determined by in-beam gamma spectroscopy [147]. We find this state at E* = 3.833 MeV with a 4 keV statistical uncertainty. Using these two states, we estimate the systematic uncertainty to be approximately 10 keV. For the overall uncertainties reported in this work we add this estimate in quadrature with the fitted statistical uncertainties.

6.4 Results for ^{35}Ca and ^{34}K

The ground state of ^{35}Ca is particle bound with a mass excess ΔM = 4777(105) keV [144]. The first excited state, predicted to be $J^\pi = 3/2^+$, is unbound to both $1p$ decay to ^{34}K and $2p$ decay to ^{33}Ar. Because ^{34}K is also unbound to proton emission, the first excited state of ^{35}Ca will only appear in the $2p$+^{33}Ar exit channel. The $2p$+^{33}Ar decay-energy spectrum is shown in Fig. 6.5 along with a fit to a single peak at E_T = 1.667(20) MeV. The region above 2 MeV is fit with an event mixing background but has a hint of a peak around 2.8 MeV which was not significant in the overall fit.

Data for the first observation of ^{34}K is presented in Fig. 6.6 showing the decay-energy spectrum for p+^{33}Ar events. The spectrum has two sharp resonances at E_T = 0.608(17) and

[6] Previously in Chapters 4 and 5, the energy of this state was assumed to be E*=3.049 MeV to stay consistent with the work in Ref. [105], where the energy was measured directly. Here, in an analysis separated from the direct energy measurement, I choose not to assume one measurement is correct and use the weighted average from a collection of similar measurements.

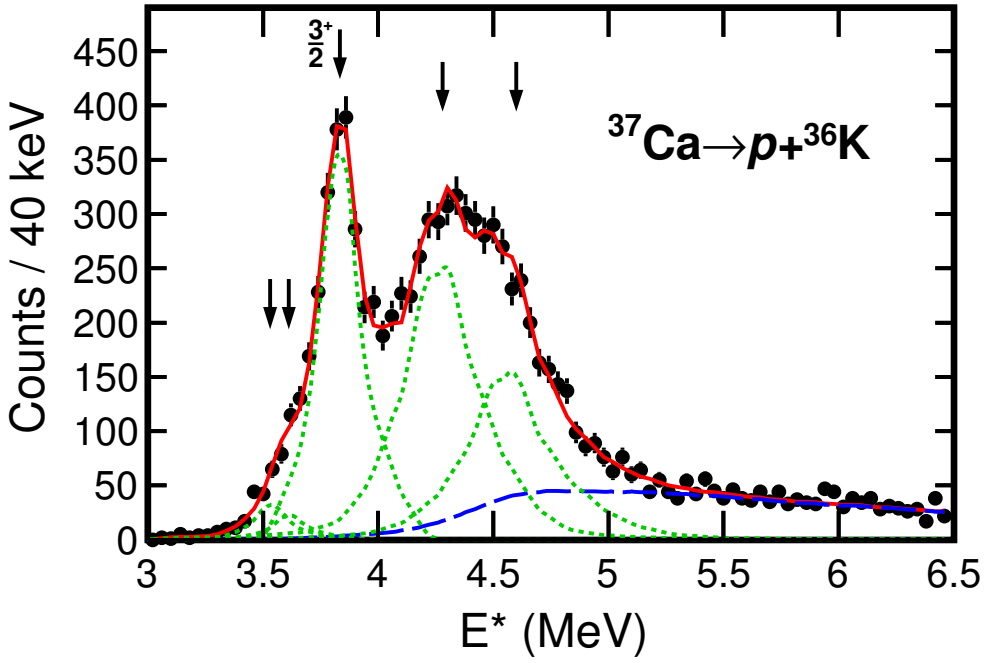

Fig. 6.4: Data points show the excitation-energy spectra of ^{37}Ca from p+^{36}K events. The red curve is from a fit with multiple peaks each shown by the green dotted curves. The blue-dashed line indicates the background for the ^{37}Ca fit. Arrows indicate states included in the fit where the two states below the $3/2^+$ level are fixed to the energies of states found in the gamma-decay study in [147], and the states above the $3/2^+$ state have not been previously observed.

1.009(18) MeV. The latter corresponds to an excitation energy of E* = 0.401(25), presuming the lower-energy peak is the ground state. At low relative energies, there is possible contamination from ^{35}Ca decays where the first emitted proton is detected but the second is missed. Assuming sequential 2p-decay, the observed population of ^{35}Ca($3/2^+$) was used along with the simulated efficiencies for detecting the first but not the second proton, resulting in a very small contribution shown by the magenta dashed curve under the second peak.

Above a decay energy of 1.5 MeV, the spectrum could be fit with multiple levels, but a two peak fit offered the fewest number of states that could reasonably reproduce the

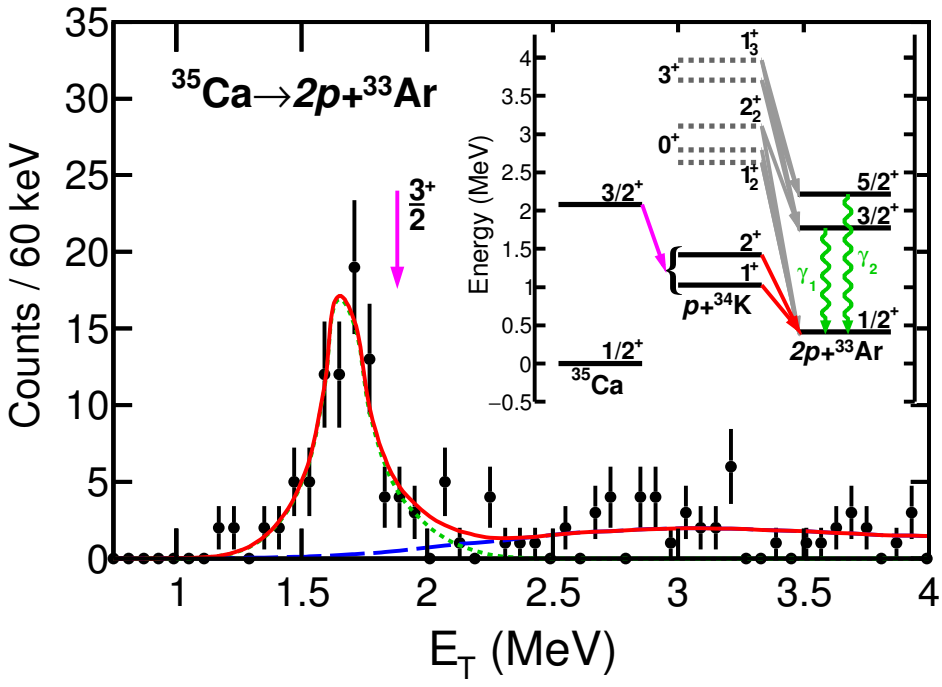

Fig. 6.5: Total decay-energy spectrum for the two-proton decay of ^{35}Ca with a single peak fit (line type and colors same as Fig. 6.4). The USDC shell-model decay energy for the $3/2^+$ state is shown by the magenta arrow. The insert shows the decay scheme for ^{35}Ca through ^{34}K with the magenta, red, and green arrows matching decays from states seen here and in Fig. 6.6.

data. The peaks at E_T = 1.85 MeV and 2.42 MeV sit on the large background determined though event mixing. For the background, the correlation function used to weight the mixed events in the procedure of [146] could not be uniquely determined in this experiment so the ^{3}He+^{8}B correlation from Ref. [146] was used instead. We decide to use this correlation function as compared to the proton emission correlations because the increased Coulomb potential between the ^{3}He and ^{8}B fragments better matches the large Coulomb potential between the p and ^{33}Ar decay fragments (with the other proton emissions discussed having approximately the same potential). This gives a better match for the end state correlations between fragments. A gate requiring $E_T > 1.36$ MeV was applied to look for gamma decays

in coincidence with p+^{33}Ar events. The result, shown as an insert in Fig. 6.6, indicates that the gamma-decaying J$^{\pi}$=3/2^{+} and J$^{\pi}$=5/2^{+} states in ^{33}Ar are populated after proton decay. This suggests, but does not prove due to the significant background, that the E$_T$ region above 1.36 MeV contains some highly excited states in ^{34}K that proton decay to gamma-decaying excited states in ^{33}Ar.

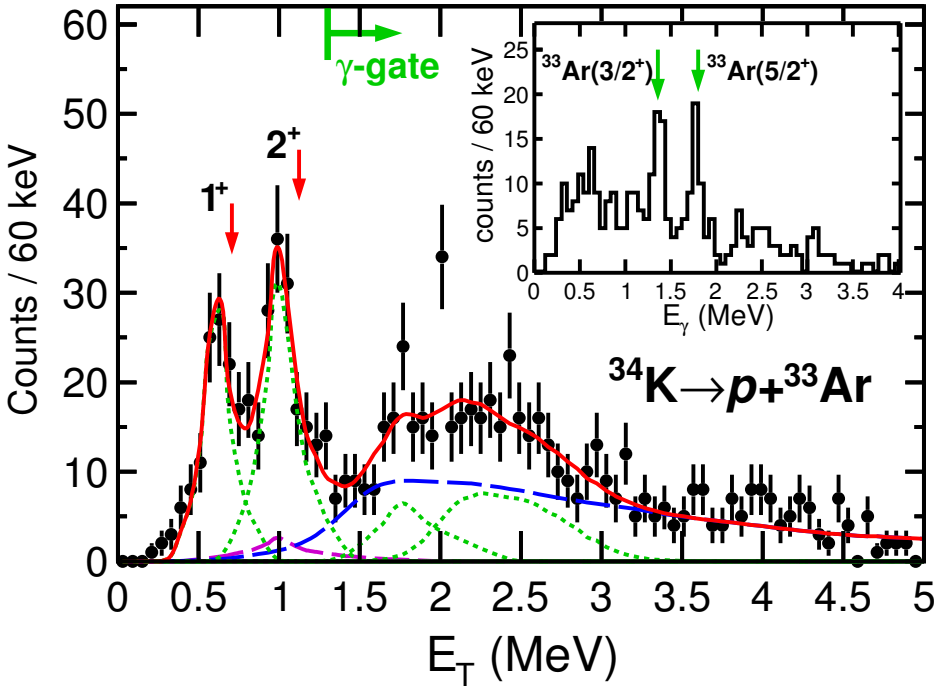

Fig. 6.6: Total decay-energy spectrum for ^{34}K fitted with 4 peaks (line colors same as Fig. 6.4). A small contribution from ^{35}Ca→2p+^{33}Ar events missing a proton is included (magenta dashed line). Red arrows indicate the predicted ground and first excited states from USDC shell-model calculations. The insert shows the gamma-ray energy spectrum in coincidence with p+^{33}Ar events having E$_T$ >1.36 MeV.

Shell-model calculations using the USDC Hamiltonian [15] were used to assign spins and parities of the states observed in ^{35}Ca and ^{34}K. The USDC Hamiltonian is the latest iteration of universal *sd* shell Hamiltonians that incorporate Coulomb and other isospin-breaking

interactions which can become important at and beyond the drip-line. A summary of the predicted transition energies and decay widths for ^{35}Ca and ^{34}K can be found in Table 6.1. Starting with ^{35}Ca, the magenta arrow in Fig. 6.5 indicates the predicted decay energy of E_T = 1.880 MeV coming from the combined Q values of the ^{35}Ca$(3/2^+) \rightarrow p+^{34}K(1^+)$ and ^{34}K$(1^+) \rightarrow p+^{33}Ar(1/2^+)$ transitions. This is 213 keV higher than observed, but this predicted value depends on the mass of ^{33}Ar, which is over-bound in the calculation by 277 keV compared to AME2020 [2]. This calculation predicts that the ^{35}Ca$(3/2^+)$ state proton decays primarily through the ^{34}K(1^+) ground state, a prediction that we do not have sufficient statistics to confirm.

The USDC calculations for ^{34}K again predict decay energies slightly higher than measured, E_T = 0.708 MeV (versus 0.608 MeV measured) for the 1^+ ground state and E_T = 1.123 MeV (versus 1.009 MeV measured) for the 2^+ first excited state, see red arrows in Fig. 6.6. The USDC calculations do accurately predict the excitation energy of the first excited state at E^* = 0.415 MeV compared to the measured value of 0.401(25) MeV. The spacing and order of the 1^+ and 2^+ states agree with what is observed in the mirror nucleus ^{34}P. The calculations also predict many states between 1.36 MeV and 3 MeV. Some states, like the 1^+_2 and 0^+, decay to the ground state of ^{33}Ar while others, like the 2^+_2, 3^+, and 1^+_3, have decay branches to excited states of ^{33}Ar. These predicted states and their decays are included as gray dotted lines and arrows in the decay scheme of Fig. 6.5 with energies included in Table 6.1. In addition to the predicted shell-model states, there are negative parity states starting at 2.3 MeV in ^{34}P which should also occur in ^{34}K but are not part of the USDC calculations. The present data cannot resolve these possible states.

Tab. 6.1: Transition energies and strengths in ^{35}Ca and ^{34}K predicted by shell-model calculations using the USD Hamiltonian [15].

Initial		final			
Iso(J^π)	E* (MeV)	Iso(J^π)	E* (MeV)	Qval	Γ_p (keV)
^{35}Ca($3/2^+$)	2.414	^{34}K(1^+)	0	1.172	0.015
^{35}Ca($3/2^+$)	2.414	^{34}K(2^+)	0.415	0.757	0.0003
^{35}Ca($5/2^+$)	4.917	^{34}K(1^+)	0	3.675	2.20
^{35}Ca($5/2^+$)	4.917	^{34}K(2^+)	0.415	3.260	12.8
^{34}K(1^+)	0	^{33}Ar($1/2^+$)	0	0.708	0.0006
^{34}K(2^+)	0.415	^{33}Ar($1/2^+$)	0	1.123	0.019
^{34}K(1^+_2)	1.607	^{33}Ar($1/2^+$)	0	2.315	17.7
^{34}K(1^+_2)	1.607	^{33}Ar($3/2^+$)	1.404	0.911	0.008
^{34}K(0^+)	1.767	^{33}Ar($1/2^+$)	0	2.475	28.0
^{34}K(0^+)	1.767	^{33}Ar($3/2^+$)	1.404	1.071	0.010
^{34}K(2^+_2)	2.083	^{33}Ar($1/2^+$)	0	2.791	0.082
^{34}K(2^+_2)	2.083	^{33}Ar($3/2^+$)	1.404	1.387	0.096
^{34}K(2^+_2)	2.083	^{33}Ar($5/2^+$)	1.992	0.799	0.0016
^{34}K(3^+)	2.684	^{33}Ar($1/2^+$)	0	3.392	0.22
^{34}K(3^+)	2.684	^{33}Ar($3/2^+$)	1.404	1.988	0.81
^{34}K(3^+)	2.684	^{33}Ar($5/2^+$)	1.992	1.400	0.055
^{34}K(1^+_3)	2.944	^{33}Ar($1/2^+$)	0	3.652	1.79
^{34}K(1^+_3)	2.944	^{33}Ar($3/2^+$)	1.404	2.248	13.6
^{34}K(1^+_3)	2.944	^{33}Ar($5/2^+$)	1.992	1.660	0.033

6.5 Results for ^{37}Sc and ^{38}Sc

Charge exchange reactions produced a small number of ^{37}Sc events observed to proton decay to ^{36}Ca. These data, shown in Fig. 6.7, were fit with either one or two peaks plus an extra wide peak at $E_T = 5$ MeV acting as a background. This is done because it cannot be assumed the background in data resulting from knockout will be the same for charge exchange and this allows the background to be constrained by fewer variables. The single peak fit, shown in Fig. 6.7(a), suggests $E_T = 3.00(5)$ MeV, but this fit misses the data points to either side of the peak. The fit is potentially remedied if the ground state has a large intrinsic width of $\sim$600 keV, but this is not supported by the shell-model predictions. The two peak fit, shown in Fig. 6.7(b), finds states at $E_T = 2.37(13)$ MeV and $E_T = 3.24(8)$ MeV.

The mirror nucleus, ^{37}S has a $7/2^-$ ground state with a $3/2^-$ state at 0.646 MeV [149]. In ^{37}Sc the Thomas-Ehrman shift of the $J^\pi = 3/2^-$ state (with a proton occupying the $\pi 1p_{3/2}$ orbital in a single-particle picture) will lower its energy. The Thomas-Ehrman shift observed for the $3/2^-$ excited states in ^{41}Sc and ^{41}Ca is 0.23 MeV. So a fit with two low-lying states in ^{37}Sc is expected. In addition there is a $3/2^+$ state at 1.398 MeV in ^{37}S which could account for a third peak around E_T=4.5 MeV in ^{37}Sc. The amount of data and the resolution are insufficient to make definitive statements. Nevertheless, this nuclide is observed and a ground-state mass estimate is obtained where the uncertainty encompasses the results from both fits (see Table 6.2).

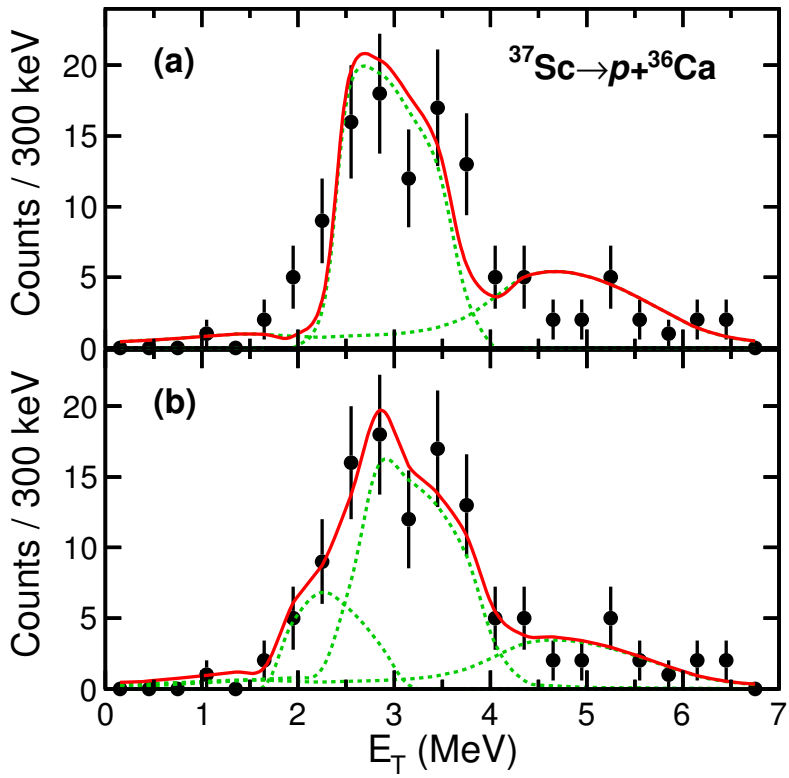

Fig. 6.7: Total decay-energy spectrum for ^{37}Sc. (a) Shows a one-peak fit while (b) shows a two-peak fit (line colors same as Fig. 6.4). The high-energy structure near 5 MeV is fit with a peak but is considered to be the background contribution.

Proton pickup reactions from the beam produced data which provided the first evidence for ^{38}Sc. Figure 6.8 shows the decay-energy spectrum for p+^{37}Ca events. The spectrum shows a resolved state (ground state) at E_T = 1.191(14) MeV. A second peak at E_T = 1.823(16) MeV (E* = 0.632(22) MeV) is well constrained from the sharp rise but at higher energy, blends into a region where the resolution declines. A third peak, at E_T = 2.40 MeV, is required for an acceptable fit, but is not well constrained. The background contribution is fit with an inverse Fermi function multiplied by a decreasing linear function to give the required smooth increase in background as the phase space increases and a long tail which is typically observed in IMS. It is also possible that the data has contributions from more

states such as those seen in the mirror ^{38}Cl. These states come from the $3/2^+$ ground state of ^{37}Ca (^{37}Cl) coupling with the $0f_{7/2}$ proton (neutron) to make $J^\pi = (2, 3, 4, 5)^-$. The 0.63 MeV spacing of the first two peaks in Fig. 6.8 is consistent with the spacing of 0.67 MeV between the 2^- ground state and the 5^- first excited state of ^{38}Cl. A fit with an extra state fixed in energy at the spacing between the 2^- and 3^- states in ^{38}Cl is also consistent with these data.

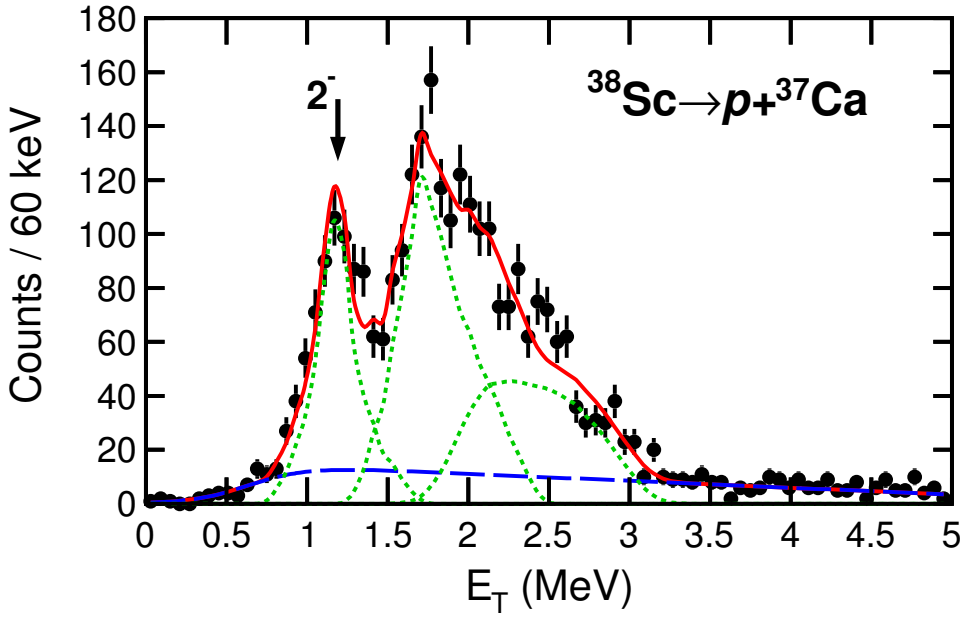

Fig. 6.8: Total decay-energy spectrum for ^{38}Sc is shown with a three-peak fit (line colors same as Fig. 6.4).

6.6 Analysis

A summary of the states measured is provided in Table 6.2. The mass measurements prompt a reexamination of the trends in neutron and proton separation energies as the former can be extended for potassium isotopes down to $N = 16$ and the latter extended for N=16 and

N=17 isotones up to scandium.

Tab. 6.2: Parameters of states identified in this work. Excitation energies and mass excesses are relative to masses from the AME2020 [2] except for ^{35}Ca [144] and ^{36}Ca[148]. States reported without uncertainties were not well constrained by their fits.

Nuclide	J^π	E_T (MeV)	E^* (MeV)	ΔM (keV)
^{34}K	1^+	0.608(17)	g.s.	-1487(17)
	2^+	1.009(18)	0.401(25)	
		∼1.85	∼1.24	
		∼2.42	∼1.81	
^{35}Ca	$3/2^+$	1.667(20)	2.08(10)	
^{36}Ca	2^+	0.464(13)	3.031(14)	
	1^+	1.632(15)	4.199(18)	
	2_2^+	∼1.94	∼4.51	
^{37}Ca	$3/2^+$	0.825(11)	3.833(11)	
		1.271(15)	4.279(15)	
		∼1.60	∼4.60	
^{37}Sc	$7/2^-$	2.69(41)	g.s.	3500(410)
^{38}Sc	2^-	1.191(14)	g.s.	-4656(14)
	(3^- or 5^-)	1.823(16)	0.632(22)	
		∼2.40	∼1.21	

The trends in neutron separation energy are shown in Fig. 6.9(a), while Fig. 6.9(b) plots the change in neutron separation energy between isotopes given by

$$\Delta S_n(N,Z) = S_n(N,Z) - S_n(N+1,Z) = \Delta M(N+1,Z) - 2\Delta M(N,Z) + \Delta M(N-1,Z). \quad (6.1)$$

The change in proton separation energy, $\Delta S_p(N,Z)$, is similarly defined to be,

$$\Delta S_p(N,Z) = S_p(N,Z) - S_p(N,Z+1) = \Delta M(N,Z+1) - 2\Delta M(N,Z) + \Delta M(N,Z-1), \quad (6.2)$$

and is plotted along with proton separation energies in Fig. 6.10(a) and (b). Figures 6.9 and 6.10 show the new data enabled by the present work as stars. The jumps in ΔS_n at $N = 20$ and $N = 28$ illustrate the classic shell closures. The increase in ΔS_n at $N = 32$ indicates an increased stability at this subshell closure.

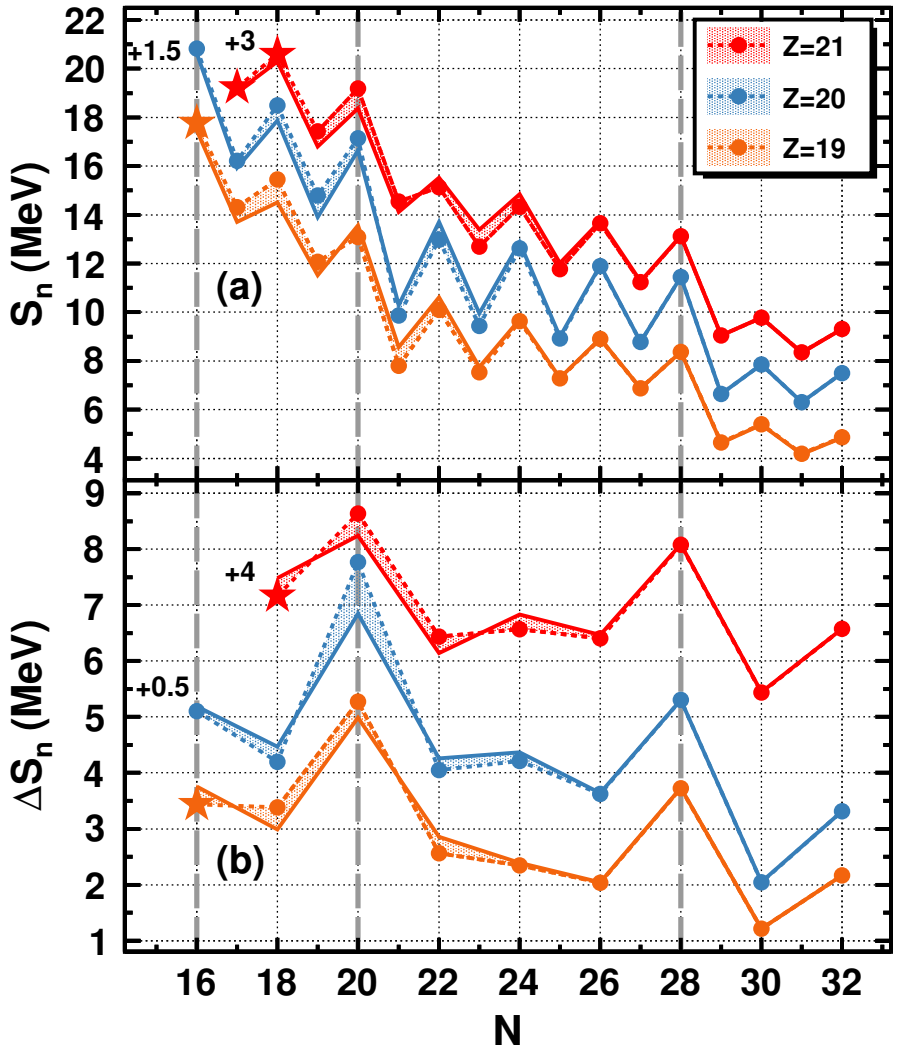

Fig. 6.9: (a) Experimental neutron separation energies for Sc, Ca, and K isotopes. (b) Changes in neutron separation energies for even N isotopes. Data are represented by points (or stars for new values) connected by dashed lines and are shifted up as indicated. Removing the Wigner energy results in the solid lines which show an increase in neutron separation energy at $N = 16$ for $Z = 19$ resembling that seen for $Z = 20$.

At $N = 16$, the raw data (points connected with dotted lines) might suggest a neutron shell closure for ^{36}Ca as was argued in Ref. [144] where the increase in ΔS_n from N=18 to N=16 was noted for Z=20 (blue data). However, for Z=19 (orange data), this increase

has largely diminished. For experimental data in this region, shell effects are conflated with the Wigner energy, where isotopes near $N = Z$ have large $T = 0$ neutron-proton pairing correlations that increase the binding energy [150]. Removing the Wigner energy from the separation energies using the form suggested by Goriely *et al.* [151], results in the solid lines in Figs. 6.9 and 6.10. The shading between the solid and dashed lines highlights the Wigner energy contribution. The Wigner-corrected separation energies show the effect of the $N = 16$ subshell closure is also present for potassium isotopes with an increase from $N = 18$ to $N = 16$ similar to that seen for calcium isotopes.

Using a similar logic, the $Z = 20$ shell gap was investigated following proton separation energies across an isotone chain. The proton separation energy differences for isotones between $N = 20$ and $N = 16$ are shown in Fig. 6.10(b). The $Z = 14$ subshell closure is most clearly seen as a peak in ΔS_p between $N = 17$ and $N = 20$. At $N = 16$, there is no evidence for this feature. With 16 neutrons, the $\nu 0d_{5/2}$ and $\nu 1s_{1/2}$ orbitals are nominally filled, so adding another neutron starts filling the $\nu 0d_{3/2}$ orbital. Through the tensor interaction [140], neutrons occupying the $\nu 0d_{3/2}$ will stabilize the $\pi 0d_{5/2}$, increasing the energy gap between it and the $\pi 1s_{1/2}$. This effect explains the observed low proton occupation of the $\pi 1s_{1/2}$ orbit in ^{34}Si, leading to the conclusion that this nucleus is doubly magic [137].

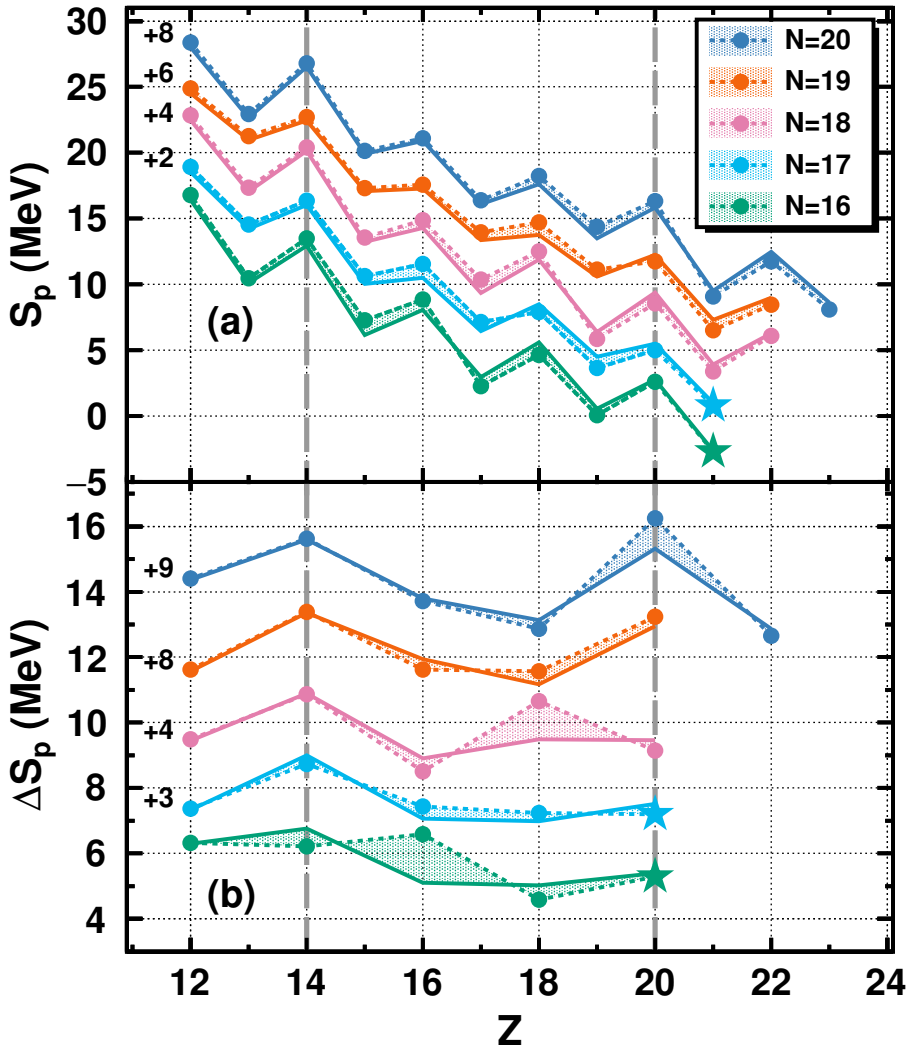

Fig. 6.10: (a) Proton separation energies for isotones from 16≤ N ≤20. (b) Changes in proton separation energies for even Z isotones. Data are represented by points (or stars for new values) connected by dashed lines and are shifted up as indicated. Removing the Wigner energy results in the solid lines which show the trends for Z=14 and Z=20.

The nucleus ^{40}Ca is doubly magic with $N = Z = 20$. Here, the $Z = 20$ shell closure appears as a sharp drop in S_p when adding a proton to get ^{41}Sc. Looking at the Wigner-corrected separation energies, the $N = 19$ isotones show a similar increase in stability but

the mass of ^{43}V has not been measured, so a point at $\Delta S_p(N = 19,\ Z = 22)$ can not be determined. For the neutron deficient calcium isotopes, the $Z = 20$ shell closure weakens markedly at $N = 18$. The Wigner-corrected energies show no jump at $N = 18$ and the data from the present work, see stars for ^{38}Sc and ^{37}Sc, verify that there is little to no increased stability at $Z = 20$ for $N = 17$ and $N = 16$.

6.7 Conclusion

Using invariant-mass spectroscopy, previously unknown proton decays near or beyond the proton drip-line were observed. The $3/2^+$ first excited state of ^{35}Ca was observed and provides an update to the excitation energy for this state. This work presents the first observations of ^{37,38}Sc and ^{34}K all of which are odd-Z ground-state single-proton emitters. The data for ^{34}K was fit to determine the ground-state mass as well as the energy of the first excited state. Higher-lying states in ^{34}K were not resolved, but there is evidence that they decay to excited states of ^{33}Ar. The data for ^{37}Sc was sparse but provides a ground-state-mass measurement with a relatively large uncertainty. In addition, the ground-state mass and energy of the first excited state of ^{38}Sc were measured.

Comparisons of the resolved states with predictions from the USDC shell-model Hamiltonian show agreement with the data for ^{35}Ca and ^{34}K but the model space lacks the pf-shell and cannot calculate the properties of ^{37,38}Sc. The ZBM2 Hamiltonian model was noticeably left out from the analysis of the nuclei presented in this chapter. This is because the ZBM2 interaction does not provide absolute binding energies needed to compare decay-energies. It can only be used to compare excited states which are limited compared to the ground state mass measurements highlighted in this work. It also does not implement isospin-breaking terms such as the Thomas-Ehrman shift, meaning predictions for energy levels would likely

need to be changed by estimates of their effect.

The ground-state masses measured in this work were used to examine trends in proton and neutron separation energies. The $N = 16$ subshell closure was investigated through neutron separation energies in the potassium isotopic chain, showing signs of increased stability in ^{35}K when the Wigner energy is removed. Removing this neutron-proton $T = 1$ (but not necessarily J = 1) congruence stabilization energy is crucial to understanding how shells evolve close to $N = Z$ [152]. The proton separation energies show a weakening of the $Z = 20$ shell closure in this neutron deficient region. This is in agreement with the analysis of the ^{36}Ca B(E2↑) strength [105] and the two-nucleon removal cross section for ^{38}Ca [117]. This has also been mentioned in a recent global examination of the trends in shell gaps over the whole chart of nuclides [152]. The three masses measured in this work help understand the evolution of shells in nuclei far from stability.

Chapter 7

Summary and Outlook

7.1 Conclusion

In this work, a collection of proton decaying resonances were observed through invariant mass spectroscopy. The properties of these states were applied to studies of nuclear structure, specifically the effects of the continuum on near-threshold resonances and the evolution of shell structure in the neutron-poor calcium region. When relevant, these studies have also been connected to topics of astrophysical importance such as (p,γ) reaction rates in the rp-process, the importance of near-threshold resonances, or the equation-of-state physics looking at the density dependence of the symmetry energy.

In Chapter 3, the experiment was a search for a predicted near-threshold s-wave resonance in ^{7}Li. The state was predicted by Vorrabi *et al.*[53] with the NCSMC, and was expected to be just above the p+^{6}He decay threshold. The data showed no evidence for a state with energy between the proton decay threshold and the IAS with large proton spectroscopic strength, excluding the possibility of a narrow resonance or a sharply rising but broad proton resonance. This experiment helps provide useful feedback to the NCSMC for other near-threshold resonances that could be important for astrophysics. Improvements in these calculations increase their accuracy in evaluating astrophysical S-factors requiring

accurate resonances properties [153].

In an experiment at the NSCL, isotopes were studied in the neutron-poor calcium region resulting from reactions on the ^{37}Ca beam. From this experiment, the p/γ branching ratio for the 2^+ state of ^{36}Ca was studied and determined to be $B_p = 0.087(8)$. This enabled the measurement of the reduced electric quadrupole strength from a separate experiment, resulting in a measured $B(E2, 0_1^+ \rightarrow 2_1^+) = 131(20)\ e^2\text{fm}^4$. This experiment also resulted in the first observations of ^{37,38}Sc, and ^{34}K. Results from this work were used to look at an evolving shell structure in the region. The $B(E2)$ and branching-ratio values could not be reproduced with a closed Z=20 shell. The ZMB2 interaction, which predicts a larger than expected proton pf-shell occupancy in the ground state was able to reproduce the $B(E2)$ and branching-ratio values. For the three newly-observed isotopes, their ground state energies enabled a look at trends in proton and neutron separation energies. These trends showed indications of a N=16 subshell gap and a fading of the Z=20 shell gap for $N \leq$18. Together, these results would support the need for a local shell-model interaction for this neutron-poor calcium region. This would help enable experiments looking beyond ^{36}Ca towards the proton drip line.

7.2 Ideas for continuation of work

The findings from this research have set the stage for several future experiments and advancements. There are open questions which remain that require deeper investigation, particularly within the FRIB experimental program, which promises improved secondary beam rates. To conclude this dissertation, the status of these open questions is discussed.

From my work on the s-wave resonance in ^{7}Li, there are other decay branches that the predicted s-wave could show up in if coupling of the mass partitions in the NCSMC shifts

the energy of the state around. If it goes sub-threshold, it is worth-while to search for a state in the n+^{6}Li decay channel. If the energy of the resonance increases, it could have a very strong n+^{6}Li(0^{+},T=1) decay branch. My experiment was insensitive to both of these decay channels as it could only detect charged particles. These decay channels would require both a neutron and gamma detector in coincidence with charged particle detection that when combined, has sufficient resolution such that it is capable of invariant-mass spectroscopy. The paper by Vorrabi *et al.*[53] also makes a prediction for an positive parity s-wave state in ^{7}Be decaying through the p+^{6}Li channel. Similarly, this state needs to be calculated with coupled mass partitions but experimentally only charged particle decay branches are open in the predicted region of excitation energy. A search for positive parity states in ^{7}Be is of interest to the field and as a comparison to *ab initio* calculations.

In the neutron-poor calcium region, there is a strong motivation for an experiment measuring the 1p-knockout reaction on a ^{36}Ca beam. Such a reaction could measure the proton-removal spectroscopic strengths based on the states populated in the resulting ^{35}K. Presently only proton knockout to ^{35}K$_{g.s.}$ has been studied [122]. The p-wave or f-wave knockout would populate the $3/2^{-}$ or $7/2^{-}$ states in ^{35}K which would be above the proton decay threshold. This would require an experimental setup similar to the one used at the NSCL in this work such that the excited proton-emitting states can be observed through invariant-mass spectroscopy.

With a ^{36}Ca beam and setup for IMS, there are many exciting prospects. It is possible a ^{36}Ca beam would excite the 0^{+}_{2} state in ^{36}Ca with higher statistics than the work presented here. This state should have a competitive proton emission decay which could be observed resulting in a more accurate determination of the energy. The lifetime of this state is also of interest as the quasi-bound proton is only a few hundred keV of energy above the decay threshold.

Moreover, this setup provides a highly interesting opportunity for the first observation of the even-even nucleus ^{34}Ca. This nuclide would be the lightest calcium isotope observed and is of interest as it potentially has a neutron bubble structure [123], is possibly a double-magic nucleus [124, 125], and is a candidate for a two-proton ground state emitter [126, 127, 128]. Similar to the work in [117], the two neutron knockout cross section to ^{34}Ca should be compared to the two-nucleon amplitudes calculated in a shell-model. An experiment looking for ^{34}Ca, will also study the properties of ^{33}K, which could be directly populated by knockout reactions or result as an intermediate of the $2p$ decay of ^{34}Ca. Because the masses of ^{33}K and ^{34}Ca are both unknown, it is uncertain whether the ground state of ^{34}Ca will decay by sequential $1p$ emission or if it will only decay through direct $2p$ emission. This uncertainty in mass and decay mode also results in an uncertain lifetime of ^{34}Ca. If the state is too long lived, it may not decay quick enough to be detected in a setup designed for IMS.

APPENDICES

Appendix A

Principles of Cyclotrons and Secondary Beams

Both experiments presented in this dissertation used the secondary beam capabilities at either the National Superconducting Cyclotron Laboratory (NSCL) or the Texas A&M Cyclotron Institute. Presented here is a brief overview on how these facilities produce secondary beams of radioactive isotopes through the use of cyclotrons and magnetic separators.

A.1 Cyclotrons

The cyclotron was first conceptualized around 1929 by Ernest Lawrence. Then with the help of his graduate student, Stanley Livingston, the first cyclotron was constructed and operating by 1932 [154]. This work, along with his research regarding artificial radioactive elements made possible by the cyclotron, won Lawrence the 1939 Nobel prize in physics [155]. Since then, cyclotrons have been a workhorse for basic nuclear science research (such as all of the work presented in this dissertation) but have also found major use cases in fields such as medicine, where they are used for radioisotope production and proton therapy, or the aerospace industry which test electronics susceptibility to radiation damage.

The principle of operation for a cyclotron is simple but effective, taking advantage of the Lorentz force law,

$$\boldsymbol{F} = q\boldsymbol{E} + q\boldsymbol{v} \times \boldsymbol{B}, \tag{A.1}$$

describing the force acting on a charge particle, q, in an electric field $\boldsymbol{E}$ and magnetic field $\boldsymbol{B}$, moving with velocity $\boldsymbol{v}$. The process starts with an ion source which injects positively charged particles at the center of the cyclotron at point (a) in Fig. A.1 where we can follow the path of a single ion. The oscillating frequency between the "D"-shaped sections called dees, produces an electric field across their gap which applies a force on the ion, accelerating it into the dee. Now that the ion has a velocity, the uniform magnetic field (pointing out of the page for Fig. A.1) applies a force that accelerates the ion in a circular path with constant radius. The radius the charged particle with mass m takes is defined as the gryoradius, r_g, which is given by,

$$r_g = \frac{mv}{qB}, \tag{A.2}$$

bending the charged particle back around to the dee gap at point (b). Once back at the gap, the alternating electric field has switched such that the field is reversed, accelerating the particle towards the other dee section of the cyclotron. The cycle is repeated, moving the ion in a circular path until point (c) where it accelerates again and takes a larger radius. The electric field between the dees must oscillate at a set frequency which matches the charged particle's orbital frequency given by,

$$f = \frac{qB}{2\pi m}, \tag{A.3}$$

also known as the cyclotron frequency.

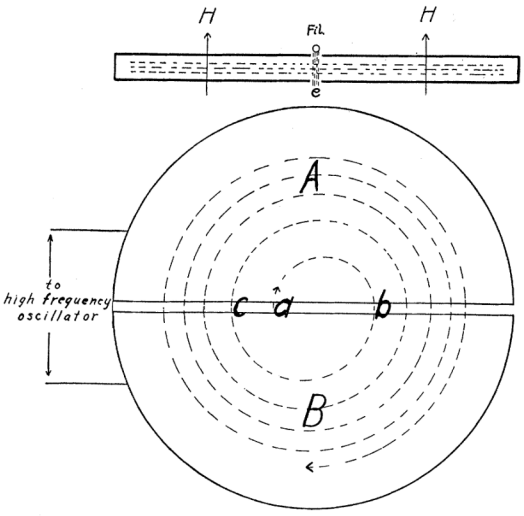

Fig. A.1: Diagram of a cyclotron taken from the first scientific report from Lawrence and Livingston [154]. The dotted line follows the trajectory for a positively charged ion between two dee sections within a magnetic field pointing out of the page.

A charged particle in a modern cyclotron will take hundreds of trips around, accelerating each time the gap is passed. The gryoradius increasing as the velocity increases. Eventually, the particle reaches a maximum energy,

$$E = \frac{1}{2}mv^2 = \frac{q^2B^2r^2}{2m}, \tag{A.4}$$

achieved at the maximum radius, r, of the cyclotron for a given charge to mass radio. From this, it is clear the maximum energy of a cyclotron for a given magnetic field — typically fixed at a constant value — is entirely dependent on the radius.

For ions at their maximum radius, the beam must be extracted from the cyclotron. Two main methods are employed depending on the charge of the ions accelerated. For positively charged ions, the beam is extracted with a slight pull from a electrostatic deflector which pulls the ions out of the magnetic field to be sent down the beamline for the experiment. A cyclotron can also accelerate negative ions as well except they rotate the opposite direction

through the cyclotron. This is commonly used when accelerating H^- ions for high intensity proton or deuteron beams. For a negative ion beam, it is extracted by passing the high energy ions through a stripper foil, removing the electrons and changing the polarity of the beam. This causes them to arc in the opposite direction in the magnetic field and out of the cyclotron as a beam.

At the Texas A&M Cyclotron Institute, the experiment from Chapter 3 used the K150 cyclotron. The K150 cyclotron, which has an active diameter of 88 inches, is named using the K-factor,

$$\frac{E}{A} = K\left(\frac{q}{A}\right)^2, \tag{A.5}$$

which is used to classify the cyclotron by the maximum kinetic energy per atomic mass for a given charged particle [156]. For the ^{7}Li beam from the K150, the maximum beam kinetic energy would be 27.5 MeV/A for fully stripped $^7Li^{3+}$ ions. The Texas A&M Cyclotron Institute also has a machine capable of reaching higher energies, a K500 cyclotron that runs independently of the K150 but shares experimental halls. While the K500 has a higher maximum energy, which opens up more experimental possibilities, the K150 can provide higher intensity beams because of its more efficient injection [157].

When you push cyclotrons towards higher energies, relativistic effects must be taken into account. As the energy of the particle increases, so does its mass. The lorentz factor, γ, can be applied to determine the relativistic mass of a particle from its restmass, m_0, as

$$m = \frac{m_0}{\sqrt{1-\left(\frac{v}{c}\right)^2}} = \gamma m_0. \tag{A.6}$$

This new relativistic mass can be directly applied to both the gyro radius as,

$$r_g = \frac{\gamma m v}{qB}, \tag{A.7}$$

and the cyclotron frequency as,

$$f = \frac{qB}{2\pi\gamma m_0}. \tag{A.8}$$

It is clear that as energy increases and therefore γ increases, we must take into account the relativistic effects as (1) the gryoradius gets larger requiring massive (and more expensive) cyclotron magnets and (2) the frequency decreases and is no longer constant for a specific ion. To overcome these issues, there are two separate strategies and types of cyclotrons, the synchrocyclotron and the isochronous cyclotron.

The synchrocyclotron modulates the frequency to account for relativistic effects as the particles are accelerated. The frequency of the oscillating electric field decreases to match the changing orbital frequency as particles effectively get heavier at high energies. The issue with this type of cyclotron is that the frequency modulation results in only packets of ions being captured in stable acceleration orbits. This results in a large loss of injected ions from the source that are out of phase from the changing frequency. This typically results in lower beam intensities compared to fixed-frequency cyclotrons. One advantage of the synchrocyclotron is that you can reach relativistic energies with simple magnet design compared to the next type of cyclotron, the isochronus cyclotron.

To return back to a fixed-frequency, and therefore more intense beams, you can use an isochronous cyclotron instead. An isochronous cyclotron modulates the magnetic field to overcome the relativistic effects and keep the fixed-frequency. To first approximation, you could do this by increasing the magnetic field as the radius increases but this results in an axially unstable orbit where ions above or below the mid-plane of the magnet poles are pushed

further from the mid-plane, defocusing the beam, and again losing intensity [158]. A better way to design an isochronous cyclotron is to have azimuthally varying fields with magnetic hills and valleys. The magnitude of a vertical $\boldsymbol{B}$-field is roughly inversely proportional to the distance between the magnet poles, so the hills seen in Fig. A.2(a) are areas of high magnetic field and the valleys have a much weaker magnetic field. In Fig. A.2(b), the effect of the higher magnetic field on the trajectory of the ions can be observed where the bending takes place primarily in the hills. In the hill and valley geometry, it is possible to build the accelerating structure or dees into the valleys between the hills so each ion would pass through three acceleration regions in one rotation.

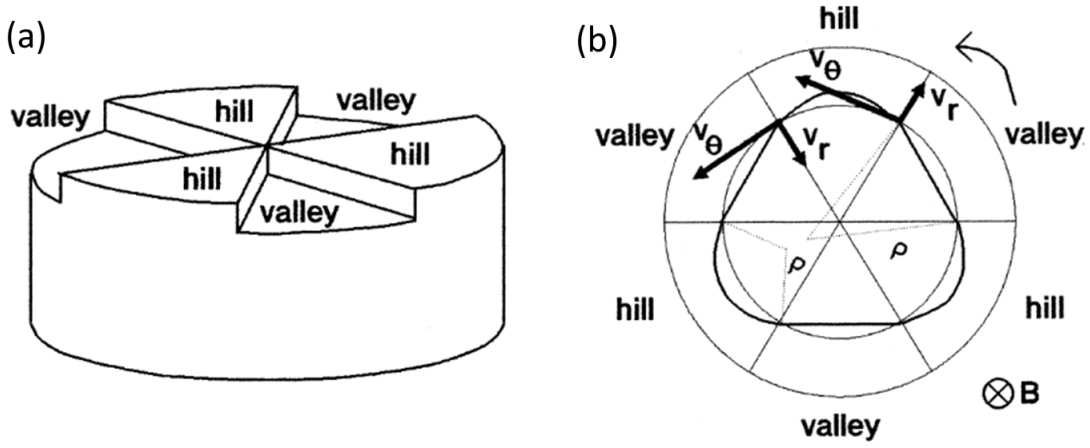

Fig. A.2: (a) Side view of one magnetic pole that has hills and valleys. The hills will be closer to the upper magnetic pole resulting in a strong magnetic field while the valleys will be further from the upper magnetic pole resulting in a weak field strength. (b) orbit of a positively charge particle in an azimuthally varying field cyclotron. [158]

As the particle reaches higher energies in the hill and valley cyclotron, and therefore larger radius orbits, the shape of the magnetic sectors can be changed to account for relativistic effects. It is no longer the strength of the magnetic field which changes, it is the magnetic field integrated over the path length ($\int Bdl$) that must increase. An example is seen in Fig. A.3

for TRIUMF's cyclotron magnetic sectors that create the hills. At small radii, the particles have short path lengths through the magnet, increasing linearly in radius similar to Fig. A.2. At large radii, the shape of the magnetic sections begin to spiral and are shaped such that the path length of a particle moving over the hill region increases, resulting in orbits that match the change in mass due to relativistic effects. This is a delicate balance that requires precise matching of the field strength in the design process and careful manufacturing to allow the frequency to remain constant.

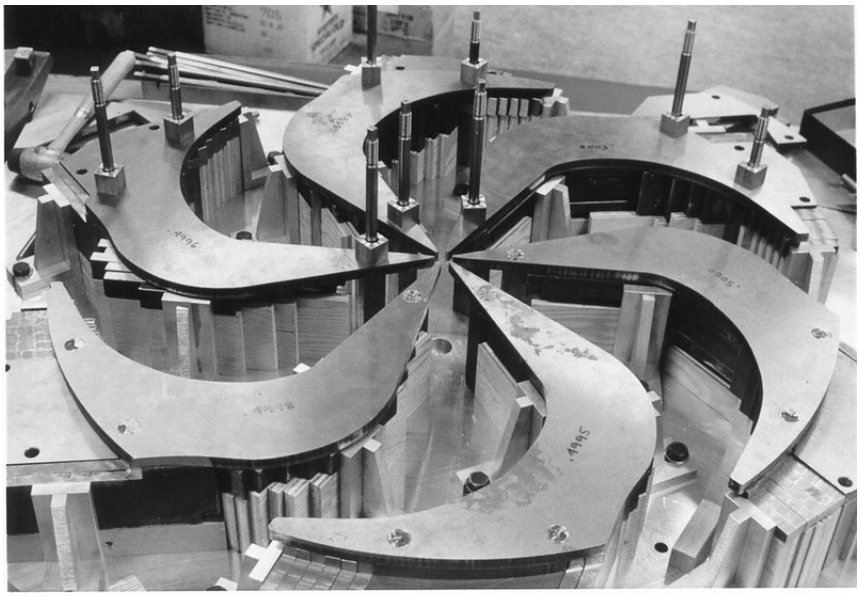

Fig. A.3: Magnets sectors for Canada's particle accelerator center TRIUMF spiral and increase in width in the outermost regions to account for relativistic effects. [159]

The National Superconducting Cyclotron Laboratory (NSCL) has two isochronous cyclotrons that are coupled together, the K500 and the K1200. They both take advantage of superconducting magnets to create stronger magnetic fields, allowing the cyclotron to take up less space because of the smaller gryoradius. The principle of the K500⊗K1200 accelerator operates as follows [160]:

1. The Electron Cyclotron Resonance (ECR) source feeds nuclei in charge state Q_1 axially into the K500.

2. The K500 does the primary acceleration to energies of tens of MeV/u.

3. The K500 beam is transported and injected horizontally into the K1200 cyclotron.

4. The ions in the beam are stripped to a higher charge state Q_2, increasing the charge to mass ratio and allowing heavier isotopes to reach higher energies.

5. The beam is accelerated to its final energy $\leq$ 200 MeV/u, extracted, and sent to the fragment separator.

Overall, this scheme allows for higher intensity and higher energy beams which are needed in the production of secondary beams.

A.2 In-flight separators

A single cyclotron, or more generally a single accelerator, is limited in that it requires an ion source to do the initial injection of charged ions. This restricts the portion of the chart of nuclides available to only stable elements or to those with long half-lives such that it is possible to feed into the ion source. In order to study unstable or exotic nuclei, it is required that they are created just before they are needed. There are currently two main methods for creating beams of radioactive nuclei, the ISOL technique and the in-flight technique.

One method of creating a radioactive beam is through the Isotope Separation On-Line or the ISOL technique [161]. Here a primary accelerator bombards a thick heavy-element target with a high-energy light-ion beam to create a large variety of different nuclei through spallation, fragmentation, or fission reactions. At the same time, the target is heated up

so the recently produced isotopes emanate out of the target and into an ion source. The fragments are magnetically separated at low energies and then fed into a second accelerator. This type of radioactive beam facility can be found for example at CERN's ISOLDE facility [162] and TRIUMF, providing high intensity low energy radioactive beams. One issue with this design is that it depends on the chemistry of the element you wish to accelerate. Refractory elements are particularly hard to create radioactive beams from as they don't migrate out of the initial target and they tend to stick to the walls of the ion source, limiting the variety of isotopes they are able to study.

The other major method of creating a radioactive beam, and the one that is primarily used in the work of this dissertation, is in-flight separation techniques. From the main accelerator, a high-energy and high-intensity primary beam bombards a target and reaction products from the beam continue through to magnetic separators to create the secondary beam. This technique can be used to create a wide range of exotic nuclei but a device that separates out and selects the isotopes of interest is required. This is the job of the fragment separator, to create a secondary beam of exotic nuclei that can be used in experiments. Many major facilities in nuclear physics pair their accelerator with a fragment separator such as the ARIS/A1900 at FRIB (formerly NSCL) [163, 164], the LISE3 at GANIL [165], the FRS at GSI [166], and bigRIPS at RIKEN [167]. These fragment separators aim to have three main features: (1) a large acceptance with high transmission of isotopes of interest, (2) a high resolving power that results in secondary beams as pure as possible, and (3) an achromatic beam that has a tuneable beam momentum. Here, achromatic, a term from optical physics, implies that after the separator, the momentum does not depend on the position, which is important for keeping a small beam profile.

The A1900 coupled to the NSCL was used in Chapters 4 through 6 of this dissertation and is diagrammed in Fig. A.4. The A1900 is composed of eight quadrupole triplet sections

and four 45° superconducting dipole magnets. The quadrupole tripet sections also include a coaxial set of hexapole and octupole coils for abberration corrections. The overall design is symmetrical which reduces high order geometrical aberrations. After the primary beam hits the production target, the A1900 separates knockout-reaction fragments based on their magnetic rigidity using a Bρ - ΔE - Bρ design. The first two dipoles start with a rough selection of charge to mass ratio based on magnetic rigidity. Then at image 2, the beam passes though a wedge shaped degrader where ions with different Z lose different amounts of momentum and no longer have the same Bρ as the desired ions. The second set of two dipoles then separates based on rigidity again resulting in improved purity of the secondary beam.

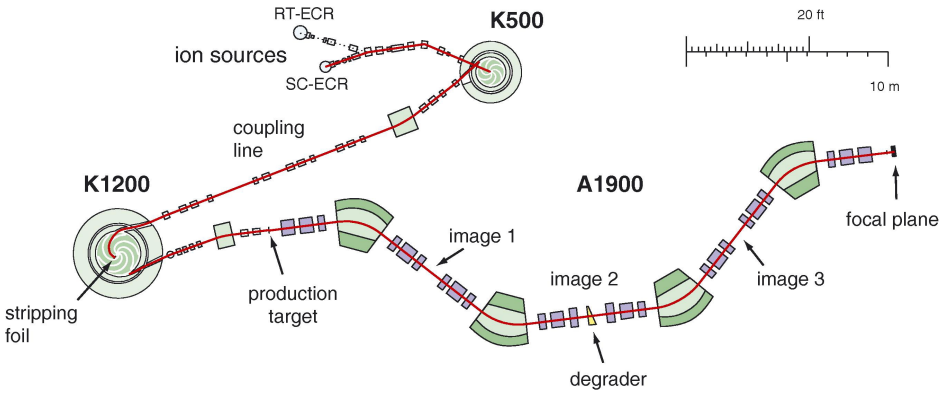

Fig. A.4: The A1900 fragment separator coupled to the NSCL. The coupled cyclotrons produce the primary beam starting from the K500 and then the K1200. The primary beam hits the production target at the start of the A1900 producing knockout reactions. The quadrupole triplets along with other smaller magnets are shown in purple while the four superconducting dipole magnets are shown in green. The first section centered around image 1 produces a Bρ section, a degrader located at image 2 changes the energy, then the second section around image 3 produces a second Bρ section. The secondary beam is selected at the focal plane of the A1900 to be used in an experiment. [168]

At Texas A&M, they have the Momentum Achromat Recoil Spectrometer (MARS) [169] that can create secondary beams. Instead of separating after a knockout reaction, they use

transfer reactions to populate nuclei just off of stability. The transfer reaction occurs in inverse kinematics when the primary beam hits the cryogenic gas target, filled with a light gas such as H_2 or D_2, and sends the recoil products around 0° into the separator. This technique can leverage the higher resonance production cross sections compared to knockout reactions and transfer reactions can be preformed at lower energies, but it requires tuning for each specific reaction and it can't add or remove more than a few nucleons.

MARS has two dispersive planes and is diagrammed in Fig. A.5. The momentum dispersive plane occurs directly after the gas target. Quadrupole magnets (Q1 and Q2) focus the beam into the dipole (D1) which bends and separates the beam based on magnetic rigidity. Momentum slits in the coffin section block nuclei which have the wrong charge to mass ratio such as other reaction products and the primary beam. Finally, Q3 refocuses the beam and D2 keeps the beam achromatic heading to the velocity dispersive plane. The velocity dispersive plane uses a vertical static electric field and a horizontal magnetic field to create a Wien filter. A Wien filter takes advantage of the Lorentz force law in Eq. (A.1), that for a given $\boldsymbol{E}$ and $\boldsymbol{B}$, only a single velocity has no net force. The last three elements after the velocity filter are the third dipole, D3, and two more focusing quadruple magnets. The third dipole and the beamline that follows is unique because it is adjustable in the vertical dispersive plane which allows for the final momentum focus and m/q selection after the Wien filter. This results in a secondary beam with major contaminates having similar charge to mass ratios as the beam of interest in the experiment.

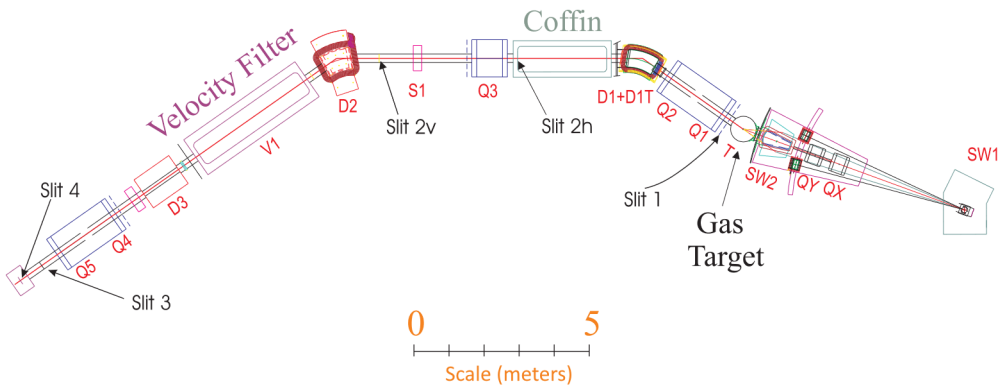

Fig. A.5: The Momentum Achromat Recoil Spectrometer at the Texas A&M Cyclotron Institute. The primary beam enters from the right to hit the gas target. Then the recoil products are separated to produce a secondary beam at the experimental station on the left. [170]

It it through cyclotrons and separators that the experimental work in this dissertation were possible. The experiment disscussed in Chapter 3 were preformed at the Texas A&M Cyclotron Institute's K150 cyclotron along with MARS. The results in Chapters 4 to 6 were a result of the second to last experiment preformed at the National Superconducting Cyclotron Laboratory. Secondary beam experiments have opened up the chart of nuclides for studies in inverse kinematics and through upgrades like FRIB, promise to extend our knowledge to thousands of new isotopes.

Bibliography

[1] National Nuclear Data Center, "information extracted from the nudat database," 2024. https://www.nndc.bnl.gov/nudat/.

[2] M. Wang, W. J. Huang, F. G. Kondev, G. Audi, and S. Naimi, "The AME 2020 atomic mass evaluation (ii). tables, graphs and references*," *Chinese Physics C*, vol. 45, p. 030003, Mar 2021.

[3] G. Gamow and E. Rutherford, "Mass defect curve and nuclear constitution," *Proc. R. Soc. Lond. Series A*, vol. 126, no. 803, pp. 632–644, 1930.

[4] C. F. v. Weizsäcker, "Zur theorie der kernmassen," *Z Phys.*, vol. 96, p. 431–458, July 1935.

[5] F. R. Daniel and W. Commons, "Liquid drop model," 2012. https://commons.wikimedia.org/wiki/File:Liquid_drop_model.svg.

[6] OpenStax and LibreTexts, "Figure 10.3.2 on nuclear binding energy." https://phys.libretexts.org/Bookshelves/University_Physics/University_Physics_%28OpenStax%29/University_Physics_III_-_Optics_and_Modern_Physics_%28OpenStax%29/10%3A__Nuclear_Physics/10.03%3A_Nuclear_Binding_Energy is licensed under CC BY 4.0.

[7] Ragnarstroberg, "Nuclear bindingenergies vs liquiddrop," 2014. https://commons.wikimedia.org/wiki/File:Nuclear_BindingEnergies_vs_liquidDrop.png.

[8] M. G. Mayer, "On Closed Shells in Nuclei. II," *Phys. Rev.*, vol. 75, pp. 1969–1970, Jun 1949.

[9] O. Haxel, J. H. D. Jensen, and H. E. Suess, "On the "magic numbers" in nuclear structure," *Phys. Rev.*, vol. 75, pp. 1766–1766, Jun 1949.

[10] B. A. Brown, A. Etchegoyen, N. S. Godwin, W. D. M. Rae, W. A. Richter, W. E. Ormand, E. K. Warburton, J. S. Winfield, L. Zhao, and C. H. Zimmerman, "Oxbash for windows pc," *MSU-NSCL report number 1289*, 2004.

[11] B. A. Brown and W. D. M. Rae, "The shell-model code nushellx@msu," *Nucl. Data Sheets*, vol. 120, pp. 115–118, 2014.

[12] N. Shimizu, "Nuclear shell-model code for massive parallel computation, "KSHELL"," 2013. arXiv:1310.5431.

[13] E. Caurier, "code ANTOINE," *Strasbourg*, 1989.

[14] B. A. Brown and W. A. Richter, "New "USD" hamiltonians for the *sd* shell," *Phys. Rev. C*, vol. 74, p. 034315, Sep 2006.

[15] A. Magilligan and B. A. Brown, "New isospin-breaking "USD" hamiltonians for the *sd* shell," *Phys. Rev. C*, vol. 101, p. 064312, Jun 2020.

[16] E. Caurier, K. Langanke, G. Martínez-Pinedo, F. Nowacki, and P. Vogel, "Shell model description of isotope shifts in calcium," *Phys. Lett. B*, vol. 522, no. 3-4, pp. 240–244, 2001.

[17] T. K. Alexander and J. S. Forster, *Lifetime Measurements of Excited Nuclear Levels by Doppler-Shift Methods*, pp. 197–331. Boston, MA: Springer US, 1978.

[18] J. M. Blatt and V. F. Weisskopf, *Theoretical Nuclear Physics*. John Wiley and Sons, 1952.

[19] D. Hill and J. A. Wheeler, "Nuclear constitution and the interpretation of fission phenomena," *Phys. Rev.*, vol. 89, pp. 1102–1145, Mar 1953.

[20] R. J. Tighe, D. M. Moltz, J. C. Batchelder, T. J. Ognibene, M. W. Rowe, and J. Cerny, "Evidence for the ground-state proton decay of ^{105}Sb," *Phys. Rev. C*, vol. 49, pp. R2871–R2874, Jun 1994.

[21] A. A. Sonzogni, "Proton radioactivity in z $>$ 50 nuclides," *Nucl. Data Sheets*, vol. 95, no. 1, pp. 1–48, 2002.

[22] T. B. Webb, R. J. Charity, J. M. Elson, D. E. M. Hoff, C. D. Pruitt, L. G. Sobotka, K. W. Brown, J. Barney, G. Cerizza, J. Estee, W. G. Lynch, J. Manfredi, P. Morfouace, C. Santamaria, S. Sweany, M. B. Tsang, T. Tsang, Y. Zhang, K. Zhu, S. A. Kuvin, D. McNeel, J. Smith, A. H. Wuosmaa, and Z. Chajecki, "Invariant-mass spectrum of ^{11}O," *Phys. Rev. C*, vol. 101, p. 044317, Apr 2020.

[23] Y. Jin, C. Y. Niu, K. W. Brown, Z. H. Li, H. Hua, A. K. Anthony, J. Barney, R. J. Charity, J. Crosby, D. Dell'Aquila, J. M. Elson, J. Estee, M. Ghazali, G. Jhang, J. G. Li, W. G. Lynch, N. Michel, L. G. Sobotka, S. Sweany, F. C. E. Teh, A. Thomas, C. Y. Tsang, M. B. Tsang, S. M. Wang, H. Y. Wu, C. X. Yuan, and K. Zhu, "First observation of the four-proton unbound nucleus ^{18}Mg," *Phys. Rev. Lett.*, vol. 127, p. 262502, Dec 2021.

[24] R. J. Charity, J. Wylie, S. M. Wang, T. B. Webb, K. W. Brown, G. Cerizza, Z. Chajecki, J. M. Elson, J. Estee, D. E. M. Hoff, S. A. Kuvin, W. G. Lynch, J. Manfredi, N. Michel, D. G. McNeel, P. Morfouace, W. Nazarewicz, C. D. Pruitt, C. Santamaria, S. Sweany, J. Smith, L. G. Sobotka, M. B. Tsang, and A. H. Wuosmaa, "Strong evidence for ^{9}N and the limits of existence of atomic nuclei," *Phys. Rev. Lett.*, vol. 131, p. 172501, Oct 2023.

[25] R. G. Thomas, "An analysis of the energy levels of the mirror nuclei, ^{13}C and ^{13}N," *Phys. Rev.*, vol. 88, pp. 1109–1125, Dec 1952.

[26] J. B. Ehrman, "On the displacement of corresponding energy levels of ^{13}C and ^{13}N," *Phys. Rev.*, vol. 81, pp. 412–416, Feb 1951.

[27] I. Tanihata, "Neutron halo nuclei," *J. Phys. G Nucl. Part. Phys.*, vol. 22, p. 157, Feb 1996.

[28] W. Schwab, H. Geissel, H. Lenske, K. H. Behr, A. Brünle, K. Burkard, H. Irnich, T. Kobayashi, G. Kraus, A. Magel, G. Münzenberg, F. Nickel, K. Riisager, C. Scheidenberger, B. M. Sherrill, T. Suzuki, and B. Voss, "Observation of a proton halo in ^{8}B," *Z Phys. A-Hadron Nucl.*, vol. 350, pp. 283–284, Dec 1995.

[29] B. Buck, A. C. Merchant, and S. M. Perez, "Ground state proton emission from heavy nuclei," *Phys. Rev. C*, vol. 45, pp. 1688–1692, Apr 1992.

[30] S. Maydanyuk and S. Belchikov, "Problem of nuclear decay by proton emission in fully quantum consideration: Calculations of penetrability and role of boundary conditions," *J. Mod. Phys.*, vol. 2, pp. 572–585, 2011.

[31] A. M. Lane and R. G. Thomas, "R-matrix theory of nuclear reactions," *Rev. Mod. Phys.*, vol. 30, no. 2, pp. 257–353, 1958.

[32] E. Vogt, "R-matrix theory," in *R-matrix school of the Joint Institute for Nuclear Astrophysics at Notre Dame*, 2004.

[33] I. J. Thompson, "Introduction to R-matrix theory," in *The 2016 R-Matrix Workshop on Methods and Applications Santa Fe, NM*, 2016.

[34] R. G. Thomas, "On the determination of reduced widths from the one-level dispersion formula," *Phys. Rev.*, vol. 81, pp. 148–149, Jan 1951.

[35] C. R. Nave, "Big bang nucleosynthesis." `http://hyperphysics.phy-astr.gsu.edu/hbase/Astro/bbnuc.html`.

[36] Borb, Mrmw, Sarang, and W. Commons, "Multiple wikipedia entries." https://en.wikipedia.org/w/index.php?title=File:Fusion_in_the_Sun.svg&lang=en and https://en.wikipedia.org/wiki/File:Triple-Alpha_Process.svg and https://en.wikipedia.org/wiki/File:CNO_Cycle.svg.

[37] M. Heil, F. Käppeler, E. Uberseder, R. Gallino, and M. Pignatari, "The s process in massive stars," *Prog. Part. Nucl. Phys.*, vol. 59, no. 1, pp. 174–182, 2007.

[38] Rursus and Wikimedia Commons, "s-process elements Ag to Sb," 2007. https://commons.wikimedia.org/wiki/File:S-process-elem-Ag-to-Sb.svg.

[39] M. R. Drout, A. L. Piro, B. J. Shappee, C. D. Kilpatrick, J. D. Simon, C. Contreras, D. A. Coulter, R. J. Foley, M. R. Siebert, N. Morrell, K. Boutsia, F. D. Mille, T. W. S. Holoien, D. Kasen, J. A. Kollmeier, B. F. Madore, A. J. Monson, A. Murguia-Berthier, Y. C. Pan, J. X. Prochaska, E. Ramirez-Ruiz, A. Rest, C. Adams, K. Alatalo, E. Bañados, J. Baughman, T. C. Beers, R. A. Bernstein, T. Bitsakis, A. Campillay, T. T. Hansen, C. R. Higgs, A. P. Ji, G. Maravelias, J. L. Marshall, C. M. Bidin, J. L. Prieto, K. C. Rasmussen, C. Rojas-Bravo, A. L. Strom, N. Ulloa, J. Vargas-González, Z. Wan, and D. D. Whitten, "Light curves of the neutron star merger GW170817/SSS17a: Implications for r-process nucleosynthesis," *Science*, vol. 358, no. 6370, pp. 1570–1574, 2017.

[40] H. Schatz, A. Aprahamian, V. Barnard, L. Bildsten, A. Cumming, M. Ouellette, T. Rauscher, F. K. Thielemann, and M. Wiescher, "End point of the *rp* process on accreting neutron stars," *Phys. Rev. Lett.*, vol. 86, pp. 3471–3474, Apr 2001.

[41] J. J. Cowan, C. Sneden, J. E. Lawler, A. Aprahamian, M. Wiescher, K. Langanke, G. Martínez-Pinedo, and F. K. Thielemann, "Origin of the heaviest elements: The rapid neutron-capture process," *Rev. Mod. Phys.*, vol. 93, p. 015002, Feb 2021.

[42] M. R. Mumpower, R. Surman, G. C. McLaughlin, and A. Aprahamian, "The impact of individual nuclear properties on r-process nucleosynthesis," *Prog. Part. Nucl. Phys.*, vol. 86, pp. 86–126, 2016.

[43] K. Mercurio, R. J. Charity, R. Shane, L. G. Sobotka, J. M. Elson, M. Famiano, A. H. Wuosmaa, A. Banu, C. Fu, L. Trache, R. E. Tribble, and A. M. Mukhamedzhanov, "Correlated two-proton decay from ^{10}C," *Phys. Rev. C*, vol. 78, p. 031602, Sep 2008.

[44] Micron Semiconductor Ltd., "S4 and BB7 design." http://www.micronsemiconductor.co.uk/.

[45] M. S. Wallace, M. A. Famiano, M. J. van Goethem, A. M. Rogers, W. G. Lynch, J. Clifford, F. Delaunay, J. Lee, S. Labostov, M. Mocko, L. Morris, A. Moroni, B. E. Nett, D. J. Oostdyk, R. Krishnasamy, M. B. Tsang, R. T. de Souza, S. Hudan, L. G.

Sobotka, R. J. Charity, J. Elson, and G. L. Engel, "The high resolution array (HiRA) for rare isotope beam experiments," *Nucl. Instrum. Methods A*, vol. 583, no. 2, pp. 302–312, 2007.

[46] G. L. Engel, M. Sadasivam, M. Nethi, J. M. Elson, L. G. Sobotka, and R. J. Charity, "A multi-channel integrated circuit for use in low- and intermediate-energy nuclear physics—HINP16C," *Nucl. Instrum. Methods A*, vol. 573, no. 3, pp. 418–426, 2007.

[47] D. Weisshaar, A. Gade, T. Glasmacher, G. F. Grinyer, D. Bazin, P. Adrich, T. Baugher, J. M. Cook, C. Diget, S. McDaniel, A. Ratkiewicz, K. P. Siwek, and K. A. Walsh, "CAESAR-A high-efficiency CsI(Na) scintillator array for in-beam γ ray spectroscopy with fast rare-isotope beams," *Nucl. Instrum. Methods A*, vol. 624, no. 3, pp. 615–623, 2010.

[48] G. Knoll, *Radiation Detection and Measurement (4th ed.)*. Hoboken, NJ: John Wiley, 2010.

[49] P. D. Olcott, J. A. Talcott, C. S. Levin, F. Habte, and A. M. K. Foudray, "Compact readout electronics for position sensitive photomultiplier tubes," in *2003 IEEE Nuclear Science Symposium. Conference Record (IEEE Cat. No.03CH37515)*, vol. 3, pp. 1962–1966 Vol.3, 2003.

[50] D. Bazin, J. A. Caggiano, B. M. Sherrill, J. Yurkon, and A. Zeller, "The S800 spectrograph," *Nucl. Instrum. Methods B*, vol. 204, pp. 629 – 633, 2003.

[51] S800 Documentation, "S800 layout & S800 FP detectors." `https://wikihost.nscl.msu.edu/S800Doc/doku.php?id=start` is licensed under CC BY 4.0.

[52] J. Yurkon, D. Bazin, W. Benenson, D. J. Morrissey, B. M. Sherrill, D. Swan, and R. Swanson, "Focal plane detector for the S800 high-resolution spectrometer," *Nucl. Instrum. Methods A*, vol. 422, no. 1–3, pp. 291 – 295, 1999.

[53] M. Vorabbi, P. Navrátil, S. Quaglioni, and G. Hupin, "^{7}Be and ^{7}Li nuclei within the no-core shell model with continuum," *Phys. Rev. C*, vol. 100, p. 024304, Aug 2019.

[54] F. Hoyle, "On nuclear reactions occuring in very hot stars.I. the synthesis of elements from carbon to nickel," *Astrophys. J. Suppl. Ser.*, vol. 1, p. 12, 1954.

[55] M. Freer and H. O. U. Fynbo, "The hoyle state in ^{12}C," *Prog. Part. Nucl. Phys.*, vol. 78, pp. 1–23, 2014.

[56] E. Epelbaum, H. Krebs, D. Lee, and U. G. Meißner, "Ab initio calculation of the hoyle state," *Phys. Rev. Lett.*, vol. 106, p. 192501, May 2011.

[57] K. S. Becker, K. D. Launey, A. Ekström, and T. Dytrych, "Ab initio symmetry-adapted emulator for studying emergent collectivity and clustering in nuclei," *Front. Phys.*, vol. 11, pp. 155–362, Mar. 2023.

[58] S. Cristallo, M. L. Cognata, C. Massimi, A. Best, S. Palmerini, O. Straniero, O. Trippella, M. Busso, G. F. Ciani, F. Mingrone, L. Piersanti, and D. Vescovi, "The Importance of the $^{13}C(\alpha, n)^{16}O$ Reaction in Asymptotic Giant Branch Stars," *Astrophys. J.*, vol. 859, p. 105, may 2018.

[59] G. F. Ciani, L. Csedreki, J. Balibrea-Correa, and A. Best, "Direct measurement of the $^{13}C(\alpha, n)^{16}O$ reaction at luna," in *Recent Progress in Few-Body Physics*, pp. 277–282, Springer International Publishing, 2020.

[60] E. Epelbaum, H. Krebs, T. A. Lähde, D. Lee, and U. G. Meißner, "Viability of carbon-based life as a function of the light quark mass," *Phys. Rev. Lett.*, vol. 110, p. 112502, Mar 2013.

[61] S. Baroni, P. Navrátil, and S. Quaglioni, "Unified ab initio approach to bound and unbound states: No-core shell model with continuum and its application to ^{7}He," *Phys. Rev. C*, vol. 87, p. 034326, Mar 2013.

[62] B. R. Barrett, P. Navrátil, and J. P. Vary, "Ab initio no core shell model," *Prog. Part. Nucl. Phys.*, vol. 69, pp. 131–181, 2013.

[63] A. Ekström, C. Forssén, G. Hagen, G. R. Jansen, W. Jiang, and T. Papenbrock, "What is ab initio in nuclear theory?," *Front. Phys.*, vol. 11, Feb 2023.

[64] S. C. Pieper and R. B. Wiringa, "Quantum monte carlo calculations of light nuclei," *Annu. Rev. Nucl. Part. Sci.*, vol. 51, pp. 53–90, Dec 2001.

[65] G. Hagen, T. Papenbrock, M. Hjorth-Jensen, and D. J. Dean, "Coupled-cluster computations of atomic nuclei," *Rep. Prog. Phys.*, vol. 77, p. 096302, Sep 2014.

[66] W. H. Dickhoff and C. Barbieri, "Self-consistent Green's function method for nuclei and nuclear matter," *Prog. Part. Nucl. Phys.*, vol. 52, pp. 377–496, Apr 2004.

[67] A. Cipollone, C. Barbieri, and P. Navrátil, "Isotopic Chains Around Oxygen from Evolved Chiral Two- and Three-Nucleon Interactions," *Phys. Rev. Lett.*, vol. 111, p. 062501, Aug 2013.

[68] H. Hergert, S. Binder, A. Calci, J. Langhammer, and R. Roth, "Ab Initio Calculations of Even Oxygen Isotopes with Chiral Two-Plus-Three-Nucleon Interactions," *Phys. Rev. Lett.*, vol. 110, p. 242501, Jun 2013.

[69] R. Machleidt and D. R. Entem, "Chiral effective field theory and nuclear forces," *Physics Reports*, vol. 503, no. 1, pp. 1–75, 2011.

[70] S. Weinberg, "Phenomenological lagrangians," *Physica A Stat.*, vol. 96, no. 1, pp. 327–340, 1979.

[71] S. Weinberg, "Nuclear forces from chiral lagrangians," *Phys. Lett. B*, vol. 251, no. 2, pp. 288–292, 1990.

[72] S. Weinberg, "Effective chiral lagrangians for nucleon-pion interactions and nuclear forces," *Nucl. Phys. B*, vol. 363, no. 1, pp. 3–18, 1991.

[73] R. Roth, J. Langhammer, A. Calci, S. Binder, and P. Navrátil, "Similarity-transformed chiral $NN + 3N$ interactions for the ab initio description of ^{12}C and ^{16}O," *Phys. Rev. Lett.*, vol. 107, p. 072501, Aug 2011.

[74] C. Forssén, R. Roth, and P. Navrátil, "Systematics of 2^+ states in C isotopes from the no-core shell model," *Journal of Physics G: Nuclear and Particle Physics*, vol. 40, p. 055105, Mar 2013.

[75] P. Maris, J. P. Vary, P. Navrátil, W. E. Ormand, H. Nam, and D. J. Dean, "Origin of the anomalous long lifetime of ^{14}C," *Phys. Rev. Lett.*, vol. 106, May 2011.

[76] D. R. Entem and R. Machleidt, "Accurate charge-dependent nucleon-nucleon potential at fourth order of chiral perturbation theory," *Phys. Rev. C*, vol. 68, p. 041001, Oct 2003.

[77] R. J. Charity, K. W. Brown, J. M. Elson, W. Reviol, L. G. Sobotka, W. W. Buhro, Z. Chajecki, W. G. Lynch, J. Manfredi, R. Shane, R. H. Showalter, M. B. Tsang, D. Weisshaar, J. Winkelbauer, S. Bedoor, D. G. McNeel, and A. H. Wuosmaa, "Invariant-mass spectroscopy of ^{18}Ne,^{16} O, and ^{10}C excited states formed in neutron-transfer reactions," *Phys. Rev. C*, vol. 99, p. 044304, Apr 2019.

[78] D. R. Tilley, C. M. Cheves, J. L. Godwin, G. M. Hale, H. M. Hofmann, J. H. Kelley, C. G. Sheu, and H. R. Weller, "Energy levels of light nuclei A=5,6,7," *Nucl. Phys. A*, vol. 708, no. 1, pp. 3–163, 2002.

[79] D. R. Tilley, J. H. Kelley, J. L. Godwin, D. J. Millener, J. E. Purcell, C. G. Sheu, and H. R. Weller, "Energy levels of light nuclei A=8,9,10," *Nucl. Phys. A*, vol. 745, no. 3, pp. 155–362, 2004.

[80] R. J. Charity, S. A. Komarov, L. G. Sobotka, J. Clifford, D. Bazin, A. Gade, J. Lee, S. M. Lukyanov, W. G. Lynch, M. Mocko, S. P. Lobastov, A. M. Rogers, A. Sanetullaev, M. B. Tsang, M. S. Wallace, R. G. T. Zegers, S. Hudan, C. Metelko, M. A. Famiano,

A. H. Wuosmaa, and M. J. van Goethem, "Investigation of particle-unbound excited states in light nuclei with resonance-decay spectroscopy using a ^{12}Be beam," *Phys. Rev. C*, vol. 78, p. 054307, Nov 2008.

[81] J. F. Ziegler, M. D. Ziegler, and J. P. Biersack, "SRIM – the stopping and range of ions in matter," *Nucl. Instrum. Methods A*, vol. 268, no. 11, pp. 1818–1823, 2010.

[82] K. Brown, *Continuum Nuclear Structure of Light Nuclei.* Phd thesis, Washington University in St. Louis, Aug. 2016.

[83] I. J. Thompson, "Coupled reaction channels calculations in nuclear physics," *Computer Phys. Rep.*, vol. 7, no. 4, pp. 167–212, 1988.

[84] A. T. Rudchik, A. Budzanowski, E. I. Koshchy, L. Głowacka, Y. G. Mashkarov, M. Makowska-Rzeszutko, V. M. Pirnak, R. Siudak, A. Szczurek, J. Turkiewicz, V. V. Uleshchenko, and V. A. Ziman, "One- and two-step processes in the ^{6}Li(d,^{6} Li), (d,^{7} Li), and (d,^{7} Be) reactions at E$_d$ = 50 MeV," *Nucl. Phys. A*, vol. 602, no. 2, pp. 211–224, 1996.

[85] L. R. B. Elton and A. Swift, "Single-particle potentials and wave functions in the 1p and 2s-1d shells," *Nucl. Phys. A*, vol. 94, no. 1, pp. 52–72, 1967.

[86] S. Cohen and D. Kurath, "Effective interactions for the 1p shell," *Nuclear Physics*, vol. 73, no. 1, pp. 1–24, 1965.

[87] T. Teichmann and E. P. Wigner, "Sum rules in the dispersion theory of nuclear reactions," *Phys. Rev.*, vol. 87, pp. 123–135, Jul 1952.

[88] J. Okołowicz, M. Płoszajczak, R. J. Charity, and L. G. Sobotka, "Collectivization of anti-analog strength above charged particle thresholds," *Phys. Rev. C*, vol. 97, p. 044303, Apr 2018.

[89] P. Doornenbal, P. Reiter, H. Grawe, T. Otsuka, A. Al-Khatib, A. Banu, T. Beck, F. Becker, P. Bednarczyk, G. Benzoni, A. Bracco, A. Bürger, L. Caceres, F. Camera, S. Chmel, F. C. L. Crespi, H. Geissel, J. Gerl, M. Górska, J. Grebosz, H. Hübel, M. Kavatsyuk, O. Kavatsyuk, M. Kmiecik, I. Kojouharov, N. Kurz, R. Lozeva, A. Maj, S. Mandal, W. Meczynski, B. Million, Z. Podolyák, A. Richard, N. Saito, T. Saito, H. Schaffner, M. Seidlitz, T. Striepling, Y. Utsuno, J. Walker, N. Warr, H. Weick, O. Wieland, M. Winkler, and H. J. Wollersheim, "The T = 2 mirrors ^{36}Ca and ^{36}S: A test for isospin symmetry of shell gaps at the driplines," *Phys. Lett. B*, vol. 647, no. 4, pp. 237–242, 2007.

[90] N. Nica, J. Cameron, and B. Singh, "Nuclear data sheets for A = 36," *Nucl. Data Sheets*, vol. 113, no. 1, pp. 1–155, 2012.

[91] A. Bürger, F. Azaiez, A. Algora, A. Al-Khatib, B. Bastin, G. Benzoni, R. Borcea, C. Bourgeois, P. Bringel, E. Clément, J.-C. Dalouzy, Z. Dlouhý, Z. Dombrádi, A. Drouart, C. Engelhardt, S. Franchoo, Z. Fülöp, A. Görgen, S. Grévy, H. Hübel, F. Ibrahim, W. Korten, J. Mrázek, A. Navin, F. Rotaru, P. Roussel Chomaz, M.-G. Saint-Laurent, G. Sletten, D. Sohler, O. Sorlin, M. Stanoiu, I. Stefan, C. Theisen, C. Timis, D. Verney, and S. Williams, "Cross sections for one-neutron knock-out from ^{37}Ca at intermediate energy," *Phys. Rev. C*, vol. 86, p. 064609, Dec 2012.

[92] T. Baugher, *Neutron-rich chromium and manganese isotopes and the role of the neutron $0g_{p/2}$ and $1d_{5/2}$ orbitals in the region below ^{68}Ni.* PhD thesis, Michigan State University, 2013.

[93] V. M. Bader, *Quadrupole collectivity in neutron-deficient Sn nuclei: ^{104}Sn.* PhD thesis, Michgan State University, 2014.

[94] S. Agostinelli, J. Allison, K. Amako, J. Apostolakis, H. Araujo, P. Arce, M. Asai, D. Axen, S. Banerjee, G. Barrand, F. Behner, L. Bellagamba, J. Boudreau, L. Broglia, A. Brunengo, H. Burkhardt, S. Chauvie, J. Chuma, R. Chytracek, G. Cooperman, G. Cosmo, P. Degtyarenko, A. Dell'Acqua, G. Depaola, D. Dietrich, R. Enami, A. Feliciello, C. Ferguson, H. Fesefeldt, G. Folger, F. Foppiano, A. Forti, S. Garelli, S. Giani, R. Giannitrapani, D. Gibin, J. J. Gómez Cadenas, I. González, G. Gracia Abril, G. Greeniaus, W. Greiner, V. Grichine, A. Grossheim, S. Guatelli, P. Gumplinger, R. Hamatsu, K. Hashimoto, H. Hasui, A. Heikkinen, A. Howard, V. Ivanchenko, A. Johnson, F. W. Jones, J. Kallenbach, N. Kanaya, M. Kawabata, Y. Kawabata, M. Kawaguti, S. Kelner, P. Kent, A. Kimura, T. Kodama, R. Kokoulin, M. Kossov, H. Kurashige, E. Lamanna, T. Lampén, V. Lara, V. Lefebure, F. Lei, M. Liendl, W. Lockman, F. Longo, S. Magni, M. Maire, E. Medernach, K. Minamimoto, P. Mora de Freitas, Y. Morita, K. Murakami, M. Nagamatu, R. Nartallo, P. Nieminen, T. Nishimura, K. Ohtsubo, M. Okamura, S. O'Neale, Y. Oohata, K. Paech, J. Perl, A. Pfeiffer, M. G. Pia, F. Ranjard, A. Rybin, S. Sadilov, E. Di Salvo, G. Santin, T. Sasaki, N. Savvas, Y. Sawada, S. Scherer, S. Sei, V. Sirotenko, D. Smith, N. Starkov, H. Stoecker, J. Sulkimo, M. Takahata, S. Tanaka, E. Tcherniaev, E. Safai Tehrani, M. Tropeano, P. Truscott, H. Uno, L. Urban, P. Urban, M. Verderi, A. Walkden, W. Wander, H. Weber, J. P. Wellisch, T. Wenaus, D. C. Williams, D. Wright, T. Yamada, H. Yoshida, and D. Zschiesche, "Geant4—a simulation toolkit," *Nucl. Instrum. Methods A*, vol. 506, pp. 250–303, Jul 2003.

[95] K. W. Brown, W. W. Buhro, R. J. Charity, J. M. Elson, W. Reviol, L. G. Sobotka, Z. Chajecki, W. G. Lynch, J. Manfredi, R. Shane, R. H. Showalter, M. B. Tsang, D. Weisshaar, J. R. Winkelbauer, S. Bedoor, and A. H. Wuosmaa, "Two-proton decay from the isobaric analog state in ^{8}B," *Phys. Rev. C*, vol. 90, p. 027304, Aug 2014.

[96] L. Lalanne, O. Sorlin, A. Poves, M. Assié, F. Hammache, S. Koyama, D. Suzuki, F. Flavigny, V. Girard-Alcindor, A. Lemasson, A. Matta, T. Roger, D. Beaumel, Y. Blumenfeld, B. A. Brown, F. D. O. Santos, F. Delaunay, N. de Séréville, S. Franchoo, J. Gibelin, J. Guillot, O. Kamalou, N. Kitamura, V. Lapoux, B. Mauss, P. Morfouace, M. Niikura, J. Pancin, T. Y. Saito, C. Stodel, and J.-C. Thomas, "Structure of ^{36}Ca under the coulomb magnifying glass," *Phys. Rev. Lett.*, vol. 129, p. 122501, Sept 2022.

[97] S. Sweany, W. G. Lynch, K. Brown, A. Anthony, Z. Chajecki, D. Dell'Aquila, P. Morfouace, F. C. E. Teh, C. Y. Tsang, M. B. Tsang, R. S. Wang, and K. Zhu, "Reaction losses of charged particles in CsI(Tl) crystals," *Nucl. Instrum. Methods A*, vol. 1018, p. 165798, Sept 2021.

[98] L. Lalanne, O. Sorlin, M. Assié, F. Hammache, N. de Séréville, S. Koyama, D. Suzuki, F. Flavigny, D. Beaumel, Y. Blumenfeld, B. A. Brown, F. D. O. Santos, F. Delaunay, S. Franchoo, J. Gibelin, V. Girard-Alcindor, J. Guillot, O. Kamalou, N. Kitamura, V. Lapoux, A. Lemasson, A. Matta, B. Mauss, P. Morfouace, M. Niikura, J. Pancin, A. Poves, T. Roger, T. Saito, C. Stodel, and J.-C. Thomas, "Evaluation of the ^{35}K$(p,\gamma)^{36}$Ca reaction rate using the ^{37}Ca$(p,d)^{36}$Ca transfer reaction," *Phys. Rev. C*, vol. 103, p. 055809, May 2021.

[99] C. A. Bertulani and A. Gade, "MOMDIS: a Glauber model computer code for knockout reactions," *Comput. Phys. Commun.*, vol. 175, no. 5, pp. 372–380, 2006.

[100] N. Iwasa, "Reduced transition probabilities of the $0^+_{gs} \rightarrow 2^+_1$ transitions in ^{20}Mg, ^{28}S and ^{36}Ca," *AIP Conf. Proc.*, vol. 1533, no. May, pp. 159–162, 2013.

[101] N. Kitamura, K. Wimmer, A. Poves, N. Shimizu, J. Tostevin, V. Bader, C. Bancroft, D. Barofsky, T. Baugher, D. Bazin, J. Berryman, V. Bildstein, A. Gade, N. Imai, T. Kröll, C. Langer, J. Lloyd, E. Lunderberg, F. Nowacki, G. Perdikakis, F. Recchia, T. Redpath, S. Saenz, D. Smalley, S. Stroberg, Y. Utsuno, D. Weisshaar, and A. Westerberg, "Coexisting normal and intruder configurations in ^{32}Mg," *Phys. Lett. B*, vol. 822, p. 136682, 2021.

[102] M. Bissell, J. Papuga, H. Naïdja, K. Kreim, K. Blaum, M. De Rydt, R. Garcia Ruiz, H. Heylen, M. Kowalska, R. Neugart, G. Neyens, W. Nörtershäuser, F. Nowacki, M. Rajabali, R. Sanchez, K. Sieja, and D. Yordanov, "Proton-neutron pairing correlations in the self-conjugate nucleus ^{38}K probed via a direct measurement of the isomer shift," *Phys. Rev. Lett.*, vol. 113, p. 052502, Jul 2014.

[103] A. Koszorús, L. Vormawah, R. Beerwerth, M. Bissell, P. Campbell, B. Cheal, C. Devlin, T. Eronen, S. Fritzsche, S. Geldhof, H. Heylen, J. Holt, A. Jokinen, S. Kelly, I. Moore, T. Miyagi, S. Rinta-Antila, A. Voss, and C. Wraith, "Proton-neutron pairing correlations in the self-conjugate nucleus ^{42}Sc," *Phys. Lett. B*, vol. 819, p. 136439, 2021.

[104] A. J. Miller, K. Minamisono, A. Klose, D. Garand, C. Kujawa, J. D. Lantis, Y. Liu, B. Maaß, P. Mantica, W. Nazarewicz, W. Nörtershäuser, S. Pineda, P. Reinhard, D. Rossi, F. Sommer, C. Sumithrarachchi, A. Teigelhöfer, and J. Watkins, "Proton superfluidity and charge radii in proton-rich calcium isotopes," *Nat. Phys*, vol. 15, no. 5, pp. 432–436, 2019.

[105] N. Dronchi, D. Weisshaar, B. A. Brown, A. Gade, R. J. Charity, L. G. Sobotka, K. W. Brown, W. Reviol, D. Bazin, P. J. Farris, A. M. Hill, J. Li, B. Longfellow, D. Rhodes, S. N. Paneru, S. A. Gillespie, A. Anthony, E. Rubino, and S. Biswas, "Measurement of the $B(E2\uparrow)$ strengths of ^{36}Ca and ^{38}Ca," *Phys. Rev. C*, vol. 107, p. 034306, Mar 2023.

[106] B. A. Brown, "Mirror charge radii and the neutron equation of state," *Phys. Rev. Lett.*, vol. 119, p. 122502, Sep 2017.

[107] B. A. Brown, K. Minamisono, J. Piekarewicz, H. Hergert, D. Garand, A. Klose, K. König, J. D. Lantis, Y. Liu, B. Maaß, A. J. Miller, W. Nörtershäuser, S. V. Pineda, R. C. Powel, D. M. Rossi, F. Sommer, C. Sumithrarachchi, A. Teigelhöfer, J. Watkins, and R. Wirth, "Implications of the ^{36}Ca$-^{36}$S and ^{38}Ca$-^{38}$Ar difference in mirror charge radii on the neutron matter equation of state," *Phys. Rev. Res.*, vol. 2, p. 022035(R), May 2020.

[108] S. V. Pineda, K. König, D. M. Rossi, B. A. Brown, A. Incorvati, J. Lantis, K. Minamisono, W. Nörtershäuser, J. Piekarewicz, R. Powel, and F. Sommer, "Charge radius of neutron-deficient ^{54}Ni and symmetry energy constraints using the difference in mirror pair charge radii," *Phys. Rev. Lett.*, vol. 127, p. 182503, Oct 2021.

[109] R. H. Cyburt, A. M. Amthor, A. Heger, E. Johnson, L. Keek, Z. Meisel, H. Schatz, and K. Smith, "Dependence of X-ray burst models on nuclear reaction rates," *Astrophys. J.*, vol. 830, no. 2, p. 55, 2016.

[110] A. Gade, D. Bazin, C. M. Campbell, J. A. Church, D. C. Dinca, J. Enders, T. Glasmacher, Z. Hu, K. W. Kemper, W. F. Mueller, H. Olliver, B. C. Perry, L. A. Riley, B. T. Roeder, B. M. Sherrill, and J. R. Terry, "Detailed experimental study on intermediate-energy coulomb excitation of ^{46}Ar," *Phys. Rev. C*, vol. 68, p. 014302, Jul 2003.

[111] T. Glasmacher, "Coulomb excitation at intermediate energies," *Annu. Rev. Nucl. Part. Sci.*, vol. 48, pp. 1–31, Dec 1998.

[112] T. Motobayashi, Y. Ikeda, K. Ieki, M. Inoue, N. Iwasa, T. Kikuchi, M. Kurokawa, S. Moriya, S. Ogawa, H. Murakami, S. Shimoura, Y. Yanagisawa, T. Nakamura, Y. Watanabe, M. Ishihara, T. Teranishi, H. Okuno, and R. F. Casten, "Large deformation of the very neutron-rich nucleus ^{32}Mg from intermediate-energy coulomb excitation," *Phys. Lett. B*, vol. 346, no. 1, pp. 9–14, 1995.

[113] A. Winther and K. Alder, "Relativistic coulomb excitation," *Nucl. Phys. A*, vol. 319, no. 3, pp. 518–532, 1979.

[114] N. Nica and B. Singh, "Nuclear data sheets for A = 34," *Nucl. Data Sheets*, vol. 113, pp. 1563–1733, 2012.

[115] B. Pritychenko, M. Birch, and B. Singh, "Revisiting Grodzins systematics of B(E2) values," *Nucl. Phys. A*, vol. 962, pp. 73–102, 2017.

[116] J. J. Valiente-Dobón, A. Poves, A. Gadea, and B. Fernández-Domínguez, "Broken mirror symmetry in ^{36}S and ^{36}Ca," *Phys. Rev. C*, vol. 98, p. 011302(R), Jul 2018.

[117] T. Beck, A. Gade, B. A. Brown, J. A. Tostevin, D. Weisshaar, D. Bazin, K. W. Brown, R. J. Charity, P. J. Farris, S. A. Gillespie, A. M. Hill, J. Li, B. Longfellow, W. Reviol, and D. Rhodes, "Probing proton cross-shell excitations through the two-neutron removal from ^{38}Ca," *Phys. Rev. C*, vol. 108, p. L061301, Dec 2023.

[118] M. Honma, T. Otsuka, B. A. Brown, and T. Mizusaki, "Shell-model description of neutron-rich pf-shell nuclei with a new effective interaction GXPF 1," *Eur. Phys. J. A*, vol. 25, pp. 499–502, sep 2005.

[119] J. Chen, "Nuclear data sheets for a=39," *Nucl. Data Sheets*, vol. 149, pp. 1–251, 2018.

[120] G. Kramer, H. Blok, J. Van Den Brand, H. Bulten, R. Ent, E. Jans, J. Lanen, L. Lapikás, H. Nann, E. Quint, G. Van Der Steenhoven, P. De Witt Huberts, and G. Wagner, "Proton ground-state correlations in ^{40}ca studied with the reaction ^{40}ca(e,e'p)^{39}k," *Phys. Lett. B*, vol. 227, no. 2, pp. 199–203, 1989.

[121] M. C. Atkinson, H. P. Blok, L. Lapikás, R. J. Charity, and W. H. Dickhoff, "Validity of the distorted-wave impulse-approximation description of ^{40}Ca$(e, e'p)^{39}$K data using only ingredients from a nonlocal dispersive optical model," *Phys. Rev. C*, vol. 98, p. 044627, Oct 2018.

[122] R. Shane, R. J. Charity, L. G. Sobotka, D. Bazin, B. A. Brown, A. Gade, G. F. Grinyer, S. McDaniel, A. Ratkiewicz, D. Weisshaar, A. Bonaccorso, and J. A. Tostevin, "Proton and neutron knockout from ^{36}Ca," *Phys. Rev. C*, vol. 85, p. 064612, Jun 2012.

[123] G. Saxena, M. Kumawat, M. Kaushik, S. K. Jain, and Mamta Aggarwal, "Bubble structure in magic nuclei," *Phys. Lett. B*, vol. 788, pp. 1–6, 2019.

[124] A. Poves, "Shell model spectroscopy far from stability," *J. Phys. G*, vol. 44, p. 084002, Jun 2017.

[125] G. Saxena, M. Kumawat, M. Kaushik, U. K. Singh, S. K. Jain, S. S. Singh, and Mamta Aggarwal, "Implications of occupancy of $2s_{1/2}$ state is *sd*-shell within (RMF+BCS) approach," *Int. J. Mod. Phys. E*, vol. 26, p. 1750072, 2017.

[126] L. V. Grigorenko, I. G. Mukha, and M. V. Zhukov, "Prospective candidates for the two-proton decay studies. (ii) exploratory studies of ^{30}Ar, ^{34}Ca, and ^{45}Fe," *Nucl. Phys. A*, vol. 714, no. 3, pp. 425–440, 2003.

[127] G. Saxena, M. Kumawat, M. Kaushik, S. K. Jain, and Mamta Aggarwal, "Two-proton radioactivity with 2p halo in light mass nuclei A=18–34," *Phys. Lett. B*, vol. 775, pp. 126–129, 2017.

[128] M. Gonçalves, N. Teruya, O. A. P. Tavares, and S. B. Duarte, "Two-proton emission half-lives in the effective liquid drop model," *Phys. Lett. B*, vol. 774, pp. 14–19, 2017.

[129] Y. Kubota, A. Corsi, G. Authelet, H. Baba, C. Caesar, D. Calvet, A. Delbart, M. Dozono, J. Feng, F. Flavigny, J.-M. Gheller, J. Gibelin, A. Giganon, A. Gillibert, K. Hasegawa, T. Isobe, Y. Kanaya, S. Kawakami, D. Kim, Y. Kikuchi, Y. Kiyokawa, M. Kobayashi, N. Kobayashi, T. Kobayashi, Y. Kondo, Z. Korkulu, S. Koyama, V. Lapoux, Y. Maeda, F. M. Marqués, T. Motobayashi, T. Miyazaki, T. Nakamura, N. Nakatsuka, Y. Nishio, A. Obertelli, K. Ogata, A. Ohkura, N. A. Orr, S. Ota, H. Otsu, T. Ozaki, V. Panin, S. Paschalis, E. C. Pollacco, S. Reichert, J.-Y. Roussé, A. T. Saito, S. Sakaguchi, M. Sako, C. Santamaria, M. Sasano, H. Sato, M. Shikata, Y. Shimizu, Y. Shindo, L. Stuhl, T. Sumikama, Y. L. Sun, M. Tabata, Y. Togano, J. Tsubota, Z. H. Yang, J. Yasuda, K. Yoneda, J. Zenihiro, and T. Uesaka, "Surface localization of the dineutron in ^{11}Li," *Phys. Rev. Lett.*, vol. 125, p. 252501, Dec 2020.

[130] J. Casal and M. Gómez-Ramos, "Opening angle and dineutron correlations in knockout reactions with borromean two-neutron halo nuclei," *Phys. Rev. C*, vol. 104, p. 024618, Aug 2021.

[131] T. Oishi, K. Hagino, and H. Sagawa, "Diproton correlation in the proton-rich borromean nucleus ^{17}Ne," *Phys. Rev. C*, vol. 82, p. 024315, Aug 2010.

[132] P.-G. Reinhard and W. Nazarewicz, "Information content of the differences in the charge radii of mirror nuclei," *Phys. Rev. C*, vol. 105, p. L021301, Feb 2022.

[133] P.-G. Reinhard and W. Nazarewicz, "Toward a global description of nuclear charge radii: Exploring the fayans energy density functional," *Phys. Rev. C*, vol. 95, p. 064328, Jun 2017.

[134] C. Iliadis, *Nuclear Physics of Stars*. Weinheim, Germany: Wiley-VCH Verlag GmbH & Co. KGaA, 2nd ed., May 2015.

[135] C. Iliadis, R. Longland, A. E. Champagne, and A. Coc, "Charged-particle thermonuclear reaction rates: III. nuclear physics input," *Nucl. Phys. A*, vol. 841, no. 1, pp. 251–322, 2010.

[136] A. Ozawa, T. Kobayashi, T. Suzuki, K. Yoshida, and I. Tanihata, "New magic number, N = 16, near the neutron drip line," *Phys. Rev. Lett.*, vol. 84, pp. 5493–5495, Jun 2000.

[137] A. Mutschler, A. Lemasson, O. Sorlin, D. Bazin, C. Borcea, R. Borcea, Z. Dombrádi, J.-P. Ebran, A. Gade, H. Iwasaki, E. Khan, A. Lepailleur, F. Recchia, T. Roger, F. Rotaru, D. Sohler, M. Stanoiu, S. R. Stroberg, J. A. Tostevin, M. Vandebrouck, D. Weisshaar, and K. Wimmer, "A proton density bubble in the doubly magic ^{34}Si nucleus," *Nat. Phys.*, vol. 13, pp. 152–156, Feb 2017.

[138] C. R. Hoffman, T. Baumann, D. Bazin, J. Brown, G. Christian, D. H. Denby, P. A. DeYoung, J. E. Finck, N. Frank, J. Hinnefeld, S. Mosby, W. A. Peters, W. F. Rogers, A. Schiller, A. Spyrou, M. J. Scott, S. L. Tabor, M. Thoennessen, and P. Voss, "Evidence for a doubly magic ^{24}O," *Phys. Lett. B*, vol. 672, no. 1, pp. 17–21, 2009.

[139] Y. Kondo, N. L. Achouri, H. A. Falou, L. Atar, T. Aumann, H. Baba, K. Boretzky, C. Caesar, D. Calvet, H. Chae, N. Chiga, A. Corsi, F. Delaunay, A. Delbart, Q. Deshayes, Z. Dombrádi, C. A. Douma, A. Ekström, Z. Elekes, C. Forssén, I. Gašparić, J.-M. Gheller, J. Gibelin, A. Gillibert, G. Hagen, M. N. Harakeh, A. Hirayama, C. R. Hoffman, M. Holl, A. Horvat, Á. Horváth, J. W. Hwang, T. Isobe, W. G. Jiang, J. Kahlbow, N. Kalantar-Nayestanaki, S. Kawase, S. Kim, K. Kisamori, T. Kobayashi, D. Körper, S. Koyama, I. Kuti, V. Lapoux, S. Lindberg, F. M. Marqués, S. Masuoka, J. Mayer, K. Miki, T. Murakami, M. Najafi, T. Nakamura, K. Nakano, N. Nakatsuka, T. Nilsson, A. Obertelli, K. Ogata, F. de Oliveira Santos, N. A. Orr, H. Otsu, T. Otsuka, T. Ozaki, V. Panin, T. Papenbrock, S. Paschalis, A. Revel, D. Rossi, A. T. Saito, T. Y. Saito, M. Sasano, H. Sato, Y. Satou, H. Scheit, F. Schindler, P. Schrock, M. Shikata, N. Shimizu, Y. Shimizu, H. Simon, D. Sohler, O. Sorlin, L. Stuhl, Z. H. Sun, S. Takeuchi, M. Tanaka, M. Thoennessen, H. Törnqvist, Y. Togano, T. Tomai, J. Tscheuschner, J. Tsubota, N. Tsunoda, T. Uesaka, Y. Utsuno, I. Vernon, H. Wang, Z. Yang, M. Yasuda, K. Yoneda, and S. Yoshida, "First observation of ^{28}O," *Nature*, vol. 620, pp. 965–970, Aug 2023.

[140] T. Otsuka, R. Fujimoto, Y. Utsuno, B. A. Brown, M. Honma, and T. Mizusaki, "Magic numbers in exotic nuclei and spin-isospin properties of the NN interaction," *Phys. Rev. Lett.*, vol. 87, p. 082502, Aug 2001.

[141] T. Otsuka, A. Gade, O. Sorlin, T. Suzuki, and Y. Utsuno, "Evolution of shell structure in exotic nuclei," *Rev. Mod. Phys.*, vol. 92, p. 015002, Mar 2020.

[142] F. Wienholtz, D. Beck, K. Blaum, C. Borgmann, M. Breitenfeldt, R. B. Cakirli, S. George, F. Herfurth, J. D. Holt, M. Kowalska, S. Kreim, D. Lunney, V. Manea, J. Menéndez, D. Neidherr, M. Rosenbusch, L. Schweikhard, A. Schwenk, J. Simonis, J. Stanja, R. N. Wolf, and K. Zuber, "Masses of exotic calcium isotopes pin down nuclear forces," *Nature*, vol. 498, pp. 346–349, Jun 2013.

[143] S. Michimasa, M. Kobayashi, Y. Kiyokawa, S. Ota, D. S. Ahn, H. Baba, G. P. A. Berg, M. Dozono, N. Fukuda, T. Furuno, E. Ideguchi, N. Inabe, T. Kawabata, S. Kawase, K. Kisamori, K. Kobayashi, T. Kubo, Y. Kubota, C. S. Lee, M. Matsushita, H. Miya, A. Mizukami, H. Nagakura, D. Nishimura, H. Oikawa, H. Sakai, Y. Shimizu, A. Stolz, H. Suzuki, M. Takaki, H. Takeda, S. Takeuchi, H. Tokieda, T. Uesaka, K. Yako, Y. Yamaguchi, Y. Yanagisawa, R. Yokoyama, K. Yoshida, and S. Shimoura, "Magic nature of neutrons in ^{54}Ca: First mass measurements of $^{55-57}$Ca," *Phys. Rev. Lett.*, vol. 121, p. 022506, Jul 2018.

[144] L. Lalanne, O. Sorlin, A. Poves, M. Assié, F. Hammache, S. Koyama, D. Suzuki, F. Flavigny, V. Girard-Alcindor, A. Lemasson, A. Matta, T. Roger, D. Beaumel, Y. Blumenfeld, B. A. Brown, F. D. O. Santos, F. Delaunay, N. de Séréville, S. Franchoo, J. Gibelin, J. Guillot, O. Kamalou, N. Kitamura, V. Lapoux, B. Mauss, P. Morfouace, J. Pancin, T. Y. Saito, C. Stodel, and J.-C. Thomas, "N = 16 magicity revealed at the proton drip line through the study of ^{35}Ca," *Phys. Rev. Lett.*, vol. 131, p. 092501, Aug 2023.

[145] R. J. Charity, K. W. Brown, J. Okołowicz, M. Płoszajczak, J. M. Elson, W. Reviol, L. G. Sobotka, W. W. Buhro, Z. Chajecki, W. G. Lynch, J. Manfredi, R. Shane, R. H. Showalter, M. B. Tsang, D. Weisshaar, J. R. Winkelbauer, S. Bedoor, and A. H. Wuosmaa, "Invariant-mass spectroscopy of ^{14}O excited states," *Phys. Rev. C*, vol. 100, p. 064305, Dec 2019.

[146] R. J. Charity and L. G. Sobotka, "Invariant-mass spectroscopy in projectile fragmentation reactions," *Phys. Rev. C*, vol. 108, p. 044318, Oct 2023.

[147] A. M. Amthor, *Experimental and Theoretical Study of Nuclear Reaction Rates in the rp-Process*. PhD thesis, Michigan State University, 2008.

[148] J. Surbrook, G. Bollen, M. Brodeur, A. Hamaker, D. Pérez-Loureiro, D. Puentes, C. Nicoloff, M. Redshaw, R. Ringle, S. Schwarz, C. S. Sumithrarachchi, L. J. Sun, A. A. Valverde, A. C. C. Villari, C. Wrede, and I. T. Yandow, "First penning trap mass measurement of ^{36}Ca," *Phys. Rev. C*, vol. 103, p. 014323, Jan 2021.

[149] J. Cameron, J. Chen, B. Singh, and N. Nica, "Nuclear data sheets for A = 37," *Nucl. Data Sheets*, vol. 113, no. 2, pp. 365–514, 2012.

[150] W. Satuła, D. J. Dean, J. Gary, S. Mizutori, and W. Nazarewicz, "On the origin of the Wigner energy," *Phys. Lett. B*, vol. 407, no. 2, pp. 103–109, 1997.

[151] S. Goriely, N. Chamel, and J. M. Pearson, "Further explorations of Skyrme-Hartree-Fock-Bogoliubov mass formulas. XIII. The 2012 atomic mass evaluation and the symmetry coefficient," *Phys. Rev. C*, vol. 88, p. 024308, Aug 2013.

[152] L. Buskirk, K. Godbey, W. Nazarewicz, and W. Satuła, "Nucleonic shells and nuclear masses," *Phys. Rev. C*, vol. 109, p. 044311, Apr 2024.

[153] J. Dohet-Eraly, P. Navrátil, S. Quaglioni, W. Horiuchi, G. Hupin, and F. Raimondi, "^{3}He(α,γ)^{7}Be and ^{3}H(α,γ)^{7}Li astrophysical s factors from the no-core shell model with continuum," *Phys. Lett. B*, vol. 757, pp. 430–436, 2016.

[154] E. O. Lawrence and M. S. Livingston, "The production of high speed light ions without the use of high voltages," *Physical Review*, vol. 40, pp. 19–35, Apr 1932.

[155] Ernest Lawrence, "Nobel lecture: The evolution of the cyclotron." NobelPrize.org, 1951. Accessed: 2023-12-20.

[156] D. P. May, G. J. Kim, R. E. Tribble, H. L. Clark, F. P. Abegglen, G. J. Derrig, and G. Tabacaru, "Progress on the facility upgrade for accelerated radioactive beams at Texas A&M," in *Proc. of the 18 th Int. Conf. on Cyclotrons and their Applications. Giardini-Naxos, Italy*, pp. 505–507, 2007.

[157] D. P. May, G. J. Kim, R. E. Tribble, H. L. Clark, F. P. Abegglen, G. J. Derrig, G. Tabacaru, and G. G. Chubaryan, "Recent progress on the facility upgrade for accelerated radioactive beams at Texas A&M," in *Proc. of cyclotrons 2010, Lanzhou, China*, pp. 24–26, 2007.

[158] K. Strijckmans, "The isochronous cyclotron: principles and recent developments," *Comput. Med. Imaging Graph.*, vol. 25, no. 2, pp. 69–78, 2001.

[159] TRIUMF Lab, "500 MeV Cyclotron Magnet, '72." `https://flic.kr/p/DHFEJ8` is licensed under CC BY 2.0.

[160] NSCL Executive Committee, "The K500 $\otimes$ K1200," Tech. Rep. MSUCL-939, National Super conducting Cyclotron Laboratory Michigan State University, Jul. 1994.

[161] M. Lindroos, "Review of the ISOL-type radioactive beam facilities," in *Proceedings of the EPAC 2004, Lucerne, Switzerland*, pp. 45–49, 2004.

[162] A. Kjelberg and G. Rudstam, "The ISOLDE isotope separator on-line facility at CERN," Tech. Rep. CERN-70-03, CERN. Geneva. ISOLDE Experiments Committee, Jan. 1970.

[163] M. Hausmann, A. Aaron, A. Amthor, M. Avilov, L. Bandura, R. Bennett, G. Bollen, T. Borden, T. Burgess, S. Chouhan, V. Graves, W. Mittig, D. Morrissey, F. Pellemoine, M. Portillo, R. Ronningen, M. Schein, B. Sherrill, and A. Zeller, "Design of the advanced rare isotope separator aris at frib," *Nucl. Instrum. Methods Phys. Res. B*, vol. 317, pp. 349–353, 2013. XVIth International Conference on ElectroMagnetic Isotope Separators and Techniques Related to their Applications, December 2–7, 2012 at Matsue, Japan.

[164] D. Morrissey, B. Sherrill, M. Steiner, A. Stolz, and I. Wiedenhoever, "Commissioning the A1900 projectile fragment separator," *Nucl. Instrum. Methods B*, vol. 204, pp. 90 – 96, 2003.

[165] R. Anne and A. C. Mueller, "LISE 3: a magnetic spectrometer-Wien filter combination for secondary radioactive beam production," *Nucl. Instrum. Methods B*, vol. 70, no. 1, pp. 276–285, 1992.

[166] H. Geissel, P. Armbruster, K. Behr, A. Brünle, K. Burkard, M. Chen, H. Folger, B. Franczak, H. Keller, O. Klepper, B. Langenbeck, F. Nickel, E. Pfeng, M. Pfützner, E. Roeckl, K. Rykaczewski, I. Schall, D. Schardt, C. Scheidenberger, K.-H. Schmidt, A. Schröter, T. Schwab, K. Sümmerer, M. Weber, G. Münzenberg, T. Brohm, H.-G. Clerc, M. Fauerbach, J.-J. Gaimard, A. Grewe, E. Hanelt, B. Knödler, M. Steiner, B. Voss, J. Weckenmann, C. Ziegler, A. Magel, H. Wollnik, J. Dufour, Y. Fujita, D. Vieira, and B. Sherrill, "The GSI projectile fragment separator (FRS): a versatile magnetic system for relativistic heavy ions," *Nucl. Instrum. Methods B*, vol. 70, no. 1, pp. 286–297, 1992.

[167] T. Kubo, K. Kusaka, K. Yoshida, A. Yoshida, T. Ohnishi, M. Ohtake, Y. Yanagisawa, N. Fukuda, T. Haseyama, Y. Yano, N. Kakutani, T. Tsuchihashi, and K. Sato, "Status and overview of superconducting radioactive isotope beam separator BigRIPS at RIKEN," *IEEE Trans. Appl. Supercond.*, vol. 17, no. 2, pp. 1069–1077, 2007.

[168] A. Stolz, T. Baumann, T. Ginter, D. Morrissey, M. Portillo, B. Sherrill, M. Steiner, and J. Stetson, "Production of rare isotope beams with the nscl fragment separator," *nucl. instrum. methods B*, vol. 241, no. 1, pp. 858–861, 2005.

[169] R. Tribble, R. Burch, and C. Gagliardi, "MARS: A momentum achromat recoil spectrometer," *Nucl. Instrum. Methods A*, vol. 285, no. 3, pp. 441–446, 1989.

[170] Cyclotron Institute, "MARS." `https://cyclotron.tamu.edu/facilities/mars/`.

Glossary

ab initio Latin for "from the beginning". A name given to a certain class of quantum calculations which calculate properties of systems from first-principles.

A1900 Fragment Separator at the National Superconducting Cyclotron Laboratory used to produce secondary beams after fragmentation.

BB7 Micron Semiconductors square 64mmx64mm double sided silicon strip detector with 32 strips on each side [44].

CAESAR CAESium-iodide scintillator ARray [47].

CI Configuration Interaction.

CNO cycle Carbon-Nitrogen-Oxygen cycle in nucleosynthesis.

CRDC Cathode Readout Drift Chambers.

CsI(Na) Cesium-Iodide crystals doped with sodium.

CsI(Tl) Cesium-Iodide crystals doped with thallium.

DSSD Double-Sided Strip Detector.

FRESCO General purpose reaction code for calculating coupled channels for light and heavy ions.

Gobbi The nickname for the detector setup with four ΔE-E telescopes with an offset arrangement around a square beam hole.

HINP16C Heavy Ion Nulear Physics 16-Channel. These are the chips developed at WashU and which were used for the silicon detectors in this dissertation [46].

HIRA HIgh Resolution Array using BB7's and CsI(Tl) [45].

HO Harmonic Oscillator. A simple system with a parabolic potential and analytic wave-function solutions to Schrödinger's equation.

IAS Isobaric Analog State. An excited state with higher isospin, T, and structure matching that of a neighboring nucleus with higher isospin projection ($T_Z = \frac{N-Z}{2}$) with the same total A.

IMS Invariant-Mass Spectroscopy.

LDM Liquid Drop Model.

magnetic rigidity rigidity, $B\rho$, is the measure of a particles resistance to deflection by a magnetic field given by $B\rho = |p|/q$. Here B is the magnetic field strength, ρ is the gyroradius, p is the momentum and q is the charge. $B\rho$ is given in units of tesla-meters [Tm].

NCSMC No Core Shell Model with Continuum [62]. An *ab inito* calculation used to calculate properties for light nuclei.

NSCL National Superconducting Cyclotron Laboratory. An accelerator facility at Michigan State University which has been superseded by the Facility for Rare Isotope Beams.

PMT PhotoMultiplier Tube.

pp-chain proton-proton chain in nucleosynthesis.

QDC charge (Q) to Digital Converter.

S4 Micron Semiconductors annular form factor for silicon with 128 rings and 128 pie shaped sectors [44].

S800 Spectrograph at the National Superconducting Cyclotron Laboratory.

SEMF Semi-Empirical Mass Formula.

SFA Scintillating-Fiber Array.

telescope A stack of detectors (typically a ΔE and E) one directly behind the other.

ToF Time of Flight.